UNIVERSITÀ DI SIENA 1240

Dipartimento di Medicina molecolare e dello sviluppo

Dottorato in Medicina Molecolare

36° Ciclo

Coordinatore: Prof. Vincenzo Sorrentino

Mechanokinetic properties of an ensemble of myosin II molecular motors purified from skeletal muscle and reassembled in a sarcomere-like nanomachine

Settore scientifico disciplinare: BIO/09

Candidata

Valentina Buonfiglio

Sede di attività: Firenze

VALENTINA BUONFIGLIO
17/05/2024 13:39:13
Firma digitale del/della candidato/a

Valentina Buonfiglio

Supervisori

Prof. Pasquale Bianco

PhysioLab, University of Florence

Prof. Duccio Fanelli

Department of Physics and Astronomy, University of Florence

Co-supervisore

Prof. Marco Linari

PhysioLab, University of Florence

Anno accademico di conseguimento del titolo di Dottore di ricerca

2022/23

Università degli Studi di Siena
Dottorato in Medicina Molecolare
36° Ciclo

Data dell'esame finale
30/05/2024

Commissione giudicatrice
Prof.ssa Rossi Daniela
Dr.ssa Vitiello Marianna
Dr.ssa Sticchi Elena

Supplenti
Dr. Amato Rosario

Contents

Introduction

My research activity during the PhD course focussed on the investigation the molecular mechanism of muscle contraction in striated muscle, with the aim of providing a theoretical framework that could contribute to the definition of the mechanokinetic parameters underlying the performance of the half-sarcomere, the functional unit of the striated muscle, making use of the innovation provided by a simplified and controlled experimental setup that employs a myosin–based synthetic machine. In each sarcomere, the $\sim 2\,\mu m$ structural unit of the striated muscle cell, force and shortening are generated by the cyclical ATP-driven interactions of two bipolar arrays of motor protein myosin II, extending from the thick filament, with the nearby actin-containing thin filaments. Different isoforms of the myosin motor in the skeletal muscles account for the different functional requirements of the slow muscles (primarily responsible for the posture) and fast muscles (responsible for breathing and voluntary movements). Despite the bulk of data characterising the mechanokinetics of muscles at the cellular level, the definition of the corresponding parameters at a molecular level is still incomplete. Inferring their definition from experiments on cells and tissues is complicated because of the structural organisation of the molecular motors in the three-dimensional lattice of the sarcomere. Moreover, cellular level studies cannot resolve the details of the motor-coupling mechanism, which is also difficult to isolate from the contribution of the other cytoskeleton and regulatory proteins. On the other hand, the collective dynamics of molecular motors working in ensemble is not revealed by single molecule experiments on purified proteins. To clarify the molecular basis of the differences in the performance of slow and fast skeletal muscle, we investigated the isoform-dependent mechanokinetic parameters with a bottom-up approach, employing a Dual Laser Optical Tweezers, either in position or in force clamp, to record the output of a unidimensional synthetic machine containing the minimum number of pure myosin isoform molecules needed to reproduce the collective action of muscle myosin II in the muscle cell. In physiological ATP concentration, the nanomachine reproduces the steady force and constant velocity shortening, characteristic of the isometric and isotonic contractions of the sarcomere *in vivo*. The implementation of a custom length clamp control allows us to minimize the high compliance typical of the optical trap experimental setup: by increasing the trap stiffness up to values similar to what myosin motors are subjected to *in situ*, the rate of force development to the steady state value, as well as the force fluctuations around the isometric value (plateau), are the direct expression of the attachment-force generation and detachment of the myosin motors. A three-state stochastic model has been developed to reproduce and characterise the dynamics of the small ensemble of myosin motors performing isometric contractions in physiological ATP concentration. Accounting for the role of the force fluctuations stemming from the discrete nature of the investigated system, allowed us to characterise the development

and the probability distribution of the force exerted by a single myosin isoform. Through a process of reverse engineering, it was possible to recover isoform-dependent single motor properties from the analysis of the dynamics of the force of the whole ensemble. In fact, data fitting of the time series of the experimental force of the ensemble provided a self-consistent estimate of all the mechanokinetic properties of the motor ensemble, including the motor force, the fraction of actin-attached motors, and the rate of transition through the attachment-detachment cycle. Inferring the properties of a single molecular motor from the analysis of the dynamics of the ensemble could pave the way to study the emergent mechanokinetic properties of an ensemble of myosin molecules purified from animal models or human biopsies, and of unknown isoforms, mutant and engineered myosin motors.

Chapter 1

Introduction to muscle contraction

1.1 Elements of muscle contraction

In the following sections we introduce and review the current knowledge concerning the structure of striated (skeletal and cardiac) muscle and the molecular mechanism of muscle contraction.

1.1.1 The structure of the skeletal muscle

Skeletal muscle is composed of cylindrical multinucleated cells, the myocytes, of diameter ranging in $30 - 200\,\mu m$, running along the entire length of the muscle. The composition of each cell is extremely complex with various level of hierarchical structural organisation, Figure 1.1. In a single fibre the contractile components are organised in hundreds of myofibrils, cylindrical structures with a diameter of $\sim 1\,\mu m$, arranged in bundles enclosed by a membrane called the sarcolemma, and running in parallel along the length of the fibre. In the fibre the myofibrils are immersed in a cytoplasmic fluid, the sarcoplasm, along with the mitochondria and the sarcoplasmic reticulum involved in the regulation of the internal calcium concentration that controls the contraction-relaxation cycle. In the myofibril the contractile proteins, actin and myosin, are arranged in filaments and, along with other accessory and regulatory proteins, constitute the $\sim 2\,\mu m$ long sarcomere, the structural unit of the striated muscle. Thousands of sarcomere are connected in series throughout the muscle fibre.
The striated appearance of muscle under the light of the microscope is due to the alternating pattern of light and dark bands. Electron microscopy revealed that such appearance results from the regular alternation of the myosin-containing thick filaments (with a diameter of 12 nm), and the actin-containing thin filaments (with a diameter of 8 nm). Each sarcomere presents a highly organised structure, detailed in the following (see Figure 1.2). Two consecutive Z lines define the edges of the sarcomere. The thick filament, originating from the M line at the centre of the sarcomere, and the thin filaments, extending from the Z line at the end of the sarcomere, are partially overlapped. The dark appearance of the A bands results from the presence of both the thick and the thin filaments, while the central portion of the A band, called the H band, contains only

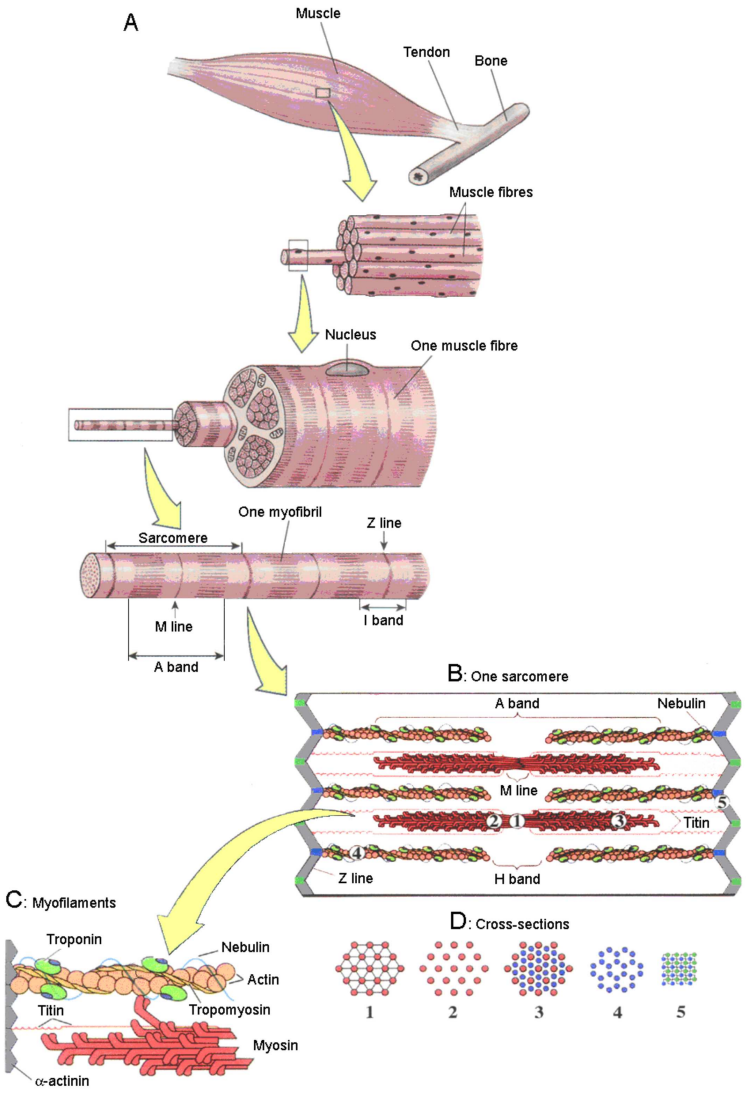

Figure 1.1: ***The different levels of organisation of the skeletal muscle structure.***
A. *From skeletal muscle to the myofibril.* **B**. *The structure of the sarcomere, thick myosin-containing filaments in red and thin actin-containing filaments in orange.* **C**. *Details of the myofilaments structure, with the contractile, regulatory and structural proteins.* **D**. *Cross-sections at different positions along the sarcomere, revealing the lattice organisation.*

thick filaments, hence the slightly lighter colour. The lighter appearance of the I bands at the edges of the sarcomere results from the presence of only thin filaments. During fibre shortening the extension of the A band, defined by the length of the thick filament, remains constant, while the I bands and the H band shorten. This is the indication of the fact that the shortening occurs due to the relative sliding of the thin past the thick filaments towards the centre of the sarcomere, increasing the overlap between filaments, and not by a change in their length [1, 2]. As shown in Figure 1.1 D, cross-sections of vertebrate myofibrils reveal that thick and thin filaments are organised into a double

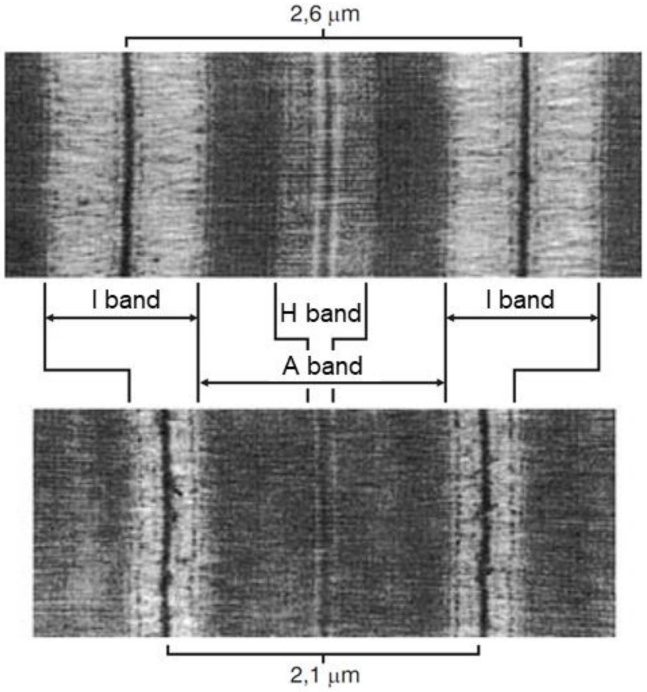

Figure 1.2: ***Electron microscopy images of the striated appearance of the myofibrils at two different sarcomere lengths.***
Top. *Sarcomere length* 2.6 µm. Bottom. *Sarcomere length* 2.1 µm. *Sarcomere length contraction occurs with the shortening of I and H bands width without any change in the A band. (Figure from W.J. Germann, C.L. Stanfield, Principles of human physiology, Benjamin-Cummings Pub Co)*

hexagonal lattice: in the overlap zone of the A band each thick filaments is surrounded by 6 thin filaments, and each thin filaments by three thick filaments, while cross-section through the I bands or the H band shows only the presence of the thin or the thick filament array respectively. At each Z line thin filaments are arranged in a tetragonal pattern, and each thin filament is connected with four other thin filaments from the subsequent sarcomere.
After this brief summary of the structure of a striated muscle cell we will introduce the functionality of the myofibril.

1.1.2 The thick filament and the myosin motors

The functional unit of the striated muscle cell is the half-sarcomere (hs). In the half-sarcomere myosin motors work in parallel as independent force generators, as the linear relation between the force developed during isometric contractions and the degree of filament overlap demonstrates [3]. A myosin molecule is a two-headed dimer consisting of six polypeptides: two heavy chains and two pairs of light chains, one for each heavy chain: one of regulatory light chains (RLC) and one of essential light chains (ELC). Each light chain is around one tenth of heavy chain's molecular weight. The N-terminal portion of the heavy chains forms two globular heads, each one of them associated with two light chains, while the C-terminal portion of the heavy chains interacts with each other forming

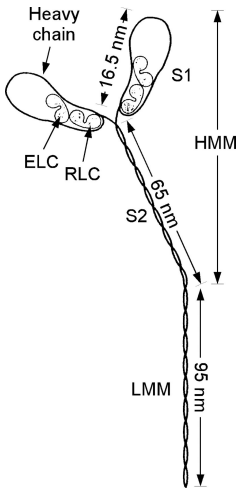

Figure 1.3: ***Schematic representation of the myosin II molecule.***
Myosin II molecule consists of two heavy chains and two pairs of light chains. Following proteolytic digestion heavy chains can be split in a globular portion (S1) and a tail (consisting of S2 and LMM). HMM is composed of S1 and S2 fragments. The S2 and LMM portions are arranged in a coiled-coil structure. Figure from (Hooper and Thuma, 2005)

a long double α-helix rod, or tail. The heavy chains can be enzymatically cut in two fragments, the light meromyosin (LMM), comprising a large part of the tail region, and the heavy meromyosin (HMM), consisting of two more portions, subfragments S1 ans S2. Subfragment S1, also known as the head, corresponds to the N-terminal globular part of the myosin molecule, and contains both the site for the hydrolysis of ATP that fuels the motor work, and the actin-binding site. The head domain sequence is strongly conserved among different myosin types. Subfragment S2, the neck, is a flexible α-helical coiled coil rod that links the head to the LMM on the thick filament backbone. See Figure 1.3 for reference. The thick filament is a 800 nm long bipolar structure, constituted by the polymerisation of the LMM in two antiparallel arrays, starting from the centre of the sarcomere, with the heads pointing towards the end of the sarcomere. On the thick filament, myosin heads are arranged in crowns along a three-stranded helix. Each crown is made of three pairs of heads, emerging at 14.3 nm intervals along the filament, with an angle of 120 °C between consecutive crowns. This results in an axial periodicity along the filaments of 42.9 nm. Taking into account that 100 nm of thick filament at the centre of the sarcomere are constituted exclusively by the overlap of antiparallel LMM, the number of myosin heads in the half-thick filament is $(800 - 100)/(6 \times 14.3) = 294$. The thick filaments contains also accessory proteins involved in the organisation of the filament structure and in the regulation of motor activity [4]. Such proteins are myosin-binding protein C and titin, a gigantic protein that spans the whole length of the half-sarcomere in the I band from the Z line to the tip of the thick filament, and, in the A band, lying on the surface of the thick filament, up to the M line.
We define the working stroke as the conformational change in the actin-attached myosin motor responsible for the force generation and the filament sliding in rigor (ATP-free). A structural model of the myosin motor has been defined, with atomic resolution, with X ray crystallography. The S1 head is constituted by an N-terminal nucleotide-binding region,

a central region consisting of an upper domain and a lower actin-binding domain, and a C-terminal segment. The nucleotide-binding and the actin-binding regions constitute the motor domain, or catalytic domain (CD). The C-terminal portion, a α-helix connecting the head to the S2 α-helix, is called light chain binding domain (LCD), as it is associated to the regulatory and essential light chains. The comparison between the myosin head crystallographic structure in rigor (corresponding to the end of the working stroke) and a construct of S1 complex with non-hydrolysable ATP analogue, putatively corresponding to the beginning of the working stroke [5, 6], made it possible to estimate the movement related to the execution of the working stroke. According to the crystallographic model the working stroke consists in $\sim 70°$ tilting of the LCD about the fulcrum at the basis of the CD, that is firmly attached to the actin filament. The LCD acts as a lever arm that amplifies the movement of the head-rod junction up to 11 nm axial displacement between the CD and the thick filament backbone (tilting lever arm model) [7].

1.1.3 The structure and the regulation of the thin filament

The thin filament consists primarily of monomers of globular actin (G-actin), constituted by two lobes separated by a deep cleft. In the presence of ATP, under physiological conditions, G-actin monomers spontaneously polymerize forming a filamentous actin (F-actin). The thin filament is composed by two F-actin strands coiled around each other in a double right-handed helix, with a half-periodicity of 36.5 nm [8]. Since actin monomers are asymmetrical, and they are all oriented in the same direction, the actin filament has a polarity with two distinguishable ends: a rapidly polymerizing end ("barbed" or (+) end), and a slow polymerizing one ("pointed" or (−) end). All actin subunits are oriented with their cleft, that contains the ATP binding site, towards the (−) end. In the sarcomere, the (+) end is anchored to the Z line at the sarcomere edge, while the (−) end extends towards the M line. Binding sites for myosin occur every 5.5 nm along the same strand of an actin filament, and myosin movement along the actin occurs only towards the (+) end, so that the actin filament slides in the direction of the (−) end, towards the M line. Structural studies performed on insect flight muscles provided evidence for myosin heads binding preferentially to "target zones" on the actin filament [9, 10]; rabbit skeletal myosin II was described to have target zones every 36 nm along actin [11], that is what expected from binding along one face of the actin filament with minimal azimuthal reorientation. In the striated muscle of vertebrates the thin filament is not only composed of F-actin: the filament unit also includes two regulatory proteins that allow the interaction between actin and myosin with presence of Ca^{2+}. One of these proteins, the tropomyosin (Tm), is a rod-like coiled-coil dimer that lies along the α-helix of actin filaments, forming a polymer that lays along the actin filament that lays from (−) to (+) end. Every tropomyosin molecule covers seven actin monomers and each tropomyosin dimer can bind one troponin complex, the other regulatory protein. The troponin complex (Tn) consists of three subunits: the calcium-binding troponin C (TnC), the actin-binding inhibitory troponin I (TnI) and the tropomyosin-binding troponin T (TnT) [12]. TnC consists of two globular N-terminal and C-terminal regions connected by a long helix [13], and acts as a Ca^{2+} sensor in muscle regulation. The C-terminal domain contains sites with high affinity for Ca^{2+} and sufficient for Mg^{2+}, so that in relaxed conditions they are normally occupied by Mg^{2+}, while the N-terminal

domain has low affinity sites but is highly selective for Ca^{2+} [14]. In the absence of Ca^{2+}, tropomyosin position covers the potential myosin-binding sites on actin. Upon depolarization of the cell membrane, Ca^{2+} is released from the sarcoplasmic reticulum, and binds the troponin C, inducing structural changes in the N-terminal domain that result in the exposure of hydrophobic residues, that strengthen TnI/TnC binding [15], and weaken TnI/actin interactions [16, 17]. The consequent interaction of TnI with TnT and Tm, and the remodelling of TnT, cause an azimuthal movement of Tm on the thin filament that exposes binding sites on actin, allowing the attachment of myosin crossbridges, and enabling cyclic interaction between actin and myosin.

1.1.4 The chemo-mechanical acto-myosin ATPase cycle

The basic principles of the force-generating crossbridge cycle in striated muscle have been elucidated on the basis of structural, mechanical, biochemical data [18–25]. Steady force and shortening in muscle contraction are the result of asynchronous cyclic interactions between myosin motors and actin, driven by adenosine triphosphate (ATP) hydrolysis on the catalytic site of the myosin motor. In this respect myosin is an enzyme capable of converting chemical energy into mechanical energy.
Molecular motors can be classified as processive or nonprocessive, depending on whether they can continuously slide along their track for a long distance by undergoing many ATP hydrolysis cycle, or they detach from their track at the end of each ATPase cycle. The myosin II motor of muscle is classified as nonprocessive. This implies that each myosin II motor domain spends most of its ATPase cycle time detached from actin, while other motors are driving filament sliding. This results in an efficient way of operation for a motor working in an ensemble. The production of force and shortening in striated muscle is therefore the result of asynchronous cyclic interactions of myosin motors with actin filaments in each half-sarcomere.
The model that defines the biochemical steps of ATP hydrolysis cycle of the actin-myosin complex was suggested in 1971 by Lymn and Taylor, with fast solution kinetic studies [20]. The cycle can be schematically described as follows (see Figure 1.4). In the absence of ATP, the myosin head extending from the thick filament is tightly bounded to an actin monomer on the nearby overlapping thin filament. As soon as an ATP molecule is available it rapidly binds to a myosin head, reducing myosin affinity to actin, and the acto-myosin complex dissociates (M−ATP + A). The binding of ATP and the detachment from actin promote a structural change with a tilt of the LCD, the lever arm (a recovery stroke). ATP is hydrolysed into ADP and Pi (M−ADP−Pi), which increase again the affinity for the actin. Binding of the myosin head to an actin monomer causes the reduction of the affinity between myosin and ATP hydrolysis products, which are then released: Pi is released first, then ADP. In the absence of actin, the Pi release is the limiting step of the ATP hydrolysis cycle. The release of Pi from actin-bound myosin is associated with a large drop in the free energy and thus is the step associated with the working stroke, which may be more or less modulated by the loading condition. The working stroke thus result either in force generation or sliding motion between the thin and thick filaments, depending on the mechanical condition (isometric or isotonic contractions). In the acto-myosin complex the rate of ADP release increase with the execution of the working stroke. Following ADP release, another ATP binds to myosin,

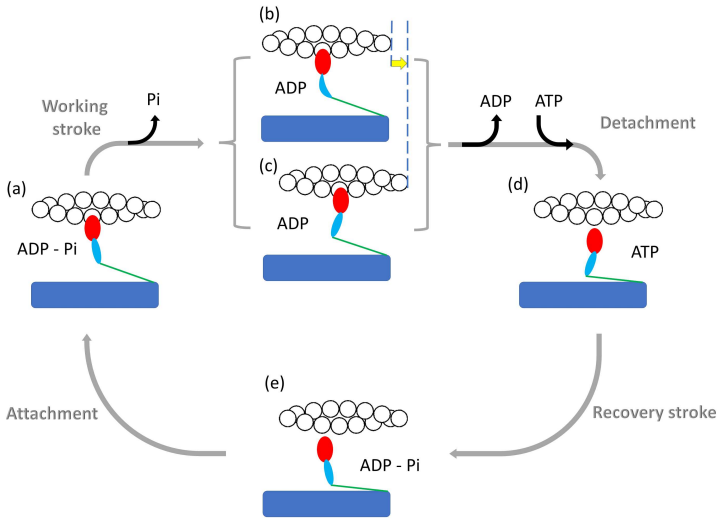

Figure 1.4: ***Schematic diagram of the chemo-mechanical cycle of the myosin motor during its interaction with the actin filament.*** *The HMM fragment of the myosin molecule is a dimer with each monomer made by the sub-fragment* 1 *(*S1 *or head containing the motor domain (red) and the light chain domain (the lever arm, violet)) and the subfragment* 2 *(*S2 *or tail, green) extending from the myosin filament backbone (blue). For simplicity, only one* S1 *and* S2 *are represented here. The myosin·ADP·Pi complex attaches to actin (white circles)* (a)*, forming the cross-bridge, which triggers the tilting of the lever arm and Pi release with generation of force and actin filament sliding. If the mechanical load sufficiently high it opposes the filament sliding, and the tilting of the lever arm causes the increase of the strain in the system, represented here by the distortion of the lever arm* (b)*. If the load is sufficiently low* (c) *tilting of the lever arm causes actin filaments sliding (yellow arrow), keeping the strain low. ADP release from and ATP binding to the motor domain cause myosin detachment from actin. ADP release is slower at high load,* $(b) \rightarrow (d)$*, and becomes faster at lower load* $(c) \rightarrow (d)$*. Hydrolysis of ATP in the detached head and reversal of the lever arm tilting (recovery stroke,* $(d) \rightarrow (e)$*) completes the cross-bridge cycle. The absence of ATP causes the cycle to stop before detachment so that all motors stay attached to actin (rigor).*

and the cycle restarts. During isometric contractions the muscle does not produce any mechanical power in spite of active crossbridge cycles, while the working stroke produces only the stretching of the elastic components, see Figure 1.4, state (b) . Calorimetric studies demonstrated that a very small enthalpy change occurs upon ATP hydrolysis, with ADP and Pi remaining in the myosin catalytic site, and that the largest enthalpy change occurs with the release of Pi [26]. The large enthalpy change measured in solution studies indicates that Pi release is associated with the execution of the working stroke. ADP release can occur either from the strained state or in the state at the end of the working stroke, when the load opposing the stroke is low. The ADP release rate is conformation dependent thus is the rate-limiting step during muscle contraction at high load. This explains how both ATPase rate and energy liberation rate increase with the reduction of load. Recent *in situ* experiments suggest that the working stroke and the

release of Pi are independent processes, even if the rate constant of Pi release increases with the progression of the working stroke [27, 28].
Due to the myosin II organization in array in the bipolar thick filament, steady force and shortening are generated by cyclic interactions between actin and each myosin motor, which is mechanically coupled to the other motors via the thick filament backbone. This arrangement allowed myosin II to evolve toward very rapid interactions with actin to prevent a motor at the end of the stroke to resist to the action of the others, consequently, the the fraction of the ATPase cycle spent by myosin in the bound state, the duty ratio r, must be small and reduce with the reduction of the load and the increase of shortening velocity. The duty ratio drops from 0.3 in isometric conditions to 0.05 in unloaded conditions, which implies that no more than 5% of motors are attached to actin at any moment [29, 30]. Myosin II organization in array provides that, after detaching from actin, the motor remains in the proximity of the thin filament, while the actin sliding continues because of the action of the other motors. Consequently, a motor keeps moving along the actin filament during the same ATPase cycle so that the sliding distance per molecule of ATP hydrolysed is more than one order of magnitude larger than the sliding promoted by its interaction with actin alone. More precisely, if the sliding distance accounted by the working stroke d is $\sim 10\,\mathrm{nm}$, the relative distance achieved during its ATPase cycle is $D = d/r = 10\,\mathrm{nm}/0.005 = 200\,\mathrm{nm}$.

1.1.5 Scaling factors of the mechanical parameters of the striated muscle from the tissue to the molecular level

In the previous Section we described the coupling between biochemical, structural and mechanical steps in the generation of force and shortening by the myosin motor in the half-sarcomere. The efficiency and control of this process is optimized by the assembly of the contractile proteins (actin and myosin), and regulatory proteins into highly ordered structures on different levels of hierarchical organization [31]. The ordered repetition of the sarcomere along and across the myocyte produces a magnification factor between the mechanical properties of the sarcomere and those of the muscle, while the relevant parameters that define the muscle performance (force, shortening velocity, power, energy rate) remain the same, provided the normalisation due to the scale factor. Specifically, the force generated in each of the two half-sarcomere is directly proportional to the overlap degree between the thick and the nearby thin filaments, as the number of available myosin motors working in parallel in each half-thick filament scales down with the reduction of the overlap. The force exerted by the two half-sarcomeres is not additive, and it must be the same as they are arranged in series. Accordingly, the force remains the same throughout the whole chains of half-sarcomeres along the whole myofibril. Myofibrils are orderly packed inside the myocyte, as well as myocytes inside the tissues. Therefore, given a constant structure of the half-sarcomere, different muscles generate different forces in relation to their cross-sectional area (CSA), and the force per CSA of vertebrate striated muscle is relatively constant, around $200 - 300\,\mathrm{kN\,m^{-2}}$. Since there are about 5×1014 thick filaments per square metre in the striated muscle, each thick filament exerts a force of $400 - 600\,\mathrm{pN}$. With 294 myosin motors on each thick filament, the average force per motor would be around $1.4 - 2\,\mathrm{pN}$. However, during the isometric contraction $r \sim 0.3$, meaning that only 1/3 of motors are attached to actin at the same

time. The average force exerted by an attached motor can therefore be estimated to be $4 - 6$ pN. Throughout a myofibril the half-sarcomeres are arranged in series, so that their changes in length results to be additive. The working range of sarcomere length *in vivo*, for most vertebrate striated muscles, is between 2.4 and 2 µm, so that against loads lower than the isometric force, the active shortening spans to 20% of the sarcomere resting length. Considering a length of 1.1 µm for the half-sarcomere, this means a shortening of 200 nm. Accordingly, for a muscle fibre, the shortening will be the product of 200 nm times the number of half-sarcomeres in series along the cell.

1.1.6 The force-velocity relation and the maximum power

In isometric contraction, the tilt of the lever arm raises the force exerted by the half-sarcomere, increasing the strain of all the elastic elements (see Figure 1.4, state (b)). When the load is lower than the maximum steady force exerted under isometric conditions T_0 (that is conventionally expressed as force per cross-sectional area of the contractile material, in kN m^{-2}), lever arm tilting results in relative filament sliding with a reduced strain in the elastic components (see Figure 1.4, state (c)). The shortening velocity V is inversely proportional to the force T (force-velocity relation, $T - V$ [32]). At physiological concentrations of ATP, ADP release is the rate-limiting step for motor detachment from actin (step (b)/(c) $\rightarrow$ (d)). The rate of ADP release is conformation-dependent, increasing during steady shortening when motors at the end of the working stroke would become negatively strained. This explains the increased rate of energy liberation $\dot{E}$ (and the underlying ATP hydrolysis rate, ϕ) when the load is reduced and the shortening speed is increased [18, 32–38]. Faster detachment of negatively strained (compressed) motors prevents the ones at the end of their working stroke to oppose positively strained motors, a requirement for the maximisation of the efficiency of an array of motors working in parallel.
The power P (the product $T \times V$) exerted by the contracting muscle varies according to the mechanical conditions: P is zero in the isometric contraction, when $T = T_0$ and when $V = 0$, is again zero during shortening at the maximum velocity V_0 when $T = 0$, and attains a maximum for loads around 1/3 T_0 (or $V = 1/4\ V_0$). During an isometric contraction and during shortening at the maximum velocity, the whole energy consumption is liberated as heat, so that the mechanical efficiency ϵ which is the ratio of power over the rate of energy liberation ($\epsilon = P/(P + \dot{H})$, where $\dot{H}$ is the rate of heat production), is zero. In the isometric contraction the rate of energy liberation accounting for the steady force T_0 (denoted $\dot{E}_0$) is minimum and corresponds to the rate of heat production $\dot{H}_0$ [32].

1.1.7 Different performance of fast and slow skeletal muscle isoforms

The performance of different types of skeletal muscles depends on the myosin II isoform expressed in the muscle cells. Skeletal muscle of different mammalian species contains four major myosin heavy chain isoforms [39]:

– a slow isoform: β-MHC (MHC-1)

– three fast isoforms: IIa-MHC, IIb-MHC, IIx-MHC (MHC-2)

and three major myosin light chain isoforms:

– a slow isoform: MLC1s

– two fast isoform MLC-1f, MLC-3f

Differential distribution of the MHCs isoforms defines four major fibre types (containing a single MHC isoform), and a number of intermediate hybrid fibre populations containing two isoforms: β-IIa, IIa-IIx, and IIx-IIb. Both MHC and MLC isoforms determine the maximum shortening velocity of skeletal muscle fibres.
Specifically, slow muscles, which are involved primarily in maintenance of posture and are characterised by the dominant presence of the isoform 1 of Myosin Heavy Chain (MHC-1 isoform), exhibit lower shortening speed at any given load, thus develop lower power and consume ATP at a lower rate than fast muscles which are involved in movement and are characterised by the dominant presence of the isoforms MHC-2A, -2B or -2X isoforms [40]. Strikingly, the functional difference between slow and fast isoforms is due to a difference of only 20% in the amino-acid composition.
During an isometric contraction, when the power is zero, the rate of energy consumption accounting for the steady force T_0 is measured by the rate of heat production ($\dot{H}_0$) [32]. $\dot{E}_0$ has been found $\sim$ 5-fold larger in fast muscles than in slow muscles [41–44]. The underlying rate of ATP hydrolysis at T_0 can be obtained from $\dot{E}_0$ by dividing it by the energy liberated per molecule of ATP hydrolysed ($\Delta G_{ATP} = 60\,\mathrm{kJ\,mol^{-1}}$ in mammalian muscle according to [45]). In this way the energetic cost of the isometric force in the intact muscle can be compared with that in the demembranated fibres, in which the rate of energy liberation is determined by measuring the rate of ATP hydrolysis. A further normalisation for the concentration of myosin motors in the mammalian muscle (0.18 mM, [42]) gives the rate of ATP hydrolysed per myosin motor ϕ. In demembranated fibres of rat fast muscle [46, 47], rabbit [48, 49] and human muscle [50] at 12 °C, ϕ is 5-fold (or more) larger than in slow muscle, in agreement with muscle measurements. In both fast muscles [41–44] and fast demembranated muscle fibres [46–49] T_0 is either similar or at max 1.5-fold larger than in slow muscles and muscle fibres. Thus the tension cost of the isometric contraction $\dot{E}_0/T_0$ results to be systematically larger in fast muscles by on average 5-fold (with a minimum of 3-fold). The justification for the elevated tension cost of the fast muscle can be only partly found in the intrinsic larger actin-activated myosin ATPase in solution, which for the fast myosin is twice that of the slow myosin [51].

1.2 From *in situ* to *in vitro* studies of muscle myosin II

Since the ordered arrangement of myosin motors in the sarcomere is of fundamental importance for the efficiency of the skeletal muscle, until a few years ago the mechanical properties of myosin II as a collective motor could be described only *in situ*, where the preserved filament lattice allows for a proper description of the functionality of the contractile proteins. However, the bulk of data characterising the energetics of slow and fast muscles at cell and tissue levels, first of all the $\sim$ 5-fold larger isometric tension cost, leaves open the question of the underlying molecular mechanism. Inferring the definition of the molecular mechanism from cell and tissue is complicated by the scaling factors related to the structural organisation of the molecular motors in the

three-dimensional lattice, the co-presence of different isoforms in the same muscle and even in the same muscle fibre and the possible confounding contribution of the other sarcomeric (cytoskeleton and regulatory) proteins. Even assuming that the tension cost is solely related to intrinsic properties of the motor isoform, the question remains about the role played by the differences in the mechanokinetic properties of the motor, as the force developed in a single motor interaction or the fraction of the ATPase cycle time each motor spends attached (the duty ratio) while working *in situ* in the half-sarcomere of the striated muscle. *In situ* studies with demembranated fibres, from frog and mammalian muscle, it was possible to investigate the coupling between mechanical and chemical steps [27, 28, 52], but the physiological responses at the sarcomere level are less consistent in these studies, mainly due to the loss of sarcomeric order. For these reasons, the development of *in vitro* techniques, as the *in vitro* motility assay (IVMA) [53, 54], constituted a fundamental advance for the study of the chemomechanical properties of the motor proteins. This method, however, presents both conceptual and methodological shortcomings: the properties emerging from the sarcomeric array arrangement of myosin II are lost, as well as the possibility to control the load.

Single molecule mechanics have been extensively employed for the study of motor proteins; in particular, combined with single molecule fluorescence, they can be used to define how force and movement are related to structural changes within the motor, or how they are coupled to a given step in the ATP hydrolysis cycle [55, 56]. Optical trapping techniques have been extensively employed to study the mechanics of motor proteins working in the nanometer-piconewton scale [22, 57]. In laser trap experiments, a focused laser beam is used to trap dielectric particles, with an index of refraction higher than the surrounding medium, in a three-dimensional potential well centred near the focal point [58]. A relevant feature of this method is that for a few hundreds of nanometers displacement from the equilibrium position, the optical trap displays virtual Hookean spring properties, so that the force exerted on the trapped particle can be measured by following bead displacement from its equilibrium position in the trap centre. Further details on the Optical tweezers setup can be found in Appendix A. The maximum force attainable within the linear response region is $\sim 50\,\mathrm{pN}$ (with a laser power of $100\,\mathrm{mW}$), and the force resolution is approximately $0.1\,\mathrm{pN}$. In optical tweezers experiments the protein of interest is typically associated to a trapped microscopic bead (of silica or polystyrene), and is brought into contact with a partner to exploit their interaction.

A special configuration of the laser trap developed to study the mechanics of myosin II is the Three-Bead Assay (TBA) [22]. In this setup the laser is split in two optical traps, each holding a bead attached to one end of an actin filament, that is suspended over a myosin motor attached to a third fixed bead. Due to its very low duty ratio, muscle myosin II spends only a small fraction of the ATPase cycle time attached to the actin filament, and TBA configuration is essential in preventing the myosin molecule from flying away under thermal agitation when it is detached during its fast intermittent interactions with actin. The actin-myosin interactions are detected from noise reduction of the bead position signal due to the increased stiffness of the system, and while this method allowed the measurements of single myosin-actin interactions [22, 59, 60], it is generally inadequate to measure the force and the load dependence of the movement, because the force development during a single myosin-actin interaction is affected by the large compliance of the optical trap. Moreover, single actin-myosin events can be detected only if the duration of actin attachment (and therefore the duty ratio) is increased by

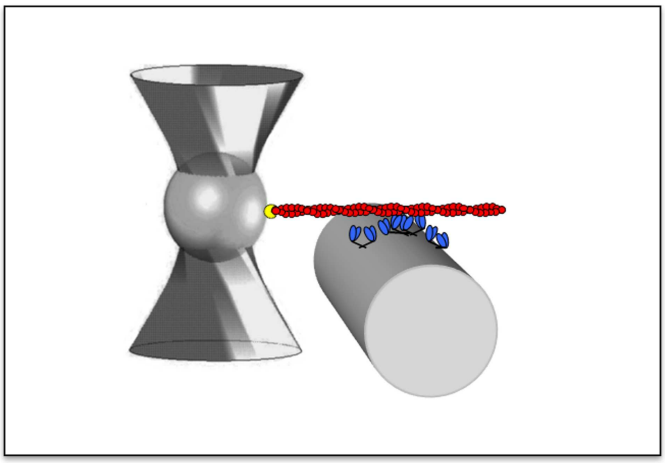

Figure 1.5: ***Schematic representation of the myosin-based nanomachine.*** *The array of myosin motors (in blue) is deposited on the surface of a pulled glass pipette carried by a piezoelectric nano-positioner, and interacts with an actin filament (in red, length* $\sim 10\,\mu m$*) attached with the correct polarity, via gelsolin (in yellow), to a polystyrene bead trapped in the focus of the Dual Laser Optical Tweezers. Figure from [61].*

reducing the ATP concentration down to $\sim 50\,\mu M$ (two orders of magnitude lower than the *in situ* physiological value, 2 mM), which prevents performing kinetic studies in physiological conditions.
This brief introduction to single molecule mechanics studies, which generated impressive advancement in the knowledge of the mechanism of unconventional myosins and non-myosin motors (like kinesin or dynein), highlights three major limits for the possibility to be used to study myosin II from skeletal muscle. First of all there is an intrinsic impossibility to detect the cooperative effects derived from the arrangement of myosin II in ensemble. Secondly, the impossibility to measure isometric force or the displacement when the load is high, due to the low duty ratio of the motors, and to the high intrinsic compliance of laser trap measurements. Lastly, the need to prolong the time of interaction between actin and myosin to be able to detect it, achieved by lowering ATP concentration to sub-physiological values, alters the kinetics of the process. Specifically, while under physiological conditions ATP binding and detachment are very fast, when the ATP is very low the kinetics of the process is dominated by the second order rate constant for ATP binding.
These limitations can be overcome by studying the mechanical properties of myosin II in a synthetic nanomachine, in which an array of myosin II motors purified from skeletal muscle, interacts with a single actin filament attached with the correct polarity to a bead trapped in the focus of a Dual Laser Optical Tweezers (DLOT), which, unlike the single laser trap, has the dynamic range of force and movement adequate for myosin working in arrays [61] (see Figure 1.5).

1.3 The functional differences between slow and fast myosin isoforms investigated with the synthetic sarcomere-like nanomachine

The definition of the emergent properties of the half-sarcomere became recently accessible by exploiting the DLOT technique for mechanical measurement on a nanomachine made by a small ensemble of myosin motors interacting with an actin filament [61]. The nanomachine allows the performance of the half-sarcomere (the generation of steady force and shortening), to be mimicked *in vitro* by an ensemble of pure myosin isoforms interacting with the actin filament, without the confounding effects of other sarcomeric proteins and higher hierarchical levels of muscle organisation. In the nanomachine a small number of HMM fragments extending from the functionalised surface of a micropipette, carried on a three-way nanopositioner acting as a length transducer, interact with an actin filament attached, with the correct polarity, to a bead trapped by the DLOT, acting as a force transducer. In solution with physiological ATP concentration the two motors of each dimer act independently [61]. Under this condition, myosin motors, after entering in contact with the actin filament, establish continuous interactions underpinning force development to a steady maximum value (equivalent to the force generated by the muscle in isometric contraction). In the original design [61] the system was operated either in position clamp to reproduce the isometric contraction, or in force clamp to reproduce isotonic contraction. The major limitation of the nanomachine working in position clamp was the large trap compliance in series with the motor array, two order of magnitude larger than the native compliance in series with the half-sarcomere. As a consequence, each addiction-subtraction of force by individual motor attachment-detachment induce substantial sliding undermining the condition of independent force generators of the motors in the native half-sarcomere. Therefore, in position clamp, the kinetics of the attached motors is influenced by the push-pull experienced when actin slides away-toward the bead for the addition-subtraction of the force contribution by a single motor (see [61], Supplementary Figure 7). In the experiments described in this work the system has been implemented to operate in length clamp. In length clamp mode the sliding between the actin filament and the motor array caused by force generating interactions is eliminated because any movement of the bead is counteracted by the movement of the nanopositioner. This protocol, that will be detailed in the next Chapter, allows the condition of the motors as independent force generators in the array to be recovered, and the rate of development of the steady isometric force as well as the force fluctuations superimposed on the steady force are direct expression of attachment/force-generation and detachment of the myosin motors. In the following Chapters we will show how the data collected from slow and fast myosin isoforms are used to feed a stochastic model providing a self-consistent estimate of all the relevant mechanokinetic parameters of the isometric performance of the motor ensemble: the force of a motor f_0, the fraction of actin-attached motors r, and the rate of transition through the attachment-detachment cycle ϕ, without assumptions from cell mechanics and solution kinetics as in previous studies [61–63].

The combined experimental and theoretical achievements reported in this Thesis set the stage for any future study on the emergent mechanokinetic properties of an ensemble of myosin molecules, either engineered or purified from mutant animal models or human biopsies.

Chapter 2

Mechanical experiments

2.1 Methods: skeletal muscle HMMs

In this Section we present the methods and setup adopted for the mechanical experiments performed with the synthetic nanomachine powered by different HMMs purified from different mammalian skeletal muscle.

2.1.1 Preparation of proteins

Adult male rabbits (New Zealand white strain), provided by Envigo, were housed at *Centro di servizi per la Stabulazione Animali da Laboratorio* (CeSAL, University of Florence), under controlled conditions of temperature (20 ± 1)°C and humidity (55 ± 10)%, and were euthanised by injection of an overdose of sodium pentobarbitone ($150\,\mathrm{mg\,kg^{-1}}$) in the marginal ear vein, in accordance with the Italian regulation on animal experimentation (Authorisation 956/2015-PR) in compliance with Decreto Legislativo 26/2014 and EU directive 2010/63. Three rabbits were used for the experiments. HMM fragments of myosin were purified from rabbit soleus and psoas muscles as reported previously in [61, 62], The functionality of the purified motors was always preliminarily checked with *in vitro* motility assay. Actin was prepared from leg muscles of the rabbits according to [64], and polymerised F-actin was fluorescently labelled by incubating it overnight at 4 °C with an excess of phalloidin-tetramethyl rhodamine isothiocyanate [65]. For the mechanical measurements in the nanomachine, the correct polarity of the actin filament was pursued by attaching the (+) end of the filament to a polystyrene bead (3 µm diameter) (Bead-Tailed Actin, BTA, [66]) with either the Ca^{2+}-sensitive capping protein gelsolin [61] or the Ca^{2+} insensitive gelsolin fragment TL40 (Hypermol, Germany) [62, 63]).

2.1.2 Mechanical apparatus

The nanomachine allows the performance of the half-sarcomere (specifically the generation of steady force and shortening), to be reproduced by an ensemble of pure myosin isoforms interacting with the actin filament without the confounding effects of other sarcomeric proteins and higher hierarchical levels of organisation of the muscle. The mechanical apparatus, described in detail in [61], is depicted in Figure 2.1: HMM fragments of

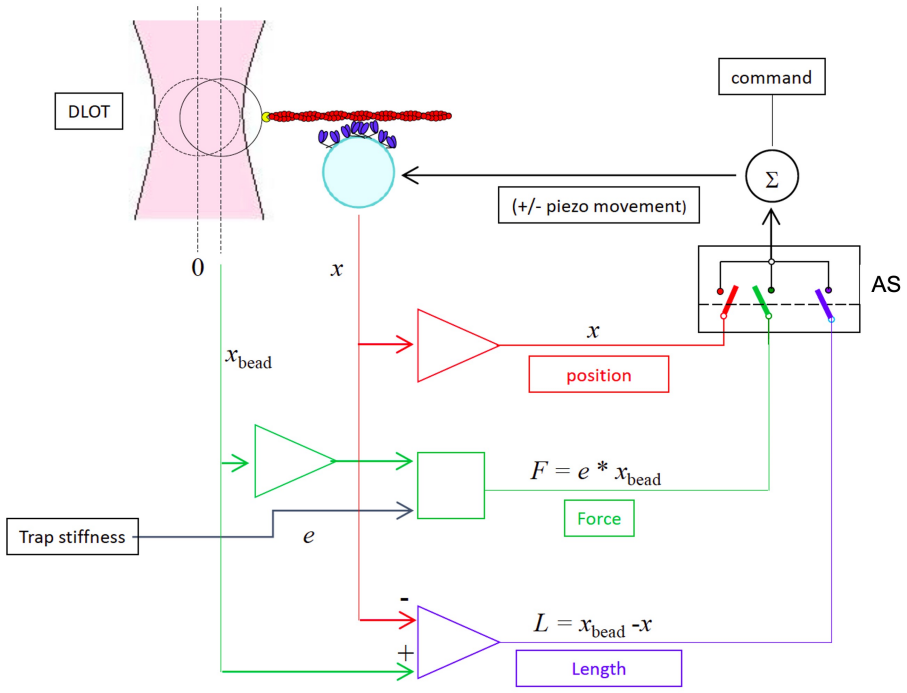

Figure 2.1: ***Block diagram of the system for nanomachine mechanics.*** *HMM fragments (blue) deposited on the functionalised lateral surface of a pulled micropipette (cyan) are brought to interact with the actin filament (red) attached with the correct polarity (+) via gelsolin (yellow) to the bead trapped in the focus of the DLOT (pink). Force generation produces the movement of the bead away from the focus of the DLOT. The switch selects the feedback signal that, together with the command (black), feeds the summing amplifier Σ that drives the piezo nanopositioner: in position clamp (red) the feedback signal is the position of the nanopositioner x carrying the support for the myosin array; in force clamp (green) the feedback signal is the force (F, calculated as the product of the stiffness of the trap (e) times the change in position of the bead x_{bead}); in length clamp (blue) the feedback signal is the change in the distance L between the position of the bead and the myosin array support.*

myosin were deposited randomly on the lateral surface of a glass pipette pulled to a final diameter of ∼ 3-4 µm and functionalised with nitrocellulose 1 % (*w*/*v*). The glass pipette was mounted in the flow chamber and carried on a three-way piezoelectric nanopositioner (nano-PDQ375, Mad City Lab, Madison WI, USA) that acts as a displacement transducer, and was brought to interact with an actin filament attached with the correct polarity to a bead trapped in the focus of a Dual Laser Optical Tweezers (DLOT) that acts as a force transducer. The DLOT system has a dynamic range for both force (0 − 200 pN, resolution 0.3 pN) and displacement (0 − 75 µm, resolution 1.1 nm) adequate for the measuring the output of the nanomachine. The buffer solutions used for all the experiments are already reported in [61] and contained physiological concentrations of ATP (2 mM) unless differently specified. 0.5 % methylcellulose was added to the running buffer in order to inhibit the lateral diffusion of F-actin [30] and minimise the probability of loss of acto-myosin interaction. The concentration of HMM from soleus and psoas muscle used

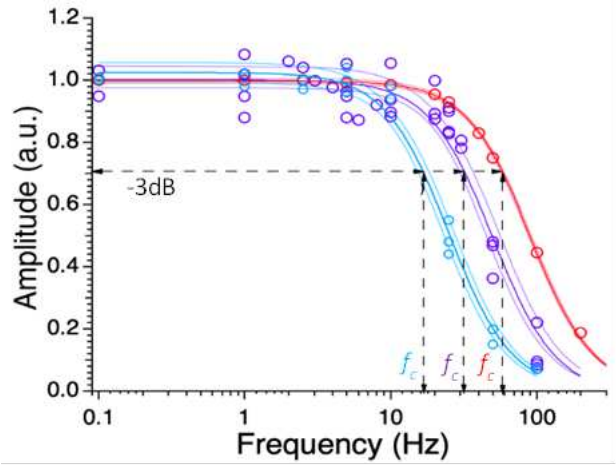

Figure 2.2: ***Power density spectrum of the system.*** *Superimposed power density spectrum either in position clamp (red circles interpolated by the red Lorentzian curve), or in length clamp with the array of actin attached motors in rigor from both fast muscle (violet circles and curve) and slow muscle (cyan circles and curve). The upper* $-3\,\mathrm{dB}$ *frequency* f_c *is:* $59 \pm 3\,\mathrm{Hz}$ *(red),* $31 \pm 6\,\mathrm{Hz}$ *(violet) and* $17 \pm 3\,\mathrm{Hz}$ *(cyan). The area delimited by thinner lines indicates the confidence limits.*

for the experiments was defined by the concentration at which the number of rupture events in rigor attained a saturating value.

This mechanical apparatus can be operated either in position clamp (to reproduce isometric contractions, Figure 2.1, red branch), when the feedback signal is the position of the nanopositioner carrying the motor array (x), or in force clamp (to reproduce isotonic contractions, Figure 2.1, green branch), when the feedback signal is the force (F), calculated as the product of the stiffness of the trap (e) times the change in position of the bead in the laser trap (x_{bead}). Recording of the nanomachine performance in true isometric condition, however, cannot be achieved in position clamp, due to the large trap compliance ($\sim 4\,\mathrm{nm\,pN^{-1}}$), which implies both several tens of nanometres movement to develop the maximum steady force and blunting of the force of individual attachment-detachment events (Supplementary Figure 7 in [61]). To eliminate the trap compliance the system has been implemented with a length clamp (blue branch in Figure 2.1), which uses as a feedback signal the change in distance (L) between the position of the actin attached bead in the laser trap (x_{bead}) and that of the nanopositioner (x), so that the movement of the bead with the force change is counteracted by the movement of the nanopositioner. In this way the effective trap compliance is reduced to $0.2\,\mathrm{nm\,pN^{-1}}$.

In length clamp the frequency response of the system is reduced by the propagation time of the mechanical signal through the loop from the force transducer to the nanopositioner, which also includes the array of actin attached myosin motors. The power density spectrum (PDS) of the system, measured with sinusoidal oscillations at different frequencies, changes depending on the selected feedback mode: in position clamp the PDS shows an upper $-3\,\mathrm{dB}$ frequency (or corner frequency f_c) of 59 Hz (Figure 2.2, red); in length clamp, when the feedback loop is closed with the array of actin-attached myosin motors in rigor, f_c decreases to 32 Hz with HMM from fast muscle (violet) and to 17 Hz with HMM from slow muscle (cyan). The mass of the system (m) is the same with either isoform array thus the different corner frequency between the two nanomachines should

almost in part depend on the different stiffness of the two arrays in rigor.
The architecture of the machine (with the length of the motor array much shorter than the length of the overlapping actin filament) implies that, for a given HMM concentration, the measured number of rupture events does not significantly change from experiment to experiment, therefore there is no need to normalise the mechanical response obtained in different experiments at physiological [ATP] by the actin filament length.
All the experiments were conducted at room temperature (24 °C).

2.2 Mechanical performance of the nanomachine powered by slow and fast myosin isoforms

In this Section we present the mechanical experiments that has been conducted employing the nanomachine powered by slow and fast myosin isoforms to investigate the molecular basis of the muscle contraction.

2.2.1 Estimate of the number of HMM molecules available for the interaction with the actin filament.

The number N of motors on the micropipette surface able to interact with the actin filament is initially determined by measuring the number of mechanical rupture events when the motor array is brought to interact with the actin filament in ATP-free solution, as in [61]. Following the formation of rigor bonds between the HMM-coated support and the actin filament (panel 1 in Figure 2.3 a), the HMM support is moved away from the actin filament, first by 1-2 µm in the direction orthogonal to the plane of the support, in order to raise a force from the trapped bead to the first bound HMM at an angle greater than 30° with the plane of the support, and then in the direction parallel to the plane, at constant velocity, to pull the motors away from the actin filament diagonally. This allows the first bonded HMM to undergo a pulling force that is higher than the axial component shared among the other motors. In this way the myosin–actin bonds brake one at a time and the attached motors cannot bind back once detached. Moreover, following each detachment the force drops because the length of actin filament segment between the bead and the next attached motor is transiently increased. Thus an additional pull is necessary to get to the next rupture event, the occurrence of which will vary in time according to the distance between the two neighbouring motors. With HMMs purified from soleus muscle the number of rupture events per interaction (Figure 2.3 b) attains a saturating value of 7.9 ± 1.1 ($n = 8$), with [HMM] used to coat the pipette of $0.2\,\mathrm{mg\,l^{-1}}$. A similar saturating value of rupture events, 8.1 ± 1.4 ($n = 8$), is obtained for the HMM purified from psoas muscle with a [HMM] of $0.1\,\mathrm{mg\,l^{-1}}$ (Figure 2.3 c). Notably, similar saturating values of [HMM] and number of rupture events (8.1 ± 1.2) were found for the psoas motors in the previous study in which an optical fibre etched to the same diameter was used as support [61]. In 2 mM [ATP] each head of an HMM dimer works independently and thus the number of available motors is twice the number of HMM ruptures: $N = 16 \pm 2$ and $N = 16 \pm 3$ for the soleus and psoas respectively.

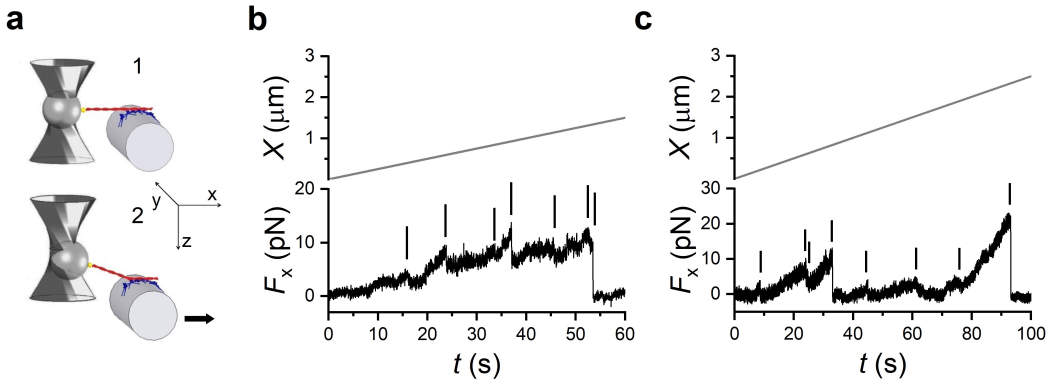

Figure 2.3: ***Estimating the number of HMMs available for actin interaction from rigor rupture events in ATP-free solution.*** **a**. 1. *Formation of the rigor bonds between the HMM array and the actin filament.* 2. *The motor support is moved away first in the direction (z) perpendicular to the plane of the actin-myosin interface and then in the direction (x) parallel to the plane, as indicated by the arrow. Panel modified from [61].* **b**. *Force (F_x, lower record) of an ensemble of soleus HMMs in response to the movement of the nanopositioner away from the actin filament in the x direction (upper record, velocity* $50\,\mathrm{nm\,s^{-1}}$*). The small vertical bars indicate the rupture events (force drop complete in less than* 50 ms*), the last of which corresponds to complete detachment of the actin filament.* **c**. *Records with the same protocol applied to an ensemble of psoas HMM.*

2.2.2 Isometric force development by the nanomachine powered by slow and fast myosin motors.

The experiment starts in position clamp, because, for the system to operate in length clamp, it is necessary that first the feedback loop is closed by the establishment of actin-myosin interactions. When an array of motors from the slow soleus muscle is brought to interact with a bead-tailed actin filament in solution with 2 mM ATP (Figure 2.4a), the establishment of continuous ATP-driven actin-myosin interactions causes the force (F, blue trace) to rise pulling on the actin filament, which in position clamp (HMM support position $x = 0$, red trace), slides in the shortening direction (ΔL, black trace, negative for shortening) due to the trap compliance (phase 1). A steady maximum force F_0 of $\sim$ 12 pN is attained with a shortening of $\sim$ 55 nm. The control is switched to length clamp in correspondence of the vertical dashed line separating phase 1 and 2. The switch time is marked by the increase in noise of the force trace as a consequence of the reduction of the compliance in series with the motor system. In fact, in length clamp the force change generated in each individual attachment and detachment is no longer dissipated in filament sliding against the large in series trap compliance. A shortening of $\sim$ 500 nm completed within $\sim$ 700 ms is superimposed on the steady isometric force in correspondence of the second vertical dashed line to drop and keep the force at zero (phase 3). When actin filament sliding stops (third vertical dashed line) force starts to redevelop towards F_0 (phase 4) with just a minimum delay, indicating that the motor array was able to cope with the imposed 500 nm shortening maintaining continuous interactions under zero load. The extent of shortening minus the amount taken by the trap compliance, ($500 - 55 = 445$ nm), divided by the time passed from the imposition of the shortening to the start of force redevelopment (0.88 s) gives an estimate of the

velocity of unloaded shortening V_0 of $0.5\,\mu m\,s^{-1}$. Force redevelopment in length clamp is much faster than the original force rise in position clamp and occurs in truly isometric conditions, as the movement of the bead due to trap compliance is counteracted by a corresponding movement of the nanopositioner in the lengthening direction (red trace, $\sim 55\,nm$), that keeps $\Delta L = 0$ (black trace). Notably, the force redevelopment following a 500 nm release attains the same F_0 value as that attained during the original rise in position clamp thanks to the architecture of the machine, in which the dimension of the motor array remains constant independently of the amount of reciprocal sliding [61]. The isometric value of the force obtained from 33 records shows a Gaussian distribution with centre 10.5 pN (Figure 2.4 b). The rate of force redevelopment in length clamp only depends on the attachment/detachment kinetics of myosin motors in isometric conditions. Force redevelopment is roughly exponential, and its time course is quantified by the rise time t_r (the time from 10% to 90% of F_0). The rise time estimated on the record (Figure 2.4 c, black) obtained by averaging the 6 traces from as many experiments (grey) is $t_r = 238 \pm 13\,ms$. The time constant τ of the underlying exponential force rise of the soleus powered nanomachine is $\tau = t_r/2.2 = 108 \pm 5\,ms$, and the rate of force development, a is $a = 1/\tau = 9.3 \pm 0.5\,s^{-1}$. The sequence of events accompanying the interaction of the array of motors purified from psoas muscle with the actin filament is the same as for the soleus motors (Figure 2.4 d). The force develops in position clamp (phase 1), while the actin filament slides in the shortening direction due to the trap compliance. A steady isometric force F_0 (15.9 pN), is attained with a shortening of 70 nm. In the 47 records of the psoas HMM F_0 shows a Gaussian distribution with centre 17 pN (Figure 2.4 e). Following the switch to length clamp, a rapid shortening of $\sim 500\,nm$ is imposed so that the force drops to zero. The shortening in this case is just sufficient to drop the force to zero, given the much faster shortening velocity afforded by the fast motor array, so that, as soon as the actin filament sliding stops (third vertical dashed line), V_0, calculated by the extent of shortening minus the amount taken by the trap compliance, $(500 - 70 = 430\,nm)$, divided by the time passed from the imposition of shortening to the start of force redevelopment (0.22 s), is $1.95\,\mu m\,s^{-1}$ (3.9 times larger than that of slow muscle). It must be considered, however, that V_0 in this case is somewhat underestimated, as most of the shortening occurs with force greater than zero. Force redevelopment in length clamp (phase 4) occurs with a rate that is not influenced by the trap compliance and thus is the expression of the kinetics responsible for the transition to the steady force F_0 by the fast isoform array. A rise time of $t_r = 77 \pm 4\,ms$ is estimated on the record (black in Figure 2.4 f) obtained by averaging the traces from 7 experiments (grey). The corresponding time constant is $\tau = t_r/2.2 = 35.0 \pm 1.8\,ms$ and the rate of force development is $a = 1/\tau = 28.6 \pm 1.4\,s^{-1}$.
The $-3\,dB$ upper frequency characterising the force rise $f_c = 0.35/t_r$ is $4.5 \pm 0.2\,Hz$.
Two main aspects emerge from these measurements on the synthetic machine operating in length clamp conditions. The first is that the rate of force redevelopment, which only depends on the attachment/detachment kinetics of myosin motors in isometric conditions, is three times slower in the soleus powered nanomachine than in the psoas powered nanomachine. The second point is that the force fluctuations around the average value displayed by the force record at the steady state are stemming from individual attachment/detachment events.
Both pieces of information will be used to feed the stochastic model described in the next Chapter.

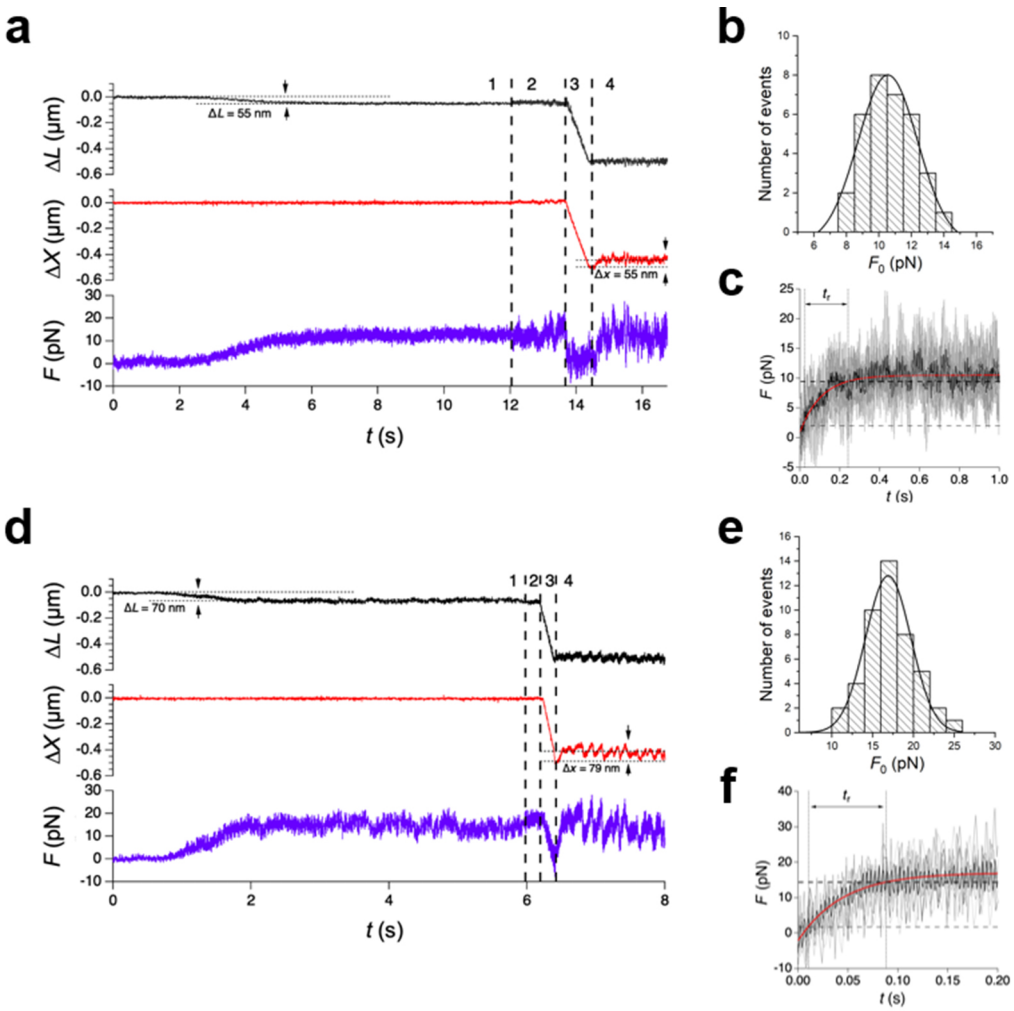

Figure 2.4: ***Caption in the next page.***

Figure 2.4: ***Active force generation by the nanomachine powered by slow (soleus) and fast (psoas) myosin motors.***
a - **c**. *Slow myosin array.* **a**. *Force (F, blue trace), movement of the nanopositioner carrying the motor array (Δx, red trace) and relative sliding between the motor array and the actin filament (ΔL, black trace) during the actin myosin interaction. Phase* 1*: following the establishment of the contact between the actin filament and myosin motors, the force rises in position clamp to the maximum isometric value ($F_0 \simeq 12\,\mathrm{pN}$), with the simultaneous sliding of the actin filament by $\sim 55\,\mathrm{nm}$ toward the shortening direction to load the trap compliance. Phase* 2*: the switch to length clamp (marked by the first vertical line) is followed by the increase in force fluctuations superimposed on F_0. Phase* 3*: force drops to zero in response to a rapid shortening of $\sim 500\,\mathrm{nm}$ imposed in length clamp (start marked by the second vertical line) with actin filament sliding under zero force. Phase* 4*: following the end of the imposed shortening (marked by the third vertical line) force redevelops in length clamp with the nanopositioner moving by $\sim 55\,\mathrm{nm}$ to counteract the trap compliance and keep the filament sliding at zero.* **b**. *Frequency distribution of F_0. Data are plotted in classes of $1\,\mathrm{pN}$ and fitted with a Gaussian (continuous line) with centre $10.5\,\mathrm{pN}$ and standard deviation $\sigma = 1.8\,\mathrm{pN}$.* **c**. *Time course of force redevelopment after rapid shortening (black trace) averaged from* 6 *records from as many experiments (grey traces). The red line is the single exponential fit to measure t_r (the time elapsed from* 10%*, horizontal thin dashed line, to* 90%*, thick horizontal dashed line, of F_0 recovery).* **d** - **f**. *Fast myosin array.* **d**. *F, Δx and ΔL, defined and colour coded as in* **a**. *Phases* 1 - 4 *as described in panel* **a**. **e**. *Frequency distribution of F_0 plotted in classes of $2\,\mathrm{pN}$ and fitted with a Gaussian (continuous line) with centre $17\,\mathrm{pN}$ and standard deviation $3\,\mathrm{pN}$.* **f**. *Time course of force redevelopment after rapid shortening (black trace) averaged from* 7 *records from as many experiments (grey traces). The red line is the single exponential fit to measure t_r labelled as in* **c**.

Chapter 3

Modelling the mechanical output of the nanomachine

In the previous Chapter we showed that the frequency response of the DLOT-nanopositioner system operated in length clamp is adequate to record the mechanical output of the nanomachine powered by an ensemble of either fast and slow HMMs.
In this Chapter we proceed to detail a stochastic model in which each molecular motor exists in three possible states (or motor configurations): one detached state and two different force-generating attached states. Such model has been developed to investigate the performance of a small ensemble of muscle myosin II, and thus characterise the mechanical output of the nanomachine.
In the last Section of this Chapter we will present the procedure adopted to feed the recorded time series of the fluctuations of the force exerted by the ensemble around the isometric steady state into the stochastic model.
Fitting the experimental records allows a self-consistent estimate of the relevant mechanokinetic parameters of the system, including the force exerted by a single myosin motor and the average number of attached motors in the stationary state, without assumptions from cell and solution kinetic studies.
The application of such procedure to experimental data sets obtained employing the mechanical apparatus detailed in the previous Chapter, will be the topic of Chapter 5.

3.1 The formalism of the master equation

As detailed in the previous Chapter, the implementation of the length clamp mode allows to recover the condition of myosin motors as independent force generators in the array. Therefore we consider an ensemble of N independent ATP-fuelled molecular motors interacting with an actin filament in isometric conditions. Each motor can be found in one of the three possible configurations, the detached state D, the attached low force-generating state A_1, or the attached high force-generating state A_2. The corresponding kinetic scheme for a single motor, which exemplifies the possible transitions between distinct allowed motor configurations is:

$$\mathrm{D} \underset{\mathrm{k}_{-1}}{\overset{\mathrm{k}_1}{\rightleftharpoons}} \mathrm{A}_1 \underset{\mathrm{k}_{-2}}{\overset{\mathrm{k}_2}{\rightleftharpoons}} \mathrm{A}_2 \xrightarrow{\mathrm{k}_3} \mathrm{D} \tag{3.1}$$

The kinetic rate constants k_j, $j \in \{1, -1, 2, -2, 3\}$ represent the probability per unit of time for the reaction j to occur, and are expressed in s^{-1}. In Appendix B we investigated a general version of the model in which the attached configurations are space-dependent. The state of the physical system constituted by the ensemble of motors, at any time t is characterised by the vector $\boldsymbol{n}(t) = \big(n_D(t), n_1(t), n_2(t)\big)$ whose entries specify the number of molecular motors in each of the considered configurations. Specifically, n_D stands for the number of motors in the state D, n_1 is the number of motors in the state A_1 and n_2 denotes the number of motors in the state A_2. Motors in the same configuration are referred in the following as belonging to the same population. The system admits the obvious conservation law $N = n_D + n_1 + n_2$ where N stands for the total number of motors in any of the considered states. Accounting for the above relation enables one to employ just two scalar (discrete) entries to photograph the state of the system, namely $\boldsymbol{n}(t) = \big(n_1(t), n_2(t)\big)$.
Under the Markov hypothesis, the stochastic dynamics of the scrutinised system is ruled by a master equation which sets the evolution of the probability $P(\boldsymbol{n}, t)$ of finding the system in the state specified by the vector $\boldsymbol{n}$ at time t. The master equation accounts for the balance of opposing contributions: on the one side the transitions *towards* the reference state (the associated terms bearing a plus sign). On the other, the transitions *from* the reference state (terms with a minus). The master equation can be cast in the general form:

$$\frac{\partial P(\boldsymbol{n}, t)}{\partial t} = \sum_{\boldsymbol{n'} \neq \boldsymbol{n}} \Big[T(\boldsymbol{n}|\boldsymbol{n'}) P(\boldsymbol{n'}, t) - T(\boldsymbol{n'}|\boldsymbol{n}) P(\boldsymbol{n}, t) \Big] \tag{3.2}$$

where $T(\boldsymbol{n'}|\boldsymbol{n})$ represent the transition rates from the state $\boldsymbol{n}$ to a new state $\boldsymbol{n'}$, compatible with the former. In the following, to identify the arrival/departure state $\boldsymbol{n'}$ we solely highlight the individual component of the vector $\boldsymbol{n}$ that changes due to the considered reaction. The explicit expression for the transition rates, as stemming from the chemical equations that define the stochastic single molecule dynamics (3.1), takes the following form:

$$\begin{aligned}
&\textit{ATTACHMENT} && T_1 = T(n_1 + 1|\boldsymbol{n}) = k_1 \, \frac{n_D}{N} = k_1 \Big[1 - \frac{1}{N}(n_1 + n_2) \Big] \\
&\textit{DETACHMENT} && T_{-1} = T(n_1 - 1|\boldsymbol{n}) = k_{-1} \, \frac{n_1}{N} \\
&\textit{CONVERSION} && T_2 = T(n_1 - 1, n_2 + 1|\boldsymbol{n}) = k_2 \, \frac{n_1}{N} \\
&\textit{CONVERSION} && T_{-2} = T(n_1 + 1, n_2 - 1|\boldsymbol{n}) = k_{-2} \, \frac{n_2}{N} \\
&\textit{DETACHMENT} && T_3 = T(n_2 - 1|\boldsymbol{n}) = k_3 \, \frac{n_2}{N}
\end{aligned} \tag{3.3}$$

The governing master equation can be hence written in the following explicit expression:

$$\begin{aligned}\frac{\partial P(\boldsymbol{n},t)}{\partial t} = & T(\boldsymbol{n}|n_1-1)P(n_1-1,t) - T(n_1+1|\boldsymbol{n})P(\boldsymbol{n},t) + \\ & + T(\boldsymbol{n}|n_1+1)P(n_1+1,t) - T(n_1-1|\boldsymbol{n})P(\boldsymbol{n},t) + \\ & + T(\boldsymbol{n}|n_1+1,n_2-1)P(n_1+1,n_2-1,t) - T(n_1-1,n_2+1|\boldsymbol{n})P(\boldsymbol{n},t) + \\ & + T(\boldsymbol{n}|n_1-1,n_2+1)P(n_1-1,n_2+1,t) - T(n_1+1,n_2-1|\boldsymbol{n})P(\boldsymbol{n},t) + \\ & + T(\boldsymbol{n}|n_2+1)P(n_2+1,t) - T(n_2-1|\boldsymbol{n})P(\boldsymbol{n},t)\ .\end{aligned} \tag{3.4}$$

3.2 The deterministic limit

From the master equation one can readily derive the mean field equations that governs the deterministic dynamics for the fraction (in the following also referred to as the continuous concentrations) of the molecular motors in configurations A_1 and A_2. We define the averaged fraction of the molecular motors in states A_1 and A_2 in the continuous limit as:

$$\begin{aligned} y &= \frac{\langle n_1 \rangle}{N} = \frac{1}{N}\sum_{\boldsymbol{n}} n_1 P(\boldsymbol{n},t) \\ z &= \frac{\langle n_2 \rangle}{N} = \frac{1}{N}\sum_{\boldsymbol{n}} n_2 P(\boldsymbol{n},t) \end{aligned} \tag{3.5}$$

In the large system size limit, the master equation (3.4) yields the following set of first order ordinary differential equations for the self-consistent evolution of the mean field concentrations:

$$\begin{cases} \dfrac{dy}{dt} &= k_1 - \big(k_1 + k_{-1} + k_2\big)\ y - \big(k_1 - k_{-2}\big)\ z \\ \\ \dfrac{dz}{dt} &= k_2\ y - \big(k_{-2} + k_3\big)\ z \end{cases} \tag{3.6}$$

Equations (3.6) can be studied at equilibrium by computing the associated fixed points obtained imposing the conditions:

$$\frac{dy}{dt} = 0; \qquad \frac{dz}{dt} = 0;$$

A straightforward calculation returns the equilibrium concentrations:

$$\begin{cases} y^* = & \Big(\dfrac{k_1}{k_1+G}\Big)\dfrac{k_{-2}+k_3}{k_2+k_{-2}+k_3} \\ \\ z^* = & \Big(\dfrac{k_1}{k_1+G}\Big)\dfrac{k_2}{k_2+k_{-2}+k_3} \end{cases} \tag{3.7}$$

where:

$$G = \frac{k_{-1}(k_{-2}+k_3)+k_2 k_3}{k_2+k_{-2}+k_3}\ . \tag{3.8}$$

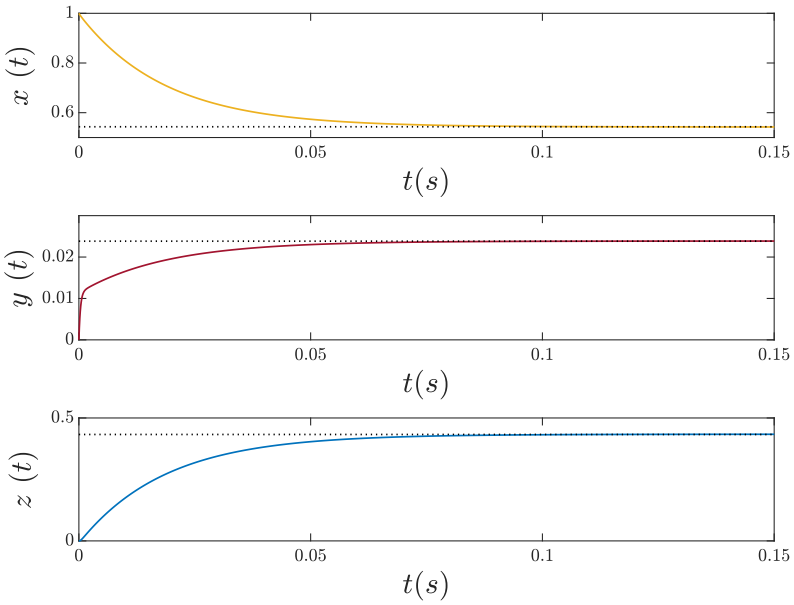

Figure 3.1: ***Temporal behaviour of the mean field concentrations of motors in different configurations.*** *The solid yellow line is the evolution of motors in the detached configuration D (yellow); the solid red and blue lines are the evolution of motors in the configuration A_1 and A_2 respectively. The dotted lines correspond to the values of the equilibrium fixed points for the concentrations x^*, y^*, z^* .*

We define the duty ratio r as the fraction of motors in an attached state (or the fraction of the ATPase cycle time a motor spends attached). In terms of the rate constants of the model, it can be computed as:

$$r = y^* + z^* = \frac{k_1}{k_1 + G} \ . \tag{3.9}$$

The temporal evolution of the mean field concentrations of the different populations of motors is described by the set of ordinary differential equations (3.6): these equations can be numerically integrated, for a representative choice of the kinetic rate constants, and the solutions are shown in Figure 3.1 for an ensemble of fixed size $N = 16$ molecular motors. In the specific case displayed in the Figure, the system evolves from an initial condition with all the motors detached from actin at $t = 0$; after a transient, the concentration of the motors in the various populations approach their equilibrium fixed points x^*, y^*, z^* as calculated in equations (3.7). The motors population dynamics in terms of the rate constants of the model is particularly complicated also due to the coupling between different configurations. In order to obtain a more manageable expression that will be useful in the analytical description of the force exerted by the ensemble of motors, a straightforward calculation can be performed to show that $z^* \simeq r = \frac{k_1}{k_1+G}$ and $y^* \ll 1$, when $k_{-2}/k_2, k_3/k_2 \ll 1$. In practical terms, under this operating assumption, which for the mammalian skeletal muscle myosin under consideration is approached at temperature $T \simeq 24\,^{\circ}\mathrm{C}$, motors are solely found in state A_2. Since this is the relevant setting for the

specific case study, in the next Section we will discuss a useful approximation for the motors population dynamics.

3.2.1 Effective model for the dynamics of the molecular motors in the high force-generating configuration

Let us assume that the population of motors in configuration A_1 is negligible as compared to those in state A_2. It is therefore legitimate to solely focus on the dynamics of species A_2, thus yielding a compact, though effective, descriptive model that we here introduce. We consider the original set of o.d.e. for the fractions of motors in the configurations A_1 and A_2 in the mean field framework (3.6). These equations can be drastically simplified by performing a self-consistent elimination of the variable y. To this end we set $dy/dt = 0$ in the first of equations (3.6) to eventually express y as a function of z. This procedure is customarily invoked to carry out the so called adiabatic elimination, which proves correct when there is a clear separation of time scales between co-evolving variables. Although this is not *a priori* the case for the system at hand, we will postulate the validity of the aforementioned condition and operate with the ensuing approximation that, as we shall prove at the end of this Section, will materialise in an accurate interpretative framework. Plugging the expression for y as a function of z into the second of equations (3.6), and solving the ensuing differential equation readily yields:

$$\begin{cases} \dfrac{dy}{dt} = 0 \qquad \longrightarrow \qquad y^* = \dfrac{k_1 + z\ (k_{-2} - k_1)}{k_1 + k_{-1} + k_2} \\ \\ \dfrac{dz}{dt} = \ k_2\ \dfrac{k_1 + z\ (k_{-2} - k_1)}{k_1 k + k_{-1} + k_2} - z\ (k_{-2} + k_3) = \\ \quad = \dfrac{k_1\ k_2}{k_1 + k_{-1} + k_2} - z\left[k_{-2} + k_3 - \dfrac{k_2\ (k_{-2} - k_1)}{k_1 + k_{-1} + k_2}\right] = b - az \end{cases} \tag{3.10}$$

which immediately yields solution:

$$\begin{aligned} z(t) &= \frac{b}{a}\Big(1 - e^{-at}\Big) = \\ &= \frac{k_1}{k_1 + G}\frac{k_2}{k_2 + k_{-2} + k_3}\left(1 - e^{-\left[k_{-2} + k_3 + \frac{k_2\ (k_1 - k_{-2})}{k_1 + k_{-1} + k_2}\right]t}\right) = \\ &= z^*\Big(1 - e^{-at}\Big) \end{aligned} \tag{3.11}$$

where a and b are positive quantities, self-consistently defined by the latter equality and G defined in (3.8).
This latter condition matches the homologous estimate for the equilibrium fraction of motors in A_2 derived from the original two dimensional model and reported in equations (3.7).
This approximation corresponds to a simplified reaction scheme:

$$\mathrm{D} \underset{\gamma}{\overset{\beta}{\rightleftharpoons}} \mathrm{A}_2$$

where β and γ represent the unknown rate constants that respectively quantifies the effective probability per unit time of attachment and detachment of a motor from actin. This scheme corresponds to the following mean field equation for the concentration of the population in configuration A_2:

$$\frac{d}{dt}\Big(\frac{n_2}{N}\Big) = \beta\Big(1 - \frac{n_2}{N}\Big) - \gamma\frac{n_2}{N}$$

By computing the stationary solution for the above model, i.e. by imposing the condition: $\frac{dn_2}{dt} = 0$, yields the equilibrium solution:

$$\frac{n_2}{N}^* = \frac{\beta}{\beta + \gamma}$$

that allows the identification: $\beta = b$ and $\gamma = a - b$ with a and b defined by equation (3.11). Through parameter a, we have also access to a closed estimate for the characteristic time scale of the exponential evolution of z, i.e. the rate of the force development. Let us notice that a is indeed the inverse of the time constant of the development of the steady force, τ as defined in the experiment, hence $a = 2.2/t_r$.
According to this simplified scheme, the effective rate of ATP consumption can be estimated as the flux ϕ of motors through the cycle per unit time. This equals to the rate of motors in A_2 detaching from the actin, in formula $\phi = z^*(a - b)$.
As anticipated, the validity of the adiabatic elimination was postulated even in the absence of a clear time scales separation of the dynamics of the system. Here we test the validity of this approach, for the investigated initial conditions in reproducing the correct time scale of the dynamics of the fraction of motors in A_2. In Figure 3.2 it is shown the evolution of the concentration of the motors in the force generating configuration A_2, with an initial condition with all the motors detached from the actin, from which it is possible to estimate the time scale upon which the stationary state is approached.
This solution will prove of interest, in the aim of devising a proper fitting scheme to be challenged against both synthetic and experimental data.

3.3 Solution of the stochastic dynamics at finite size

We now turn back to consider the stochastic dynamics of the system at finite size N, so as to account for the role played by finite size fluctuations. To quantify the contribution as stemming from the intimate graininess of the investigated system, we ought to solve the master equation (3.4) that implements the microscopic dynamics described by the chemical equations (3.1), and doing so to access the probability of finding the system in any of the allowed states at a generic time t. This is achieved as discussed in the following.
Firstly we remark that the solution of the master equation, i.e. the probability distribution $P(\boldsymbol{n}; t) \equiv P(n_1, n_2; t)$, can be written as a vector $\boldsymbol{P}(t)$ of dimension $(N+1)\times(N+1)$. This latter returns the probability at time t, of finding the system in the state characterised by n_1 motors in configuration A_1 and n_2 motors in configuration A_2. Here, n_1 and n_2 can in principle assume every integer values in the range $[0, N]$, i.e. a total of $N + 1$ values each. Observe however that the populations of motors in the configurations A_1 and A_2,

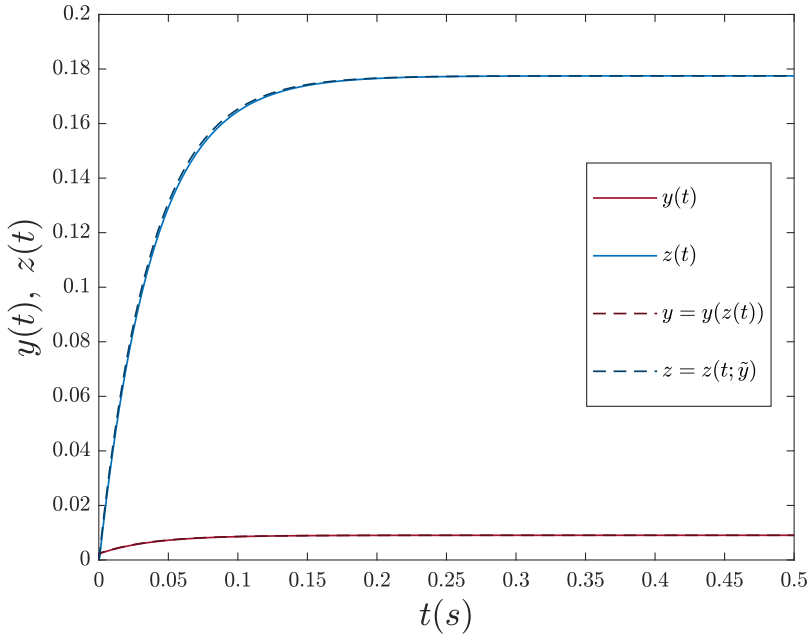

Figure 3.2: ***Validation of the adiabatic approximation.*** *In red (solid and dashed lines) the evolution of the concentration of motors in configuration A_1, in blue (solid and dashed lines) the evolution of the concentration of motors in configuration A_2. The solid lines represent the numerical integration of the dynamical system without any approximation, the dashed lines correspond to the integration of the dynamical system when the adiabatic approximation is adopted. The approximation allows to reproduce the correct the time scale at which the concentration of motors in A_2 reaches the stationary state.*

must satisfy the obvious constraint that reflects the conservation law, i.e. $n_1 + n_2 \leq N$. A simple way to express the condition above is to consider that for each possible value of n_1, n_2 can assume values in the range $[0, N - n_1]$. This readily implies that the total number of possible states of the system is identically equal to $M = (N + 1)(N + 2)/2$. The number of allowed states are hence smaller than what anticipated above. Indeed the non trivial entries of $\boldsymbol{P}(t)$ are $M = (N + 1)(N + 2)/2$. We will consequently focus on the non trivial elements of vector $\boldsymbol{P}(t)$ which we shall denote as $P_m(t)$ with $m = 1, \ldots, M$. For the relevant setting of $N = 16$ molecular motors, instead of $(N + 1) \times (N + 1) = 289$ configurations we only have $M = 153$ possible states that can be eventually visited by the system, and that we explicitly list in Table 3.1. The master equation (3.4) can be written in an equivalent matrix notation:

$$\frac{d\boldsymbol{P}(t)}{dt} = \tilde{\mathbb{Q}}\ \boldsymbol{P}(t) \qquad \text{in components:} \qquad \dot{P}_m(t) = \sum_{l=1}^{M} \tilde{Q}_{ml} P_l(t)$$

and, upon time discretisation:

$$\boldsymbol{P}(t + \Delta t) = \mathbb{Q}\ \boldsymbol{P}(t) \tag{3.13}$$

Table 3.1

$m \in [1, 153]$	$(n_1,\ n_2)$	
1	$(0,0)$	$q = 0$
2	$(0,1)$	
$\vdots$	$\vdots$	
17	$(0,16)$	
18	$(1,0)$	$q = 1$
$\vdots$	$\vdots$	
33	$(1,15)$	
34	$(2,0)$	
$\vdots$	$\vdots$	$\vdots$
150	$(14,2)$	
151	$(15,0)$	$q = 15$
152	$(15,1)$	
153	$(16,0)$	$q = 16$

(3.12)

where Δt is a microscopic timescale that we have selected for a uniform resampling of the stochastic dynamics. Matrix $\mathbb{Q}$ has dimension $M \times M$, it is stochastic and reads:

$$\mathbb{Q} = \mathbb{W}\Delta t + \left(\mathbb{1} - \sum_i W_{ij}\Delta t\ \delta_{ij}\right) . \tag{3.14}$$

The entries of the matrix $\mathbb{Q}$ can be computed from the transition rates of the underlying master equation. Let us focus on the generic element W_{lm} that enters the definition of matrix $\mathbb{Q}$. Assume in particular index m to label the reference initial state, while index l identifies the state that can be eventually reached through the chemical dynamics. Five possible types of transitions exist, organised in $q = N + 1$ blocks, which corresponds to the selected value of n_1, while n_2 can freely varies within $[0, N - n_1]$:

$$\begin{aligned}
l_1 &= m^{max}(q+1) + n_2 + 1 \\
l_2 &= m^{max}(q) - n_2^{max} + n_2 + 1 \\
l_3 &= m^{max}(q) - n_2^{max} + n_2 + 2 \\
l_4 &= m^{max}(q+1) + n_2 \\
l_5 &= m - 1
\end{aligned}$$

where we denote $m^{max}(q)$ the largest possible index as associated to block q, for the selected choice of m; while n_2^{max} stands the largest values that can eventually take the discrete variable n_2. Hence:

$$\begin{aligned}
n_2^{max} &= N - n_1 \\
m^{max}(q+1) &= m^{max}(q) + N + 1 - n_1
\end{aligned}$$

The non trivial elements $W_{m,l}$ are hence:

$$W_{l_1,m} \equiv T(n_1+1, n_2|n_1, n_2) = \frac{k_1}{N}\big(N - n_1 - n_2\big) \qquad \begin{cases} n_2 \in \big[0, n_2^{max} - 1\big] \\ n_1 \in \big[0, N-1\big] \end{cases}$$

$$W_{l_2,m} \equiv T(n_1-1, n_2|n_1, n_2) = \frac{k_{-1}}{N} n_1 \qquad \begin{cases} n_2 \in \big[0, n_2^{max}\big] \\ n_1 \in \big[1, N\big] \end{cases}$$

$$W_{l_3,m} \equiv T(n_1-1, n_2+1|n_1, n_2) = \frac{k_2}{N} n_1 \qquad \begin{cases} n_2 \in \big[0, n_2^{max}\big] \\ n_1 \in \big[1, N\big] \end{cases}$$

$$W_{l_4,m} \equiv T(n_1+1, n_2-1|n_1, n_2) = \frac{k_{-2}}{N} n_2 \qquad \begin{cases} n_2 \in \big[1, n_2^{max}\big] \\ n_1 \in \big[0, N-1\big] \end{cases}$$

$$W_{l_5,m} \equiv T(n_1, n_2-1|n_1, n_2) = \frac{k_3}{N} n_2 \qquad \begin{cases} n_2 \in \big[1, n_2^{max}\big] \\ n_1 \in \big[0, N\big] \end{cases}$$

Given the above structure, it is possible to identify for every choice of m, the corresponding combination of n_1 and n_2, and associate the $m-$component of vector $\boldsymbol{P}(t)$ to a specific state (n_1, n_2). That is possible because the $m^{max}(q)$ are in fact the partial sums of the finite sequence:

$$m^{max}(q) = \sum_{i=0}^{q} N + 1 - i \qquad\qquad i \in \{0, \dots, N\}$$

for $q = 0, \dots, N$.
For a given m, we thus identify the index q that matches the relation:

$$m^{max}(q) \geq m$$

and then set:

$$\begin{cases} n_1 = q \\ n_2 = m - m^{max}(q-1) - q \end{cases} \tag{3.15}$$

The stationary solution of the stochastic dynamics, i.e. the stationary probability distribution $\boldsymbol{P}^{\mathrm{ST}}$, defines the kernel of the $M \times M$ matrix $\mathbb{Q}$ and can be hence computed as the eigenvector of $\mathbb{Q}$ associate with the null eigenvalue.
It is also possible to compute the general solution of the master equation (3.13) at any step time t. This can be formally cast in the form:

$$\boldsymbol{P}(t) = \mathbb{Q}^t \boldsymbol{P}(0)$$

Denote the right eigenvector of $\mathbb{Q}$, associated to eigenvalue $\lambda^{(i)}$, as $\big|\psi^{(i)}\big\rangle$, and assume $\big\langle\chi^{(i)}\big|$ to label the corresponding left eigenvector. In formulae:

$$\begin{cases} \mathbb{Q}\big|\psi^{(i)}\big\rangle = \lambda^{(i)}\big|\psi^{(i)}\big\rangle \\ \\ \big\langle\chi^{(i)}\big|\,\mathbb{Q} = \lambda^{(i)}\big\langle\chi^{(i)}\big| \end{cases} \qquad\qquad i = 1, \dots M$$

The general solution at time t for the m-component can be expressed in a closed form as:

$$P_m(t) = \left(\mathbb{Q}\right)^t P_m(0) = \sum_{i=1}^{M} \left(\lambda^{(i)}\right)^t \left|\psi^{(i)}\right\rangle \left\langle\chi^{(i)}\right| P_m(0) \tag{3.16}$$

where $P_m(0)$ is the probability distribution at time $t = 0$.
From the knowledge of the exact solution, at any time t, and recalling the mapping (3.15), it is possible to extract the marginal probability distribution for motors in one of the two configuration A_1 or A_2. This is accomplished by formally defining the marginal probabilities $P(n_1; t)$ and $P(n_2; t)$:

$$\begin{aligned} P(n_1, t) &= \sum_{n_2} P(n_1, n_2, t) \\ P(n_2, t) &= \sum_{n_1} P(n_1, n_2, t) \end{aligned} \tag{3.17}$$

that allows us to calculate the average number of motors in one specific configuration as:

$$\begin{aligned} \langle n_1(t)\rangle &= \sum_{n_1=1}^{N} n_1 P(n_1, t) \\ \langle n_2(t)\rangle &= \sum_{n_2=1}^{N} n_2 P(n_2, t) \ . \end{aligned}$$

We are now presenting the details of the numerical simulations of the considered population dynamics, obtained via the celebrated Gillespie algorithm [67, 68]. This algorithm allows to numerically simulate a single stochastic orbit of the considered dynamics (working with the same rate constants as assumed in the the mean field simulations), generating a time series of the evolution of the macroscopic (discrete) fractions of motors, whose probability distribution are the solution of the master equation (3.13). A typical solution for the fractions of the various populations i.e. $n_D(t)/N$, $n_1(t)/N$, $n_2(t)/N$ for finite N is displayed in Figure 3.3. As expected the stochastic trajectories fluctuate around the corresponding deterministic orbit (solid lines). The observed fluctuations are a material imprint of the inherent discreteness of the simulated system.

The stationary probability distribution of fluctuations can be numerically accessed from individual stochastic simulations, by averaging over a large set of independent stochastic realisations. In Figure 3.4 the stationary state distribution of the fluctuations (i.e. the fluctuations displayed around the deterministic fixed point, once the initial transient has faded away) is depicted for the force-generating populations A_1 and A_2, and compared to the analytical solution obtained from the governing master equation, i.e. the marginal probability distributions $\boldsymbol{P}_1^{\mathrm{ST}}$ and $\boldsymbol{P}_2^{\mathrm{ST}}$, via the procedure discussed above. The agreement is satisfying and testifies on the correctness of the proposed analytical treatment.

Let us now recall the relevant setting for the examined system, for which it is reasonable to assume that the population of motors in configuration A_1 is negligible as compared to those in state A_2. It is therefore legitimate to solely focus on the dynamics of species A_2, thus yielding a compact, though effective, descriptive model. The marginal probability ρ_q to find $q \leq N$ motors in A_2 can be extracted from the stationary probability distribution

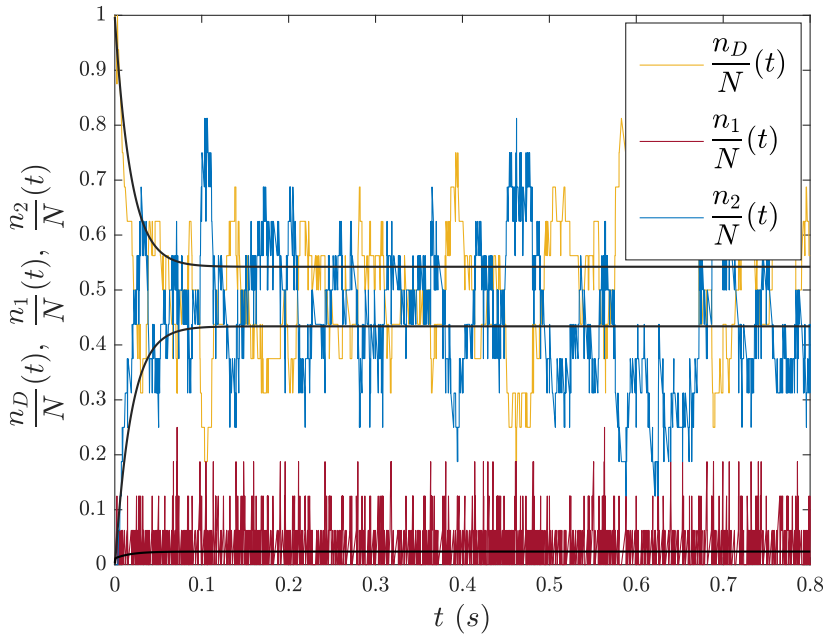

Figure 3.3: ***Stochastic simulations obtained with the Gillespie algorithm.*** *Temporal behaviour of the concentrations of the three populations of motors in each configuration: D (yellow line), $A1$ (red line), A_2 (blue line), for a small ensemble of size $N = 16$. The black solid lines represents the deterministic evolution of the concentrations.*

$\boldsymbol{P}^{\mathrm{ST}}$, the stationary solution of the master equation. This is done by summing the elements of $\boldsymbol{P}^{\mathrm{ST}}$ that refer to the selected q, and that account for all possible partitioning of the remaining $N - q$ motors among configurations D and A_1.
In the next section we will turn to discussing the isometric force as exerted by the pool of interacting molecular motors, arranged in different classes as dictated by the stochastic model here outlined.

3.4 From the population dynamics to the characterisation of the force

With the knowledge of the motors population dynamics we are now able to characterise the force exerted by a small ensemble of molecular motors in isometric conditions. This is obtained by combining the contributions from each individual motor of the collection: motors in the configuration A_1, each exerting a force f_1 and motors in A_2, each exerting a force f_2. The experimental set-up of the nanomachine is characterised by the fact that HMMs are deposited on the surface with a random orientation with respect to the actin filament. As a consequence, we assume that the intensity of the force exerted by a motor depends on the binding angle θ, as measured from the correct *in situ* orientation. Depending on the specific orientation of the molecule, the force progressively decreases up to a minimum value that can be set as $0.1 f_0$ [55]. In particular, the force of a single

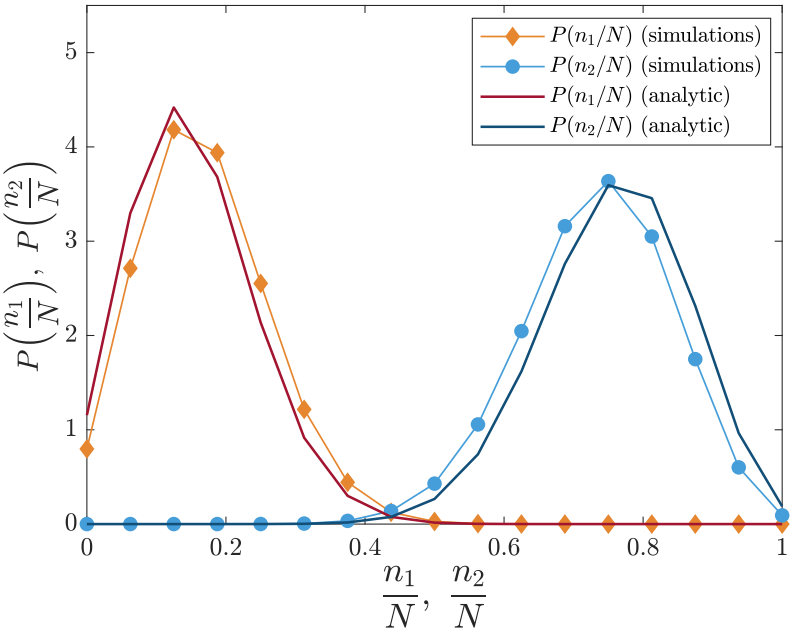

Figure 3.4: ***Checking the theory predictions*** **vs.** ***stochastic simulations.*** *Comparison between the stationary probability distributions of the fractions of motors in the force-generating configurations as obtained from the simulated dynamics and the stationary state solution of the master equation. Normalised histograms (light coloured lines with symbols) refers to the populations of motors in configurations A_1 (in red) and A_2 (in blue), as obtained from the simulated dynamics for a suitable choice of the kinetic parameters. Dark coloured lines stand for the homologous marginal distribution as derived from the stationary solution of the master equation.*

motor can change within a bounded interval: the largest value of the force f_0 is exerted when the motor orientation is correct (corresponding to the *in situ* orientation). Then, in accordance with [62] (see Supplementary Figure 2a) we postulate that the exerted force f_1 is a random variable, uniformly distributed within the interval $\mathcal{I}_1 = \left[-f_0, f_0\right]$. Similarly, the force f_2 is randomly extracted from the interval $\mathcal{I}_2 = \left[\frac{f_0}{10}, f_0\right]$.

3.4.1 Mean field analysis

Let us focus initially on the average force exerted by the small ensemble of motors. The mean field average force exerted by the ensemble of myosin motors, at any time t can be written as:

$$\langle F(t)\rangle = \langle n_1(t)\rangle \langle f_1\rangle + \langle n_2(t)\rangle \langle f_2\rangle = \langle n_2(t)\rangle \langle f_2\rangle \tag{3.18}$$

given that $\langle f_1\rangle = 0$ since the interval $\mathcal{I}_1$ is symmetric with respect to zero. In the stationary state, $\langle F(t)\rangle$ converges to the asymptotic plateau value F_0, and thus:

$$F_0 = N z^* \frac{11}{20} f_0$$

where use has been made of the self-consistent condition $\langle f_2 \rangle = (11/20) f_0$. If we recall that $z^* \simeq r$, for the case here examined we are left with the final expression:

$$r f_0 = \frac{1}{N} \frac{20}{11} F_0 \ . \tag{3.19}$$

We observe that the experimental value of the stationary force exerted by a pool of N motors acting in the state A_2, solely constrains the product of f_0 and r. That is, on deterministic means, we cannot access a direct estimate of the maximum force exerted by an individual motor f_0, and the associated duty ratio of the ensemble r, but just constraint this latter pair to fall on a hyperbole, set by F_0. Accounting for the fluctuations superimposed on F_0, and thus by properly gauging the stochastic component of the dynamics, enables us to resolve the above degeneracy.

3.4.2 On the role of fluctuations

To take full profit from the available experimental information and to improve on the deterministic handling of the recorded data, we consider the dynamics of the system at finite N, so as to account for the role played by finite size fluctuations. To quantify the contribution as stemming from the intimate graininess of the investigated system, we ought to solve the master equation (3.13), focusing in particular on the stationary state probability distribution $\boldsymbol{P}^{\mathrm{ST}}$. As discussed in the previous Section, we are in a position to solve exactly the stochastic model in its stationary state, and thus get a closed expression for $\boldsymbol{P}^{\mathrm{ST}}$, as function of the parameters of the model. This knowledge will be used to compute $P(F)$, the probability distribution of the total force F, exerted by the ensemble in isometric conditions. Remark that $P(F)$ is ultimately shaped by the kinetic constants of the model (namely, $k_1, k_{-1}, k_2, k_{-2}, k_3$) and also reflects the maximum force f_0, as applied by individual motors. Recall also that N is directly determined by the protocol of counting of the rupture events in ATP-free solution detailed in Chapter 2 (see Figure 2.3).
In the next Chapter we will construct an inverse procedure to recover information on the underlying parameters, by confronting the predicted distribution of the force $P(F)$ to the homologous curve obtained from the experimentally recorded data. In particular we will prove that, by exploiting the information content as stemming from the fluctuations, it is eventually possible to unambiguously determine both f_0 and r.

The knowledge of the stationary marginal probabilities $(\rho_0, \rho_1, \rho_2, ..., \rho_N)$ calculated at the end of the previous Section opens up the perspective to calculate the non-equilibrium stationary state distribution of the force F exerted by the ensemble of motors.
To work along these lines we shall assume that the contribution to the force (including fluctuations) of the motors in the state A_1 is always negligible. This assumption is motivated by the fact that, for the experimental setting here explored, only a tiny fraction of motors is found to populate state A_1, at any time t. In the next Section we will relax this working assumption so as to provide a rigorous theoretical framework that extends to account for the relevant setting where the population of A_1 motors is instead significant in size.
Let us focus on $q \leq N$ distinct motors in state A_2. As postulated earlier, each motor can exert a constant random force f, uniformly spanning the assigned interval $\mathcal{I}_2$. For each

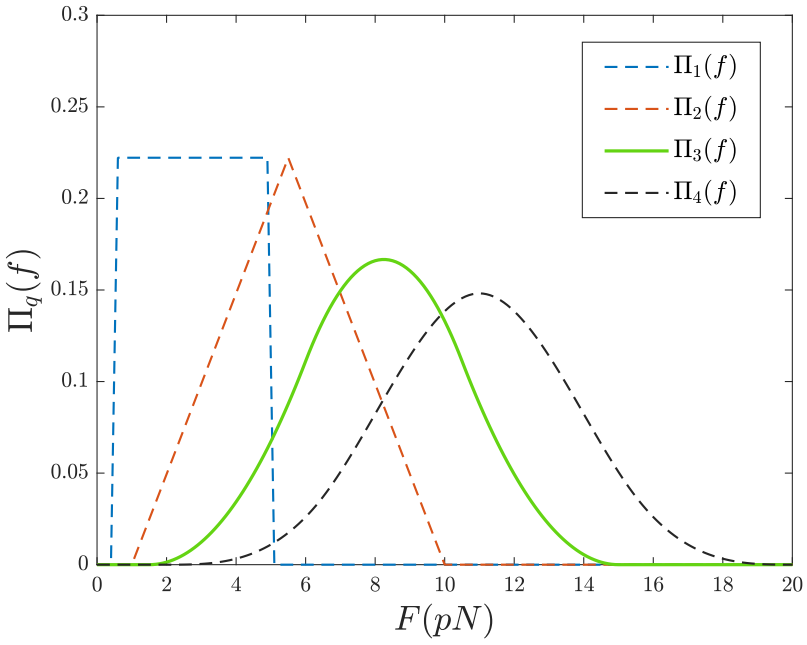

Figure 3.5: ***Many body stationary force probability distributions.*** *The probability distributions* $\Pi_q(f)$ *are plotted for* $q = 1, 2, 3, 4$.

choice of q, we can compute the distribution of the forces $\Pi_q(f)$ applied by the selected q motors, by combining independent and identically uniformly distributed random variables drawn for the interval of pertinence $\mathcal{I}_2$. Functions $\Pi_q(f)$ need to be combined together with proper weighting factors that reflect the stationary probability ρ_q of having exactly q motors in the force-generating state A_2, namely:

$$P(F) = \rho_1\Pi_1(f) + \rho_2\Pi_2(f) + \cdots + \rho_{16}\Pi_{16}(f) \ = \sum_{q=1}^{N} \rho_q \ \Pi_q(f) \ .$$

where use has been made of the fact that $\Pi_0 = 0$.
The obtained profiles are reported in Figure 3.5 for the relevant case $N = 16$ and for $q = 1, 2, 3, 4$. In Figure 3.6 the global distribution of fluctuations is depicted for a specific choice of the parameter f_0 and the rate constants of the model. The general analytical characterization of the probability distribution of the force of an ensemble of motors in two different force-generating configurations is provided in the following.

3.4.3 Analytical characterisation of the force probability distribution

As mentioned, the fluctuations of the force around the average value stem from finite size corrections. To estimate the probability distribution $P(F)$ we focus on $q \in [1, N]$ force-generating distinct motors and postulate that each of them can exert a uniform, randomly selected force f. For each choice of q, one can compute the distribution of the force $\Pi_q(f)$ exerted by the q motors. This is a particular case of the more general problem of calculating the probability distribution for the total force exerted by all the

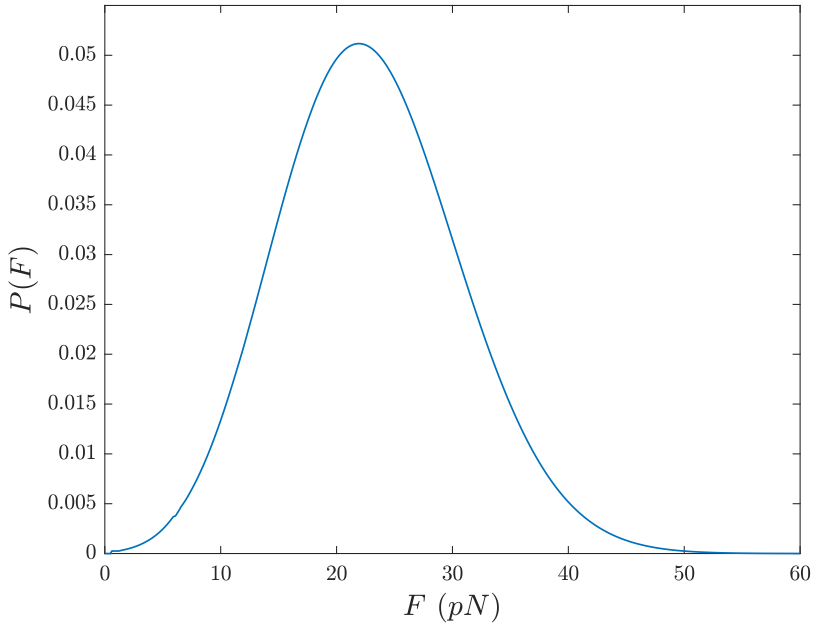

Figure 3.6: ***Theoretical distribution of force fluctuations.*** *Probability density function $P(F)$ as resulting from the sum of the $\Pi_q(f)$, for $q = 1, \ldots, N$ weighted with the stationary solution of the master equation for a system of $N = 16$. The adopted parameters are: $f_0 = 6\ pN$, $k_1 = 30\ s^{-1}$, $k_{-1} = 500\ s^{-1}$ $k_2 = 2000\ s^{-1}$ $k_{-2} = 100\ s^{-1}$ $k_3 = 10\ s^{-1}$.*

n_1 and n_2 molecular motors in the force-generating configurations A_1 and A_2. Here we discuss the problem under this general perspective. To this end we denote by f_1 the random force uniformly distributed in the interval $\mathcal{I}_1$ and exerted by the motors in configuration A_1 and by f_2 the one extracted from the interval $\mathcal{I}_2$, exerted by the motors in the configuration A_2.
As suggested in [69] we are dealing with the problem of finding the probability distribution of the sum of n random variables Y_i, for $i = 1, \ldots, n$ each of them uniformly distributed in the interval $[b_i, c_i]$. In our case we have only two classes of variables Y_i: the ones relative to the forces exerted by motors in the configuration A_1, and those relative to the forces exerted by motors in the configuration A_2, so that:

$$\sum_{i=1}^{n} Y_i = \sum_{i=1}^{n_1} Y_i + \sum_{i=n_1+1}^{n} Y_i$$

and:

$$Y_i = \begin{cases} f_1 \quad \text{and} \quad [b_i, c_i] = [-f_0, f_0] \quad \text{if} \quad i = 1, \ldots, n_1 \\ \\ f_2 \quad \text{and} \quad [b_i, c_i] = \left[\dfrac{f_0}{10}, f_0\right] \quad \text{if} \quad i = n_1 + 1, \ldots, n \end{cases} \tag{3.20}$$

We can observe that the probability distributions of the sum of the variables Y_i is the same as the probability distribution of the sum of the variables $X_i = Y_i - b_i$, which are

defined in the intervals $[0, a_i]$, where $a_i = c_i - b_i$.
Introduce the sum s:

$$s = \sum_{i=1}^{n} X_i$$

with $n \geq 2$. Then the distribution of the sum as defined above reads [69]:

$$\Pi_n(s; n_1, n_2) = \frac{1}{(n-1)!} \frac{1}{(a_1)^{n_1}(a_2)^{n_2}} \left[s^{n-1} + \sum_{k=1}^{n} (-1)^k \left(\sum_{J_k} \Big(s - \sum_{l=1}^{k} a_{j_l} \Big)_+ \right)^{n-1} \right] \tag{3.21}$$

where we adopted the notation: $(f)_+ = max\{0, f\}$.
From this expression it is possible to compute the probability distribution for the sum of the variables of our interest:

$$\sum_{i=1}^{n} Y_i = \sum_{i=1}^{n} \Big(X_i + b_i \Big) = \sum_{i=1}^{n} X_i + \sum_{i=1}^{n_1} b_i + \sum_{i=n_1+1}^{n} b_i = s + n_1 b_1 + n_2 b_2$$

where $b_1 = -f_0$ and $b_2 = \frac{f_0}{10}$.
If we consider just one class of variables Y_i, meaning if we consider only the forces exerted by one of the two force-generating populations of motors, the distributions Π_n can be computed as a specific case of the generalisation of the Irwin-Hall distribution, [70], the uniform sum distribution. These refer to the sum of n random variables x_i, each of them defined in the interval $[a, b]$ and take the form:

$$\Pi_n(x) = \frac{1}{b-a}\, g(y; n) \qquad \text{with:} \qquad y = \frac{x - na}{(b-a)} \tag{3.22}$$

where:

$$g(y, n) = \frac{1}{2(n-1)!} \sum_{k=0}^{n} (-1)^k \binom{n}{k} (y-k)^{n-1} \operatorname{sgn}(y-k)\ .$$

When considering only one population of motors in one of the two force-exerting configurations, n_j where j can be $j = 1$ or $j = 2$, the probability distribution associated with such an ensemble is $P(F_j)$ with $F_j = n_j f_j$ and it is given by the expression (3.22) where $n = n_j$ and $x = f_j$. The general case of an ensemble constituted by two different populations of force-generating motors requires the use of the expression (3.21) with $n = n_1 + n_2$ and $s = F_1 + F_2 = n_1 f_1 + n_2 f_2$.

3.4.4 Simulating the stochastic force generated by a small ensemble of motors

We are now in the position to simulate also the temporal series of the force of the ensemble. This is obtained by assigning to each individual motor the force that it is able to exert, based on its configuration (as stipulated by the stochastic dynamics), and following the prescriptions described in the previous Section. In Figure 3.7 (a) is displayed the time series of the force exerted by motors of populations A_1 and A_2, when we impose an initial condition with all the motors detached from the actin, for a specific choice of the parameters. The empirical probability distribution of the force of the ensemble at the

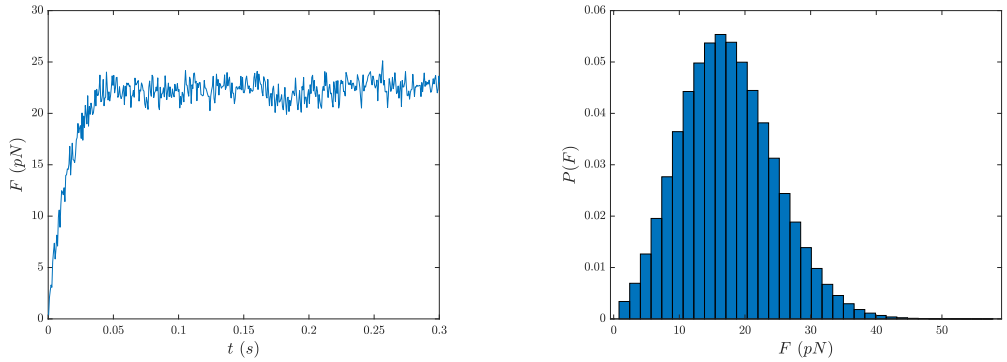

(a) *(b)*

Figure 3.7: **a.** *Force development as obtained by averages of stochastic simulations. The trajectory has been obtained averaging over* 100 *independent simulated trajectories. The force is measured in pN and it is exerted by a collection of* $N = 16$ *molecular motors with a suitable choice of the kinetic parameters.* **b.** *Probability distribution of the force of the ensemble. The histogram has been obtained from a single time series of the force of the ensemble at the isometric plateau, obtained via the Gillespie algorithm. The force is measured in pN and it is exerted by a collection of* $N = 16$ *molecular motors with a suitable choice of the kinetic parameters.*

isometric plateau, for a specific set of parameters, can be obtained from a time series of $F(t)$; the resulting histogram of the force fluctuations is shown in Figure 3.7 (b).

By accessing the temporal evolution of the force, including the fluctuations around the equilibrium value, we can recover key information on the underlying structural and kinetic parameters. This task corresponds to solve an inverse problem, from the observed time series of the force of the ensemble back to the relevant parameters. The details of this reverse engineering procedure for parameter estimation it is presented in details in the next Chapter.

3.5 The fitting strategy for parameters estimation

In this Section we present the strategy adopted to estimate the relevant parameters of the model. We will construct an inverse procedure to recover information on the underlying parameters, by confronting the predicted distribution of the force $P(F)$ to the homologous curve recorded experimentally. In particular we will prove that, by exploiting the information content as stemming from the fluctuations, it is eventually possible to unambiguously determine both f_0 and r.

In the following we validate in detail the procedure against synthetically generated data based on the stochastic model introduced in the previous sections.

3.5.1 Inverse scheme validation on synthetic data

By accessing the temporal evolution of the force, including the equilibrium fluctuations, one can aim at recovering some information on the underlying structural and chemical

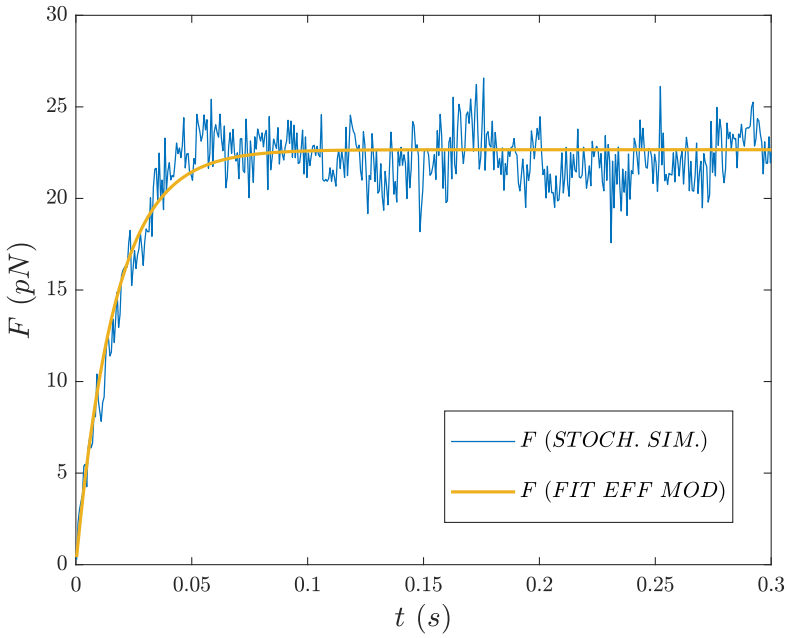

Figure 3.8: ***Fitting procedure of the synthetic data obtained for the force development.*** *The force development of the synthetic data obtained with the stochastic simulations (blue noisy trajectory, measured in pN, exerted by a collection of $N = 16$ molecular motors, with parameters $T_0 = 22.9\ pN$ and $a = 54.7\ s^{-1}$) has been fitted with the solution of the mean field effective model (yellow line).*

parameters. This corresponds to solving an inverse problem, from the observed force back to the relevant parameters, that we shall formalize hereafter. We begin by focusing on the average force profile, hence disregard the impact of finite size fluctuations. As mentioned in Section 3.2.1, the time evolution of the recorded force can be approximated by an effective, two-parameters model. These parameters - respectively denoted F_0, the mean value of the force exerted by the ensemble once the isometric plateau has been reached, and a, the rate of the force development - can be estimated via a direct fit, as shown in Figure 3.8 Having accessed to preliminary estimated values for the average force at the stationary plateau F_0 and for the rate of isometric force development a, one can then set forth to characterise the other kinetic parameters by analysing the distribution of the fluctuations of the force around the asymptotic plateau. To this end we note that f_0, following equation (3.19) in the framework of the effective model, can be written as:

$$f_0 = \frac{20}{11}\frac{F_0}{N}\frac{a}{b} \tag{3.23}$$

where a is constrained to the value determined by the parameters estimation performed on the force development trajectory, while $b = k_1 k_2/(k_1 + k_{-1} + k_2)$ as defined by equation (3.11).

Armed with the above knowledge, we can proceed further by comparing the probability density function of the force fluctuations $P(F)$ as obtained analytically, to the homologous histogram computed from the stochastic simulations (the empirical distribution of the force $\bar{P}(F)$). The former is adjusted to the latter by modulating the free parameters k_1,

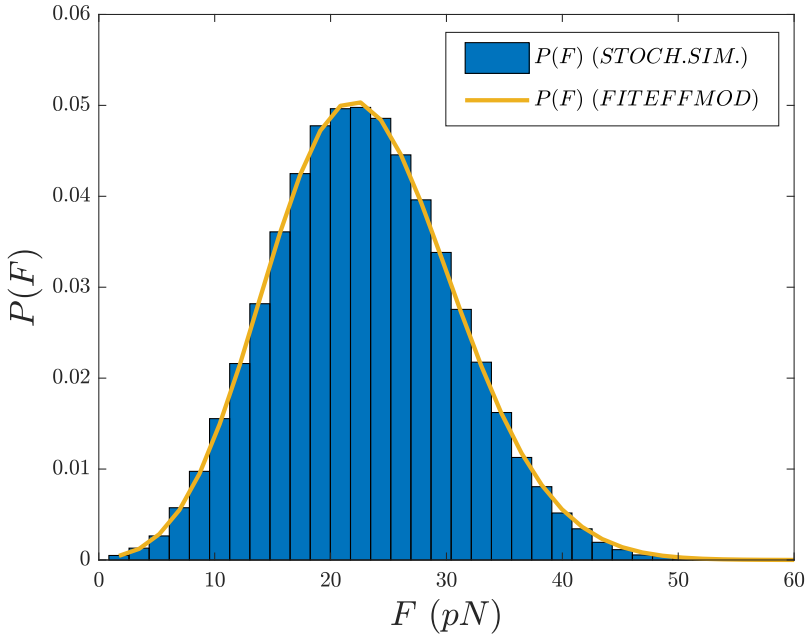

Figure 3.9: ***Fitting procedure of the synthetic data obtained for the force fluctuations at the isometric plateau.*** *The probability density function of the force as obtained from the stochastic simulations (blue bars) is compared to the fitted profile (yellow line).*

k_{-1}, k_2, k_{-2} and k_3, for a fixed choice of N (here set to the correct value, namely the value assumed in the simulations, $N = 16$). The fit is based on a simulated annealing algorithm to optimise the loss function:

$$\mathcal{L} = |\bar{P}(F) - P(F)|^2 \tag{3.24}$$

where $|\cdot|$ represents the usual L_2 norm. The results of the fitting via inverse scheme is shown in Figure 3.9. Testing the method against synthetic data generated *in silico* enables us to conclude that, the force of a correctly oriented motor and the duty ratio of the ensemble, i.e. parameters f_0 and $r = k_1/(k_1 + G)$, can be correctly estimated, as it follows from inspection of Table 3.2. Also the estimated b and a (recomputed

Table 3.2: ***Estimated parameters via the inverse scheme fed with simulated data.***
Errors are below 10^{-3} *if not explicitly provided.*

	F_0 (pN)	f_0 (pN)	r	a (s^{-1})	b (s^{-1})	ϕ(s^{-1})
True parameters	22.9	6.0	0.46	54.7	23.7	13.43
Estimated parameters	22.7	6.1	0.46 ± 0.03	54.8	23.5	13.42

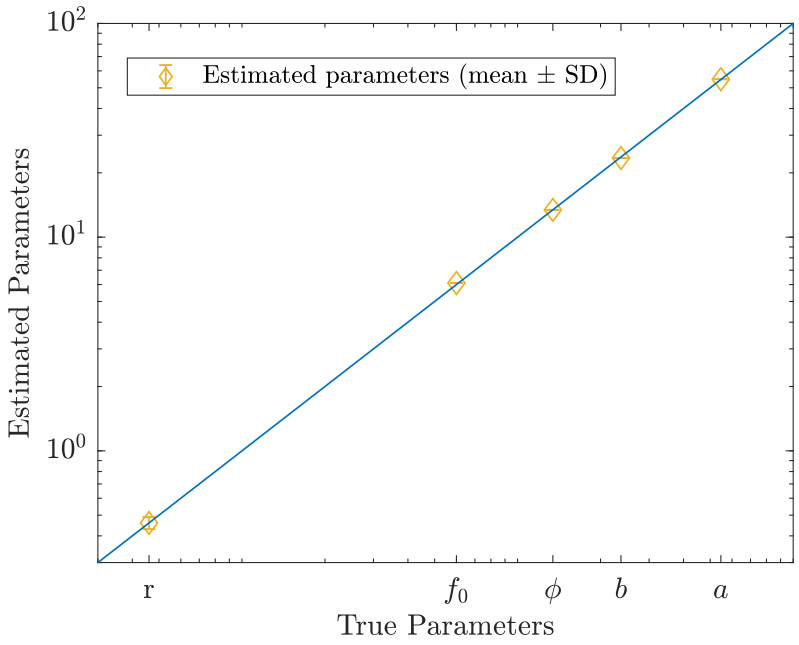

Figure 3.10: ***Results of the optimisation procedure for the parameters estimation.*** *The parameters estimation has been performed in the framework of the effective model and the results are identified by the yellow symbols (Mean values and standard deviations are obtained from different replica of the stochastic optimization algorithm). The estimated values are compared with the parameters adopted in the stochastic simulations of the dynamics (blue solid line).*

from the best fitted values for the kinetic constants) are pretty close to their nominal values as imposed in the simulations. Remarkably ϕ, the rate of motors completing the interacting cycle with the actin, is also correctly recovered. Figure 3.10 shows the graphic comparison between the results of the optimisation procedure for the parameters estimation performed under the assumptions of the effective model, and the values of the parameters adopted in the stochastic simulations of the dynamics (these latter are referred to as true parameters, as they are imposed in the simulation and thus known with infinite precision). The symbols refers to the mean and SD of the duty ratio r, the force of a single motor f_0, the rate ϕ and the two parameters a and b that describe the dynamics of the system in the deterministic limit. The blue line represents the value of the corresponding parameter adopted in the simulations. In Figure 3.11 it is shown the parameters estimation in the plane (f_0, r), where the solutions resulting from the analysis of the force of the ensemble in the deterministic framework are represented by the solid line, while the symbols shows the value of the parameter f_0 and r that can be estimated by taking into account the fluctuations of the force of the ensemble.
The above analysis refers to a fixed value of N, the size of the system that we assumed (from the experiment results shown in Figure 2.3) to be $N = 16$. In principle the correct value of N is not *a priori* known. To overcome this intrinsic limitation, one could repeat the analysis by varying N and recording the parameters estimated as follows the fitting scheme. Here, we will consider the simplified setting where a and b are frozen to the values determined for $N = 16$ (so that z^* remains unchanged). This is implemented by

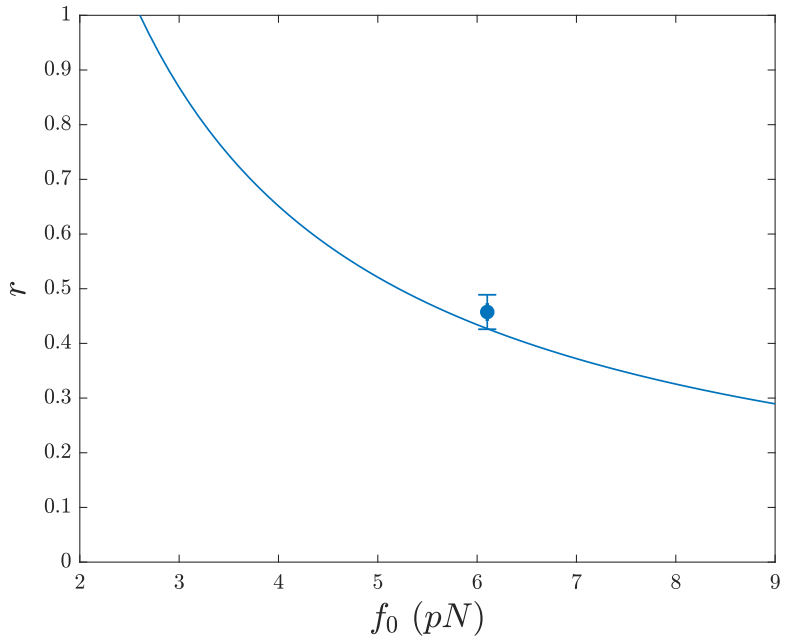

Figure 3.11: ***Parameters estimates in the reference plane*** (f_0, r). *The symbol follows from the integrated fitting strategy that accounts for fluctuations. The solid line is the hyperbole populated with the degenerate mean field, hence deterministic solutions. Remark that the fitted symbol is close but not on top of the hyperbole. The observed deviation is eventually due to the residual population* y^* *that is adequately estimated via the generalised fitting strategy base on the stochastic description. The error is obtained from different replica of the stochastic optimisation algorithm.*

removing two parameters from the pool of quantities to be fitted. Specifically k_{-1} and k_3 are constrained to match two constitutive relations, that involve k_1, k_2 and k_{-2}, in addition to a and b. The parameters to be fitted are hence k_1, k_2 and k_{-2}, while k_{-1}, k_3 and f_0 can be self-consistently determined from the their best fit values. Notice that f_0 is expected to change as a function of N as specified by relation (3.23). The result of the analysis are reported in Figure 3.12: the fitting procedure converges (with the requested limit of precision) only over a finite range of values of N, centred around the value adopted when performing the simulations. This observation implies that we are in a position to obtain a reasonable estimate for the interval of pertinence of N, as follows the procedure outlined above.
The introduced theoretical framework and the ensuing fitting strategy, thoroughly validated against synthetic data, can be hence applied to the analysis of the experimental data so to yield a self-consistent estimate of the underlying mechanokinetic parameters.

In this Chapter we have presented a combined experimental and theoretical approach that could set the basis for future studies on the emergent mechanokinetic properties of the half-sarcomere-like arrangement of any myosin motors, either engineered or purified from mutant animal models or human biopsies. In Section 3.5 we showed that the inverse scheme adopted to estimate the underlying parameters of the dynamics is able to

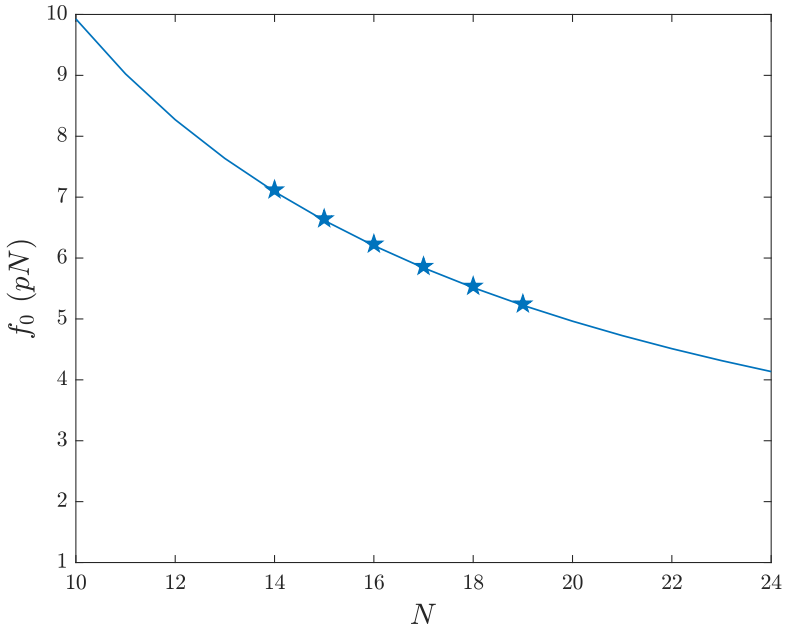

Figure 3.12: ***Checking f_0 against N.*** *The parameter f_0 is estimated as a function of N (solid line) applying the inverse scheme to the simulated data. The symbols refers to the best fit value of f_0 as determined for different choices of N.*

provide an accurate estimate for the force of a single molecular motor with the correct orientation, and the duty ratio of the ensemble of motors. This achievement has been made possible by combining the exact solution of the master equation to express the marginal probability distribution for the populations of force generating motors A_2 and the Irwing-Hall probability distributions for the uniform sums distributions to describe the probability distribution of the force of the ensemble. However the definition of the underlying kinetic rate constants of the dynamics remains uncertain due to the multiple possible combinations of these microscopic parameters that results in the same macroscopic ensemble behaviour. The analysis presented has been carried out under the assumption that the contribution of the motors in state A_1, to the force exerted by the ensemble, is negligible. The assumption has been motivated by the fact that, for the experimental setting explored in Chapter 2, only a tiny fraction of motors is found to populate state A_1, at any time t, given the fact that all experiments were conducted at room temperature. In order to generalised the proposed theoretical conceptualisation of the model, in the next Chapter 4 we will present and discuss a more general formulation of the analytical problem of the description of the probability distribution of the force exerted by an ensemble of motors that can be found in two different force-generating configurations, by explicitly taking into account the contribution of motors in population A_1, that becomes relevant for experimental data acquired at lower temperatures. This new approach will employ two different strategies. On the one hand the distribution of the force of the ensemble will be treated as random sum distributions instead of Irwing-Hall distributions: this will prove useful given that random sum distributions converge to normal distributions in the context of pertinence. On the other hand the master equation can be treated in the Gaussian noise approximation, also known as the

Van Kampen approximation, that provides an useful expression when the concentrations of the motors populations are sufficiently different from zero. These two approximations will prove essential in order to obtain more manageable expressions to be implemented in a revised version of the fitting scheme for parameters estimation.

Chapter 4

Model generalisation

In the previous Chapter we developed a fitting procedure to analyse data recorded in experiments conducted at room temperature on HMMs purified from two different mammalian skeletal muscles. The results of the application of this approach to the experimental data will be provided and discussed extensively in Chapter 5. Under such experimental conditions it is reasonable to assume that the contribution of motors in configuration A_1 to the force of the ensemble is negligible.
The contributions of motors in low force configuration become relevant when the array of motors performs at lower temperatures (around $T \simeq 12\,^{\circ}\mathrm{C}$).
In this Chapter we present a generalisation of the theoretical approach, that allows us to take into account the force contributions of molecular motors in configuration A_1. The fitting strategy can be hence generalised to account for data sets recorded at different temperatures. The structure of the Chapter is the following: in Section 4.1 we present the approximation of the analytical form of the probability distribution $P(F)$ of the force exerted by an ensemble made of two different force-generating motor states; in Section 4.2 we implement the procedure to account for the temperature dependency of the kinetic rates, while in Section 4.3 we propose an alternative approach for the solution of the population dynamics, that involves the Gaussian noise approximation. The advantage of this last approach consists in the fact that it allows to obtain an explicit expression for the probability distribution of the motors populations, which does not require to solve the master equation, therefore yielding a more straightforward (and less time consuming, from the computational point of view) fitting procedure.
The aim for this general formalisation would be to estimate not only the force of a single correctly oriented molecular motor f_0 and the duty ratio r of the ensemble, but also to improve on the estimate for the order of magnitude of the kinetic rates that govern the dynamics of the system. The kinetic parameters were in fact not properly resolved with the previous fitting scheme, due to the multiple microscopic combinations of rate constants that result in the same macroscopic behaviour of the ensemble, and thus in the same estimation for parameters like the single motor force or duty ratio. Combining synthetic data that reproduce the evolution of the force of the ensemble of motors at different temperatures provides a way to constrain the microscopic evolution to reveal the underlying kinetic parameters of the dynamics.

4.1 Force exerted by an ensemble of myosin motors in two force-generating configurations

The analysis develops from the deterministic description of the interactions between the force-generating populations of motors in the ensemble, and then moves to the stochastic description in order to account for the fluctuations of the total force. The aim is to provide a theoretical description of the probability distributions of the force fluctuations around the isometric plateau that will be employed in the parameter estimations presented at the end of the Section.

4.1.1 The mean field evolution

We recall the expression of the set of differential equations for the evolution of the fractions of attached motors $y(t)$ and $z(t)$, already defined in Section 3.2 of Chapter 3:

$$\begin{cases} \dfrac{dy}{dt} &= k_1 - \big(k_1 + k_{-1} + k_2\big)\ y - \big(k_1 - k_{-2}\big)\ z \\ \\ \dfrac{dz}{dt} &= k_2\ y - \big(k_{-2} + k_3\big)\ z \end{cases} \tag{4.1}$$

The system can be written as: $\dot{\boldsymbol{x}} = J\boldsymbol{x} + \boldsymbol{b}$ where $\boldsymbol{x} = (y, z)$, $\boldsymbol{b}^T = (k_1, 0)$ and J is the jacobian matrix of the linear system (that does not depend on the concentrations):

$$J = \begin{pmatrix} -(k_1 + k_{-1} + k_2) & -k_1 + k_{-2} \\ k_2 & -(k_{-2} + k_3) \end{pmatrix} \tag{4.2}$$

We denote with $\theta_{1,2}$ the eigenvalues of the matrix. The corresponding eigenvectors are $\boldsymbol{v}_{1,2}$. The solution of the system is:

$$\begin{cases} y(t) &= y^* + c_1 e^{\theta_1 t} v_{11} + c_2 e^{\theta_2 t} v_{21} \\ \\ z(t) &= z^* + c_1 e^{\theta_1 t} v_{12} + c_2 e^{\theta_2 t} v_{22} \end{cases} \tag{4.3}$$

where:

$$\begin{cases} y^* = & \Big(\dfrac{k_1}{k_1 + G}\Big) \dfrac{k_{-2} + k_3}{k_2 + k_{-2} + k_3} \\ \\ z^* = & \Big(\dfrac{k_1}{k_1 + G}\Big) \dfrac{k_2}{k_2 + k_{-2} + k_3} \end{cases} \tag{4.4}$$

are the equilibrium fixed points of the system and we the expression of G, defined in Chapter 3, is recalled here for the sake of simplicity: $G = (k_{-1}(k_{-2} + k_3) + k_2 k_3)/(k_2 + k_{-2} + k_3)$.
The constants $c_{1,2}$ can be computed by imposing the initial conditions of interest. In the following we will assume $\boldsymbol{x}(t = 0) = (0, 0)$, that readily yields:

$$\begin{cases} c_1 &= \dfrac{1}{det(V)} \Big(-y^* v_{2,2} + z^* v_{2,1}\Big) \\ \\ c_2 &= \dfrac{1}{det(V)} \Big(y^* v_{1,2} + z^* v_{1,1}\Big) \end{cases} \tag{4.5}$$

where we have defined the matrix:

$$V = \begin{pmatrix} v_{1,1} & v_{2,1} \\ v_{1,2} & v_{2,2} \end{pmatrix} .$$

Focusing on the equilibrium solution of the mean field dynamics we can quantify the so called duty ratio r, i.e. the average fraction of attached motors, that results in the same expression founded in Chapter 3, Section 3.2: $r = y^* + z^* = \frac{k_1}{k_1+G}$ with G defined above. Let us consider now the force exerted by the ensemble of N motors. As already recalled in Chapter 3, the myosin fragments available for interaction with the actin are deposited on a support with random orientation, and this reflects in the force exerted by each individual motor. In particular we have assumed that the force applied by motors in configuration A_1 is uniformly distributed in the interval $\mathcal{I}_1 = [-f_0, f_0]$, while the force exerted by motors in A_2 is uniformly distributed in the interval $\mathcal{I}_2 = [f_0/10, f_0]$. Hence, the average force exerted by motors in configuration A_1 is zero ($\langle f_1 \rangle = 0$). We can thus conclude that the average force F_0, exerted by the collection of examined motors at the isometric plateau, is:

$$F_0 = \langle n_1 \rangle \langle f_1 \rangle + \langle f_2 \rangle \langle f_2 \rangle = N\Big(\langle f_1 \rangle y^* + \langle f_2 \rangle z^*\Big) = N \langle f_2 \rangle z^* . \tag{4.6}$$

4.1.2 Stationary solution of the master equation

Let us focus on the stochastic evolution of the populations of motors. The dynamics of the system under scrutiny is governed by a master equation that quantifies the probability associated to each possible state of the system. The master equation can be cast in the general form (3.2), where $T(\boldsymbol{n}|\boldsymbol{n'})$ stand for the transition rates which follow the kinetic scheme (3.1).
In order to obtain the theoretical expression for the probability distribution of the force exerted by an ensemble composed of n_1 motors in configuration A_1 and n_2 motors in configuration A_2, as a function of the system's parameters, we perform the following steps:

1. We solve the master equation in the stationary state to obtain $P(n_1 = q_1, n_2 = q_2)$

2. We define the total force produced by the active motors at any time t. This latter depends on the number of motors in each force-generating configurations, namely:

$$F_{n_1,n_2}(t) = \sum_{i=0}^{n_1(t)} f_1^i + \sum_{i=0}^{n_2(t)} f_2^i \tag{4.7}$$

   where f_1^i and f_2^i are, for all $i \in \{0, \ldots, n_j\}$ for $j = \{1, 2\}$, random variables with uniform probability distributions $U(-f_0, f_0)$, and $U(f_0/10, f_0)$ respectively.

3. We fix q_1 and q_2 in $\{0, \dots, N\}$ and define the total force exerted by an ensemble made of q_1 motors in state A_1 and q_2 motors in state A_2:

$$F_{q_1,q_2} = \sum_{i=0}^{q_1} f_1^i + \sum_{i=0}^{q_2} f_2^i \tag{4.8}$$

This force is distributed as the sum of q_1 i.i.d variables f_1^i, uniformly distributed in $[-f_0, f_0]$, and q_2 i.i.d variables f_2^i, uniformly distributed in $[f_0/10, f_0]$, therefore that it is distributed as the sum of two Irwing-Hall distributions (IH) $\Phi(q_1; -f_0, f_0)$ and $\Phi(q_2; f_0/10, f_0)$.

4. We hence define the probability density function of the force of the ensemble composed of n_1 motors in state A_1 and n_2 motors in state A_2 as:

$$P(F_{n_1,n_2} = \mathcal{F}) = \sum_{q_1,q_2=0}^{N} P(F_{q_1,q_2} = \mathcal{F}) P(n_1 = q_1, n_2 = q_2) \tag{4.9}$$

5. We now assume that $P(n_1 = q_1, n_2 = q_2) \neq 0 \qquad sse \qquad q_1, q_2 \gg 1$.

6. Further, we recall that an IH distribution for the sum of n i.i. uniformly distributed variables in the interval $(0, 1)$ $u^i \sim U(0, 1)$, can be approximated by a Gaussian distribution $\mathcal{G}(\mu, \sigma^2)$ for sufficiently large n:

$$\Phi(n; 0, 1) \xrightarrow{n \gg 0} \mathcal{G}\Big(\mu = \frac{n}{2}, \sigma^2 = \frac{n}{12}\Big) \quad . \tag{4.10}$$

Label $j = \{1, 2\}$ the two populations of motors. We seek at expressing the variables $f_j^i \sim U(a, b)$ in terms of the variables $u^i \sim U(0, 1)$.
If $u_i \sim U(0, 1)$, then $f_i = a - (b - a)u_i \sim U(a, b)$, and:

$$\sum_{i=1}^{n} f^i = \sum_{i=1}^{n} a - (b - a)u^i = na - (b - a)\sum_{i=1}^{n} u^i$$

with:

$$\sum_{i=1}^{n} u^i \sim \Phi(n; 0, 1) \xrightarrow{n \gg 0} \mathcal{G}\Big(\mu = \frac{n}{2}, \sigma = \frac{n}{12}\Big) \quad . \tag{4.11}$$

We obtain that the sum of n i.i. uniformly distributed variables f^i in the interval (a, b) is distributed (in the limit of large n) as a Gaussian distribution:

$$\mathcal{G}(f^i) = \frac{1}{b-a} \frac{\exp\left(-\frac{(\frac{f^i - na}{b-a} - \frac{n}{2})^2}{2\frac{n}{12}}\right)}{\sqrt{2\pi\frac{n}{12}}} = \frac{\exp\Big(-\frac{(f^i-\mu)^2}{2\sigma^2}\Big)}{\sqrt{2\pi\sigma^2}} \tag{4.12}$$

with parameters:

$$\begin{cases} \mu = na - \dfrac{n}{2}\big(b - a\big) = \dfrac{n}{2}\big(b + a\big) \\ \\ \sigma^2 = \dfrac{n}{12}\big(b - a\big) \end{cases} \tag{4.13}$$

7. Under the hypothesis 5, each IH distribution (one for each of the two populations of motors) can be approximated with a Gaussian distribution $\mathcal{G}(\mu_j, \sigma_j^2)$ with known parameters:

$$\sum_{i=0}^{q_1} f_1^i \sim \Phi(q_1; a_1, b_1) \xrightarrow{q_1 \gg 0} \mathcal{G}(\mu_1, \sigma_1^2) \qquad \begin{cases} \mu_1 = 0 \\ \sigma_1^2 = \frac{1}{3} q_1 f_0^2 \end{cases} \tag{4.14}$$

and

$$\sum_{i=0}^{q_2} f_2^i \sim \Phi(q_2; a_2, b_2) \xrightarrow{q_2 \gg 0} \mathcal{G}(\mu_2, \sigma_2^2) \qquad \begin{cases} \mu_2 = \frac{11}{20} q_2 f_0 \\ \\ \sigma_2^2 = \frac{27}{400} q_2 f_0^2 \end{cases} \tag{4.15}$$

Therefore $P(F_{q_1,q_2} = \mathcal{F})$ is a sum of two independent Gaussian distributions $\mathcal{G}(\mu_i, \sigma_i^2)$, which results in a Gaussian distribution with parameters:

$$F_{q_1,q_2} \sim \mathcal{G}(\mu_F, \sigma_F^2) \begin{cases} \mu_F = \mu_1 + \mu_2 = \frac{11}{20} q_2 f_0 \\ \\ \sigma_F^2 = \sigma_1^2 + \sigma_2^2 = (\frac{1}{3} q_1 + \frac{27}{400} q_2) f_0^2 \end{cases} \tag{4.16}$$

8. In conclusion the probability distribution of the force of an ensemble of n_1 motors in A_1 and n_2 motors in A_2 takes the following expression:

$$P_{F_{n_1,n_2}}(\mathcal{F}) = \sum_{q_1,q_2=0}^{N} \mathcal{G}\Big(\mu_F(q_1, f_0), \sigma_F^2(q_1, q_2, f_0)\Big) P(n_1 = q_1, n_2 = q_2) \tag{4.17}$$

with $P(n_1 = q_1, n_2 = q_2)$ stationary solution of the populations master equation (3.4).

4.1.3 Fitting procedure

We have derived an explicit expression for the theoretical probability distribution of the force exerted by two different force-generating populations of motors working in ensemble. We are now presenting the fitting procedure adopted to perform a parameters estimation on synthetically generated stochastic trajectories, under different temperature conditions. In order to take into account the contribution of motors in population A_1, we must consider the solution of the deterministic model obtained in the previous Section (without the adiabatic approximation exploited in the previous Chapter).
We will combine the deterministic and stochastic solution of the dynamics as follows. We consider the theoretical expression of the probability distribution of the force exerted by the ensemble of motors (4.17), and the solution of the mean field dynamics in the form (4.3), and compute their distances (mean square error) to the histogram of the isometric force at the plateau, and to the force development respectively, both obtained from synthetically generated stochastic data.

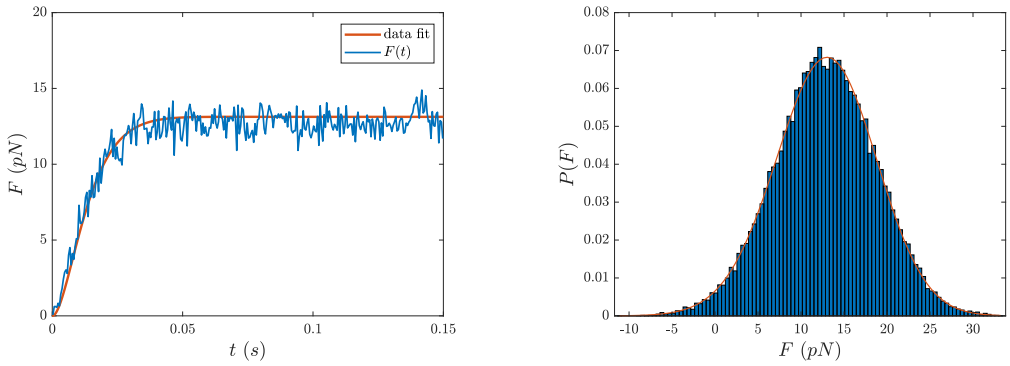

(a) *(b)*

Figure 4.1: ***Result of the fitting procedure on the force development and on the probability distribution of the force obtained from the stochastic simulations of the dynamics.***
a. *The trajectory of the force has been obtained averaging over* 600 *independent simulated trajectories. The force is measured in* pN *and it is exerted by a collection of* $N = 20$ *molecular motors with a suitable choice of the kinetic parameters and the force of a single motor* f_0. **b.** *Comparison of the empirical distribution of the force (histogram, in blue) and the analytical one* $P(F)$ *(line, in red).*

Adjusting the kinetic parameters to minimize these distances we provide an estimation of the force of a single molecular motor and of the duty ratio of the ensemble; the results of the fitting procedure of the force development and the force distribution at the isometric plateau are shown in Figure 4.1. From the inspection of Table 4.1 it can be appreciated that the estimates of f_0, r and ϕ are in good agreement with the values of the corresponding parameters set adopted to generate the synthetic data. The optimisation procedure is quite stable with respect to these parameters, as suggested by the small standard deviations obtained from different independent realisation of the fitting procedure. On the other hand, the values of the kinetic parameters k_i are not resolved in a satisfactory way by the optimisation as can be appreciated in Figure 4.2. This is due to the large degeneration of possible kinetics solutions corresponding to the same stationary distribution $P(F)$.
In the following Section we propose a procedure to extract kinetics information by considering the effect of temperature on the performance of the motors: including the temperature dependence guarantees a more reliable and robust parameter estimation strategy, allowing for a more precise gauge of the kinetic rates k_i.

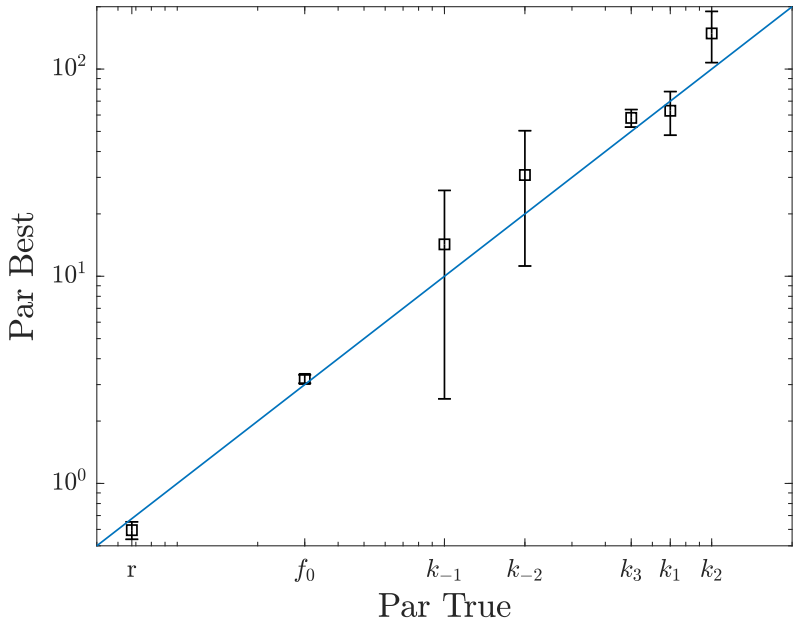

Figure 4.2: ***Estimated parameters from the synthetic data.***
The solid blue line represents the true parameters of the simulated dynamics, the symbols (mean ± SD) are obtained with the optimization procedure on simulated time series of the force of the ensemble. Both axes are plotted in log scale.

Table 4.1: ***Estimated parameters via the inverse scheme fed with simulated data.***
The parameters are: the force of a single motor f_0, the duty ratio of the ensemble r and the rate of transition through the attachment–detachment cycle ϕ. Mean and standard deviations are computed from different independent realisation of the optimisation procedure.

	F_0 (pN)	f_0 (pN)	r	$\phi(\mathrm{s}^{-1})$
True parameters	12.8	3.0	0.68	20
Estimated parameters	12.8	3.19 ± 0.15	0.60 ± 0.06	21 ± 2

4.2 Temperature dependence of the system's parameters

We consider two data sets that simulate the behaviour of the ensemble at different temperatures. We are going to show how it is possible to improve the robustness of the fitting scheme and provide an estimation of the order of magnitude of the kinetic rate constants of the dynamics. In order to be able to improve on the estimation of the kinetic parameters of the system we consider the temperature dependence of the probability per time unit associate to each transition between motor's configurations. Based on Arrenhius' theory of activated kinetic processes, the dependence of the reaction constants on the temperature of the system is assumed to be of the form:

$$k_i(T_2) = k_i(T_1) Q_i^{\frac{T_2 - T_1}{10\,^\circ\mathrm{C}}} \tag{4.18}$$

for each reaction constant $k_1, k_{-1}, k_2, k_{-2}, k_3$, and where Q_i is the temperature coefficient Q_{10} for the $i-$th reaction. In the following we will indicate as $\boldsymbol{k}(T)$ the set of kinetic rates at temperature T. Another assumption, in accord with [71], would be that the magnitude of the force of a single molecular motor is not affected by the temperature changes, meaning that the force of a single molecular motor in configuration A_1 and A_2 would be uniformly distributed in the intervals $\mathcal{I}_1 = [-f_0, f_0]$ and $\mathcal{I}_2 = [f_0/10, f_0]$ respectively, where f_0 is the force of a single correctly orientated motor at both temperature T_1 and T_2. With the previous assumptions we implemented the Gillespie algorithm to generate synthetic data sets for a system composed by N molecular motors, working at two different temperatures T_1 and T_2. We will exploit both the mean field solution of the dynamics and the probability distribution of the force of the ensemble of motors working at two different temperatures to perform a parameters estimation that allows to predict the order of magnitude values of the kinetic constant of the dynamics as well as the force of a single correctly oriented motor. The duty ratio of the ensemble can be computed following the relation (3.9).

4.2.1 Fitting procedure for data at different temperature

We consider two data sets of synthetically generated time series of the force of an ensemble constituted by a fixed number of N molecular motors, at two different temperatures T_1 and T_2, with $T_1 = 14\,^\circ\mathrm{C}$ and $T_2 = 34\,^\circ\mathrm{C}$. The fitting procedure described in Section 4.1.3 has been applied to both the data sets to estimate the force of a single correctly oriented motor f_0 and the kinetic constants $\boldsymbol{k}(T_1)$. The kinetic constants $\boldsymbol{k}(T_2)$ at temperature T_2 has been calculated with the relations (4.18), where we assumed the following values for the Q_10 factors: $Q_1 = Q_{-1} = Q_3 = 1.8$, $Q_2 = 4.6$ and $Q_{-2} = 2.5$. These values have been suitably chosen to mimic the temperature dependent performance of typical mammalian skeletal muscles as for described in [72]. The results of the fitting procedure performed on synthetic data with different temperature parameters T_1 and T_2 are shown in Figure 4.3, while the estimated parameters, compared with the ones assumed in the simulations of the dynamics (and labelled as "true parameters"), are listed in the Tables 4.2 and 4.3, and represented in Figure 4.4 in linear scale axes. A comparison between the results of the two procedures is shown in Figure 4.5, where the results obtained by analysing a single data sets are marked in red, while the results of the procedure that involves two different data sets at different temperature parameters are marked in black. From Figure

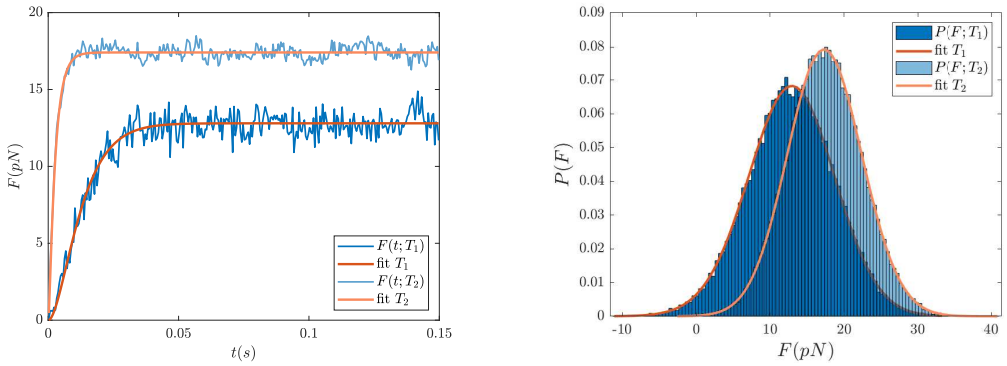

(a) *(b)*

Figure 4.3: ***Result of the fitting procedure on the force development and on the probability distribution of the force obtained from the stochastic simulations of the dynamics.***
The relevant parameters of the simulations are: $N = 20$, $f_0 = 3, T_1 = 14\,^{\circ}\mathrm{C}$ *and* $T_2 = 34\,^{\circ}\mathrm{C}$, *while the values of the* Q_{10} *factors are listed in the text, and the kinetic constants are:* $\boldsymbol{k} = (70, 10, 100, 20, 50)$. **a.** *The trajectory of the force has been obtained averaging over* 600 *independent stochastic simulations.* **b.** *The histogram of the force of the ensemble at the isometric plateau is fitted against the analytical profile, via a self–consistent optimisation procedure which aims at estimating the kinetic parameters and the force of a single motor* f_0.

4.5 it is possible to see an improvement of the results for the average values of the kinetic constants (obtained from independent iterations of the stochastic fitting), compared with the values obtained when we analyse only a single data set. Figure 4.6 displays the plane (f_0, r), where the solutions of the mean field dynamics are represented by the two hyperbolae, the one above corresponding to the data set with the lower temperature T_1, while the symbols are the results of the analysis of the probability distribution of the force fluctuations around the isometric plateau, exerted by the ensemble of motors.
In the next Section we propose a further simplification of the fitting procedure that involve an approximated expression for the motors probability distribution.

Table 4.2: ***Estimated parameters via the inverse scheme fed with simulated data.***

	F_0 (pN)	f_0 (pN)	r
True parameters	12.8	3.0	0.68
Estimated parameters	12.8	3.19 ± 0.4	0.68 ± 0.08

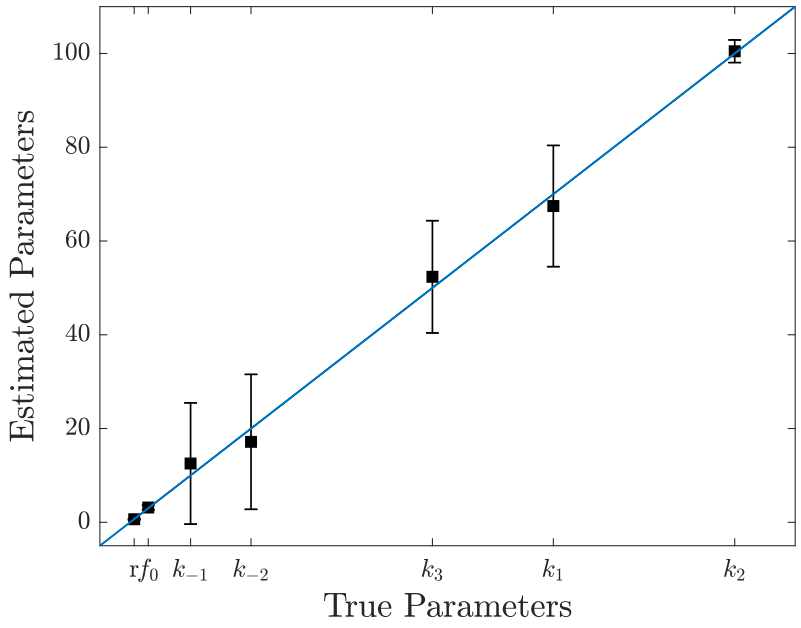

Figure 4.4: ***Estimated parameters from the synthetic data.*** *The solid blue line represents the true parameters of the simulated dynamics, the symbols (mean ± SD) are obtained with the optimisation procedure that employs two force data sets at different temperature parameters. The results shown are relative to the data set at the temperature* $T_1 = 14\,^{\circ}\mathrm{C}$.

Table 4.3: ***Estimated parameters via the inverse scheme fed with simulated data.*** *The kinetic parameters* $\mathbf{k}$ *are all expressed in* (s^{-1}).

	$k_1(T_1)$	$k_{-1}(T_1)$	$k_2(T_1)$	$k_{-2}(T_1)$	$k_3(T_1)$
True parameters	70	10	100	20	50
Estimated parameters	69 ± 9	9 ± 8	100 ± 2	21 ± 9	51 ± 8

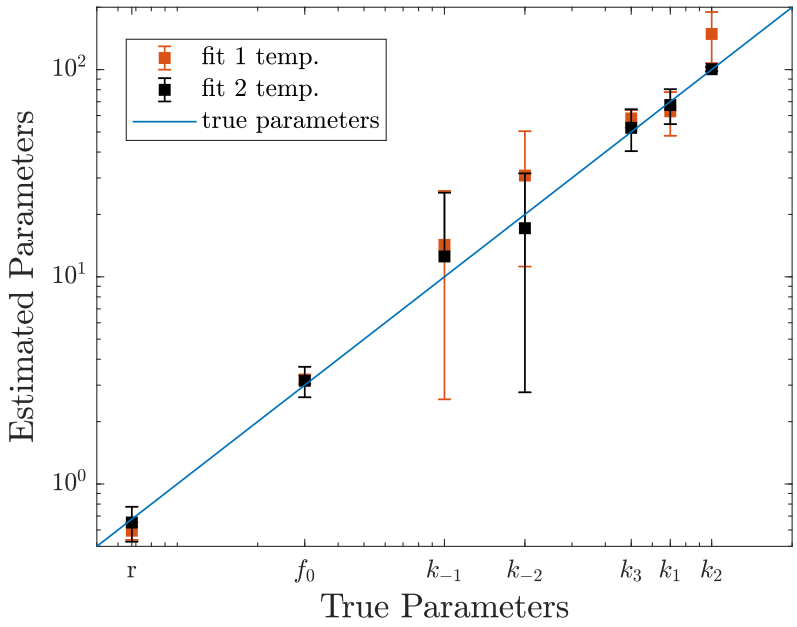

Figure 4.5: ***Comparison between different procedures.***
The solid blue line represents the true parameters of the simulated dynamics, the red symbols (mean ± SD) refers to the results of the optimisation procedure conducted with a single data set at temperature T_1, while black symbols (mean ± SD) are obtained with the optimisation procedure on two simulated time series of the force of the ensemble at different temperatures T_1 and T_2.

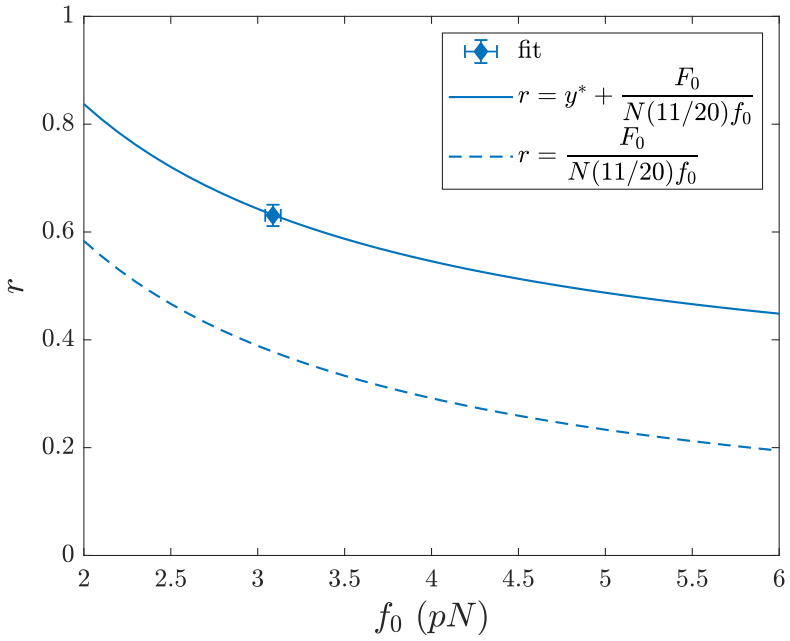

Figure 4.6: ***Estimated*** (f_0, r) ***from the synthetic data.***
The symbol (mean $\pm$ *SD) represents the solution of the optimisations procedure for the force of a single motors* f_0*, and the duty ratio of the ensemble* r*. The solid line represents the expression of the duty ratio of the ensemble as it follows from the mean field model, with the mean field solution for* y^* *expressed as a function of the estimated kinetic parameters of the system. The dashed line represent the duty ratio as previously estimated without taking into account the contribution of the motors in configuration* A_1*.*

4.3 Gaussian noise approximation for the motors populations

We are now exploring another useful approximation of the dynamics of the stochastic system. We are interested in an expression for the probability distribution of the populations dynamics, that involves the Gaussian noise approximation carried out on the master equation that describes the evolution of the probability distribution associated with the microscopic states of the system. We observe that the marginal stationary solutions of the master equation $P^{\mathrm{ST}}(n_1)$ and $P^{\mathrm{ST}}(n_2)$, depicted in Figure 3.4 resemble normal distributions when the values of the fractions of motors are sufficiently far from the boundaries, i.e. for $n_1/N, n_2/N \gg 0$ and $n_1/N, n_2/N \ll 1$. We then consider the probability distribution of the total force of the ensemble:

$$P_{F_{n_1,n_2}}(\mathcal{F}) = \sum_{q_1,q_2=0}^{N} P_{F_{q_1,q_2}} P(n_1 = q_1, n_2 = q_2) \tag{4.19}$$

where $P_{F_{q_1,q_2}}(\mathcal{F}) \equiv \mathcal{G}\Big(\mu_F = \mu(q_1, f_0), \sigma_F^2 = \sigma^2(q_1, q_2, f_0)\Big)$ is the Gaussian distribution obtained in Section 4.1. In order to carry out the Gaussian noise approximation for the populations of motors we define the discrete number of motors in configuration j as $n_j = Nx_j$ where x_j is the "discrete" concentration of the motors in configuration j. Now we can express the stationary solution of the master equation in terms of the concentrations variables: $P(n_1 = q_1, n_2 = q_2) = P(Nx_1 = q_1, Nx_2 = q_2)$ or $P(x_1 = \frac{q_1}{N}, x_2 = \frac{q_2}{N})$. In the limit $x_j \gg 1$ it is possible to perform a system size expansion of the master equation, a perturbative approach named the Van Kampen approximation [73], in order to obtain a linear Fokker-Planck equation for the probability distribution of the fluctuations, around the mean field solution, associated with the concentration of the two force-generating motors populations. The stationary solution of the Fokker-Planck equation (i.e. the solution calculated when $\langle \boldsymbol{x} \rangle = \boldsymbol{x}^*$), written in terms of the concentration of motors is a bivariate Gaussian distribution, centred on the mean field solution of the dynamics of the system. The standard calculations carried out to obtain the Fokker-Planck equation and its solution from the master equation will be explicitly obtained in the next Section. This solution can be inserted in equation (4.19) as an expression for $P(n_1 = q_1, n_2 = q_2)$ to be adopted instead of the exact solution of the master equation, which can be computationally expensive to be used in the fitting procedure. The results of the parameters estimation on synthetic data sets will be presented in the last Section of this Chapter.

4.3.1 Details of the Van Kampen expansion

To quantify the statistics of the fluctuations around the stationary state we consider the master equation in the form (3.4) and we perform an expansion in the system size N. The first order of the expansion $(1/\sqrt{N})$ results in the means field equations for the populations of motors, while the second order of the expansion $(1/N)$ yields a Fokker-Planck equation for the probability distribution of the finite size fluctuations around the stationary state, for each populations of motors. Following the Van Kampen hypotheses, when the system size is large but finite $N \gg 1$, the discrete concentrations n_1/N and

n_2/N will differ from the mean field fractions of motors by a contribution of magnitude $1/\sqrt{N}$ (as follows from the Central Limit Theorem):

$$\frac{n_1(t)}{N} = y^*(t) + \frac{\xi}{\sqrt{N}} \qquad \text{and} \qquad \frac{n_2(t)}{N} = z^*(t) + \frac{\eta}{\sqrt{N}} \tag{4.20}$$

where y^* and z^* are defined in equation (4.3), and ξ and η are the fluctuations associated with the number of motors in A_1 and A_2 respectively.
To simplify the notation we recall that the number of motors in the actin-attached configurations at the time t is indicated by $\boldsymbol{n}(t) = (n_1(t), n_2(t))$, and we define the vector containing the fractions of attached motors:

$$\boldsymbol{x} = (y, z) \qquad \text{therefore} \qquad \boldsymbol{x^*} = (y^*, z^*) \tag{4.21}$$

The associated fluctuations will be defined as: $\boldsymbol{\lambda} = (\xi, \eta)$.
These stochastic variables have a probability distribution $\Pi(\boldsymbol{\lambda}, t)$ defined by the following expression:

$$\Pi(\boldsymbol{\lambda}, t) \equiv P\big(\boldsymbol{n}; t\big) = P\Big(y + \frac{\xi}{\sqrt{N}}, z + \frac{\eta}{\sqrt{N}}; t\Big) \tag{4.22}$$

according to the Van Kampen hypothesis (4.20).
The time evolution of the probability distribution $\Pi(\boldsymbol{\lambda}, t)$ is characterised by deriving the previous expression in respect of time:

$$\begin{aligned} \frac{\partial P}{\partial t} &= \frac{1}{N}\frac{\partial \Pi}{\partial \tau} - \frac{1}{\sqrt{N}} \sum_{i=1}^{2} \frac{\partial \Pi}{\partial \lambda_i} \frac{dx_i}{d\tau} = \\ &= \frac{1}{\sqrt{N}} \Big(\frac{\partial P}{\partial t}\Big)_{1/\sqrt{N}} + \frac{1}{N}\Big(\frac{\partial P}{\partial t}\Big)_{1/N} + \mathcal{O}(N^{-3/2}) \end{aligned} \tag{4.23}$$

where we separated the two contributions of magnitude $1/\sqrt{N}$ and $1/N$.
To calculate these two contributions we write the master equations in terms of step operators $\epsilon_i^{\pm}$ defined by their action:

$$\epsilon_i^{\pm} T(n_i|n_i) P(n_i, t) = T(n_i \pm 1 | n_i \pm 1) P(n_i \pm 1, t) \tag{4.24}$$

and, recalling the expressions for the transition rates (3.3) defined in Chapter 3 we obtain:

$$\begin{aligned} \frac{\partial P(\boldsymbol{n}, t)}{\partial t} =& (\epsilon_1^- - 1) T_1 P(\boldsymbol{n}, t) + (\epsilon_1^+ - 1) T_{-1} P(\boldsymbol{n}, t) + (\epsilon_1^+ \epsilon_2^- - 1) T_2 P(\boldsymbol{n}, t) + \\ &+ (\epsilon_1^- \epsilon_2^+ - 1) T_{-2} P(\boldsymbol{n}, t) + (\epsilon_2^+ - 1) T_3 P(\boldsymbol{n}, t) \ . \end{aligned} \tag{4.25}$$

We now expand both the step operators and the transition rates up to the second order (N), in the limit $1/\sqrt{N} \ll 1$. Observing that:

$$n_i \pm 1 = \pm 1 + N\Big(x_i + \frac{\lambda_i}{\sqrt{N}}\Big) = \pm 1 + N x_i + \sqrt{N}\lambda_i$$

we get:

$$\epsilon_i^{\pm} \approx \mathbb{1} \pm \frac{1}{\sqrt{N}}\partial_{\lambda_i} + \frac{1}{2N}\partial^2_{\lambda_i} + \mathcal{O}(N^{-3/2})$$

$$\epsilon_i^{\pm}\epsilon_j^{\mp} \approx \mathbb{1} \mp \frac{1}{\sqrt{N}}\partial_{\lambda_j} + \frac{1}{2N}\partial^2_{\lambda_j} \pm \frac{1}{\sqrt{N}}\partial_{\lambda_i} - \frac{1}{N}\partial_{\lambda_i}\partial_{\lambda_j} + \frac{1}{2N}\partial^2_{\lambda_i} + \mathcal{O}(N^{-3/2}) \approx$$
$$\approx \mathbb{1} + \frac{1}{\sqrt{N}}(\pm\partial_{\lambda_i} \mp \partial_{\lambda_j}) + \frac{1}{2N}(\partial^2_{\lambda_i} - \partial^2_{\lambda_j} + 2\partial^2_{\lambda_i\lambda_j})$$

and for the transition rates:

$$T_1 \approx k_1\Big[1 - y - z - \frac{(\xi+\eta)}{\sqrt{N}}\Big] \qquad \text{and} \qquad T_{-1} \approx k_{-1}\Big(y + \frac{\xi}{\sqrt{N}}\Big)$$
$$T_2 \approx k_2\Big(y + \frac{\xi}{\sqrt{N}}\Big) \qquad \text{and} \qquad T_{-2} \approx k_{-2}\Big(z + \frac{\eta}{\sqrt{N}}\Big)$$
$$T_3 \approx k_3\Big(z + \frac{\eta}{\sqrt{N}}\Big)$$

Substituting these expressions in the master equation (4.25) and comparing the results with the equation (4.23), we find that the first term on the right hand side (the leading order of the expansion) coincides with the set of differential equations that governs the mean field dynamics of the system (3.6). The second term on the right hand side results to be:

$$\Big(\frac{\partial P}{\partial t}\Big)_{1/N} = \frac{\partial \Pi}{\partial t} = -\,\partial_\xi(A_1\Pi(\lambda;t)) - \partial_\eta(A_2\Pi(\lambda;t)) + \frac{1}{2}\Big[\partial^2_{\xi^2}(B_{11}\Pi(\lambda;t)) +$$
$$+ \partial^2_{\eta^2}(B_{22}\Pi(\lambda;t)) + \partial_\xi\partial_\eta(B_{12}\Pi(\lambda;t)) + \partial_\eta\partial_\xi(B_{21}\Pi(\lambda;t))\Big]$$

where $\boldsymbol{A}(\boldsymbol{\lambda}) = M\boldsymbol{\lambda}^T$. Matrices M and B, respectively the drift matrix and the diffusion matrix are:

$$M = \begin{pmatrix} -(k_1 + k_{-1} + k_2) & -(k_1 - k_{-2}) \\ k_2 & -(k_{-2} + k_3) \end{pmatrix} \tag{4.26}$$

which coincides in the deterministic limit, with the jacobian matrix of the system (4.2), and:

$$B = \begin{pmatrix} k_1(1-y-z) + (k_{-1}+k_2)y + k_{-2}z & -k_2y + k_{-2}z \\ -k_2y + k_{-2}z & k_2y + (-k_2 + k_3)z \end{pmatrix} \tag{4.27}$$

which is a symmetric and positive definite matrix.
The previous expression can be written as standard Fokker-Plank equation in the form:

$$\frac{\partial \Pi(\boldsymbol{\lambda},t)}{\partial t} = -\sum_{i=1}\frac{\partial}{\partial\lambda_i}\Big[A_i(\boldsymbol{\lambda})\Pi(\boldsymbol{\lambda},t)\Big] + \frac{1}{2}\sum_{i,j=1}^{2}\frac{\partial^2}{\partial\lambda_i\partial\lambda_j}\Big[B_{ij}(\boldsymbol{\lambda})\Pi(\boldsymbol{\lambda},t)\Big]\,. \tag{4.28}$$

The Van Kampen approximation allowed us to decouple the deterministic and the stochastic dynamics of the system, which results in local fluctuations around the mean

field stationary state. Summarising, the second order in $\sqrt{N}$ of the expansion yields a Fokker-Planck equation for the probability distribution of the fluctuations, associated with the populations of motors in the actin-attached configurations. The general solution of the Fokker-Planck equation (4.28) [73], is a bivariate Gaussian distribution, that can be characterised by its moments. Performing the standard calculations, the equation that describes the time evolution of he first moment of the distribution is, for each component, the linear differential equation is:

$$\frac{d\left\langle \lambda_i \right\rangle}{d\tau} = \sum_{k=1}^{2} M_{ik} \left\langle \lambda_k \right\rangle = \left\langle A_i \right\rangle \tag{4.29}$$

or, in components:

$$\begin{aligned} \langle \dot{\xi} \rangle &= \langle A_1 \rangle = \sum_{k=1}^{2} M_{1k} \langle \lambda_k \rangle = (k_1 + k_{-1} + k_2) \langle \xi \rangle - (k_1 - k_{-2}) \langle \eta \rangle \\ \langle \dot{\eta} \rangle &= \langle A_2 \rangle = \sum_{k=1}^{2} M_{2k} \langle \lambda_k \rangle = k_2 \langle \xi \rangle - (k_{-2} + k_3) \langle \eta \rangle \end{aligned} \tag{4.30}$$

that implies that for $\langle \dot{\boldsymbol{\lambda}} \rangle = 0$ we have $\langle \lambda_i \rangle = 0$ for $i = 1, 2$, accordingly with the Van Kampen ansatz.
For the second moment of the distribution we obtain the following set of differential equations, for the diagonal components:

$$\frac{d\left\langle \lambda_i^2 \right\rangle}{d\tau} = 2 \sum_{k=1}^{2} M_{ik} \left\langle \lambda_i \lambda_k \right\rangle + B_{ii} = 2 \left\langle \lambda_i A_i \right\rangle + B_{ii} \tag{4.31}$$

and for the off-diagonal ones:

$$\begin{aligned} \frac{d\left\langle \lambda_i \lambda_j \right\rangle}{d\tau} &= \sum_{k=1}^{2} \Big(M_{ik} \left\langle \lambda_j \lambda_k \right\rangle + M_{jk} \left\langle \lambda_j \lambda_k \right\rangle \Big) + \frac{1}{2} B_{ij} + \frac{1}{2} B_{ji} = \\ &= \langle \xi_j A_i \rangle + \langle \xi_i A_j \rangle + \frac{1}{2} (B_{ij} + B_{ji}) \end{aligned} \tag{4.32}$$

or, in components:

$$\begin{aligned} \langle \dot{\xi^2} \rangle &= 2 \sum_{k=1}^{2} M_{1k} \langle \xi \lambda_k \rangle + B_{11} \qquad\qquad \langle \dot{\eta^2} \rangle = 2 \sum_{k=1}^{2} M_{2k} \langle \eta \lambda_k \rangle + B_{22} \\ &\langle \dot{\xi \eta} \rangle = \sum_{k=1}^{2} M_{1k} \langle \eta \lambda_k \rangle + M_{2k} \langle \xi \lambda_k \rangle + B_{12} \end{aligned} \tag{4.33}$$

where $B_{12} = B_{21}$.
We now define the vector of the second moments of the distribution as $\boldsymbol{\zeta} = \Big(\langle \xi^2 \rangle \quad \langle \eta^2 \rangle \quad \langle \xi \eta \rangle \Big)^T$, that satisfies the following equation for the time evolution:

$$\langle \dot{\boldsymbol{\zeta}} \rangle = \mathcal{M} \langle \boldsymbol{\zeta} \rangle + \boldsymbol{b} \tag{4.34}$$

where $\boldsymbol{b} = (B_{11} \quad B_{22} \quad B_{12})^T$, and $\mathcal{M}$ is the matrix with the following elements:

$$\mathcal{M} = \begin{pmatrix} 2J_{11} & 0 & 2J_{12} \\ 0 & 2J_{22} & 2J_{21} \\ J_{21} & J_{12} & (J_{11} + J_{22}) \end{pmatrix} \tag{4.35}$$

Being interested in the solution of the previous equation for the dynamics of the fluctuations around the stationary state we are interesting to solve the previous equation when $\langle \dot{\boldsymbol{\zeta}} \rangle = 0$, i.e.:

$$\langle \boldsymbol{\zeta} \rangle = -\mathcal{M}^{-1}\boldsymbol{b} \ . \tag{4.36}$$

The solution of the Fokker-Planck equation (4.28) has the explicit form:

$$\Pi(\boldsymbol{\lambda}; t) = \frac{\exp\Big(-\frac{1}{2}\Big[(\boldsymbol{\lambda} - \langle \boldsymbol{\lambda} \rangle)^T \Sigma^{-1} (\boldsymbol{\lambda} - \langle \boldsymbol{\lambda} \rangle)\Big]\Big)}{2\pi\sqrt{det(\Sigma)}} \tag{4.37}$$

where $\langle \boldsymbol{\lambda} \rangle = (\langle \xi \rangle \quad \langle \eta \rangle)^T$ is the mean value of the vector of the fluctuations of the two motors populations, and Σ is the covariance matrix with elements:

$$\Sigma = \begin{pmatrix} \langle \xi^2 \rangle & \langle \xi\eta \rangle \\ \langle \xi\eta \rangle & \langle \eta^2 \rangle \end{pmatrix} \tag{4.38}$$

Equation (4.28) can be expressed in terms of the components of the fluctuations associated with the two motors population as:

$$\Pi(\xi, \eta; t) = \frac{\exp\left(-\frac{1}{2(1-\rho^2)}\left[\frac{(\xi - \langle \xi \rangle)^2}{\langle \xi^2 \rangle} - 2\rho\frac{(\xi - \langle \xi \rangle)(\eta - \langle \eta \rangle)}{\sqrt{\langle \xi^2 \rangle \langle \eta^2 \rangle}} + \frac{(\eta - \langle \eta \rangle)}{\langle \eta^2 \rangle}\right]\right)}{2\pi\sqrt{\langle \xi^2 \rangle \langle \eta^2 \rangle (1 - \rho^2)}} \tag{4.39}$$

where the correlation coefficient ρ is defined as:

$$\rho = \frac{\langle \xi\eta \rangle}{\sqrt{\langle \xi^2 \rangle \langle \eta^2 \rangle}} \ . \tag{4.40}$$

We are interested in the solution of the Fokker-Planck equation expressed for the number of motors in the actin-attached configurations, i.e. n_1 and n_2, which is:

$$P(n_1, n_2) = \frac{\exp\left(-\frac{1}{2(1-\rho^2)N}\left[\frac{(n_1 - Ny^*)^2}{\langle \xi^2 \rangle} - 2\rho\frac{(n_1 - Ny^*)(n_2 - Nz^*)}{\sqrt{\langle \xi^2 \rangle \langle \eta^2 \rangle}} + \frac{(n_2 - Nz^*)^2}{\langle \eta^2 \rangle}\right]\right)}{2\pi\sqrt{N^2 \langle \xi^2 \rangle \langle \eta^2 \rangle (1 - \rho^2)}} \tag{4.41}$$

where we have exploited that $\langle \xi \rangle = \langle \lambda \rangle = 0$ from (4.30), $\xi = \frac{(n_1 - Ny^*)}{\sqrt{N}}$ from the Van Kampen hypotheses (4.20) and that $\Sigma_{\boldsymbol{\lambda}} = \frac{\Sigma_{\boldsymbol{n}}}{N}$.
Before we proceed to utilise this expression in the definition of the probability distribution of the force, we must inspect if this approximation is satisfying for the conditions under which we performed the stochastic simulations of the system dynamics. In Figure 4.7 we can see the $2D$ histogram of the stationary probability distribution $P(n_1, n_2)$ obtained from the Gillespie simulation of a stochastic trajectory (on the left), and the corresponding function derived by the implementation of the Van Kampen approximation on the master equation (on the right). The agreement between the two results is satisfactory when we

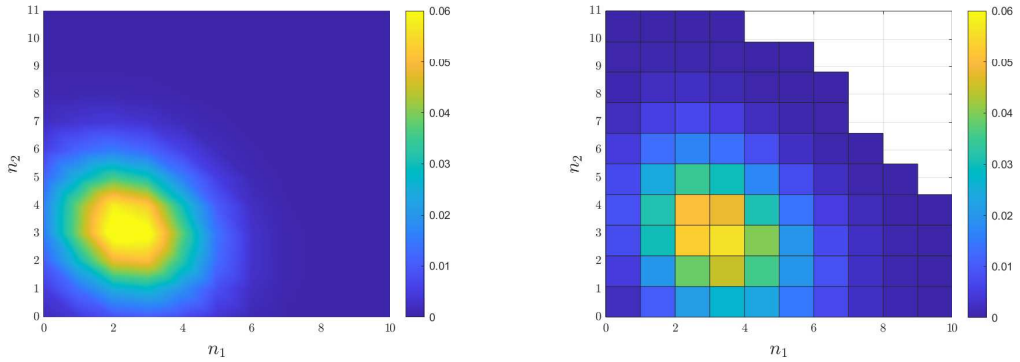

(a) (b)

Figure 4.7: ***Checking on the Van Kampen approximation.*** *Probability density function $P(n_1, n_2)$ associated to the stationary concentrations of force-generating motors,* (a) *as obtained from stochastic simulations data, and* (b) *from the analytical solution obtained via the Van Kampen approximation.*

consider a set of kinetic rates that correspond to average fractions of motors that are sufficiently different from zero in the stationary state, i.e. $\langle n_1 \rangle, \langle n_2 \rangle \gg 0$.

By inserting expression (4.41) in the probability distribution of the total force of the ensemble (4.17) (replacing the exact solution of the master equation), when considering the continuous limit for the concentrations, we find:

$$\begin{aligned} P_{F_{n_1,n_2}}(\mathcal{F}) &= \int_0^N dq_1 \int_0^N dq_2 \, P_{F_{q_1,q_2}}(\mathcal{F}) \, P(Ny = q_1, Nz = q_2) = \\ &= \int_0^N dq_1 \int_0^N dq_2 \, \mathcal{G}\Big(\boldsymbol{\mu}_F, \boldsymbol{\sigma}_{\boldsymbol{F}}\Big) \, \mathcal{G}\Big(\boldsymbol{x}^*, \frac{1}{N}\boldsymbol{\Sigma}\Big) = \\ &= \int_{-\infty}^{+\infty} dx_1 \int_{-\infty}^{+\infty} dx_2 \, \frac{e^{-\frac{(\mathcal{F}-\mu_F)^2}{2\sigma_F^2}}}{\sqrt{2\pi\sigma_F^2}} \, \frac{e^{-\frac{1}{2N}(\boldsymbol{x}-\boldsymbol{x}^*)^T\Sigma^{-1}(\boldsymbol{x}-\boldsymbol{x}^*)}}{2\pi\sqrt{N^2 \det(\Sigma)}} \end{aligned} \tag{4.42}$$

The integral can be numerically evaluated and exploited to perform a fitting procedure that does not involve the calculations needed to solve the master equation.
The results of this procedure will be presented in the next Section.

4.3.2 Fitting scheme for data at different temperatures

In this Section we show the results of the new approach that exploits the functional form (4.42) for the probability distribution of the total force of the ensemble to perform the parameters estimation on data sets numerically generated with different temperature parameters for which the Van Kampen approximation can be carried out. In Figure 4.8 are shown the results of the fitting procedure on the force development and on the probability distribution of the force of the ensemble. The average values of the parameters obtained with this method are in good accord with the parameters adopted to generate the simulated trajectories, as can be appreciated inspecting the results reported in Table 4.4. In Figure 4.9 it is shown the result of the fitting procedure in the plane (f_0, r), where

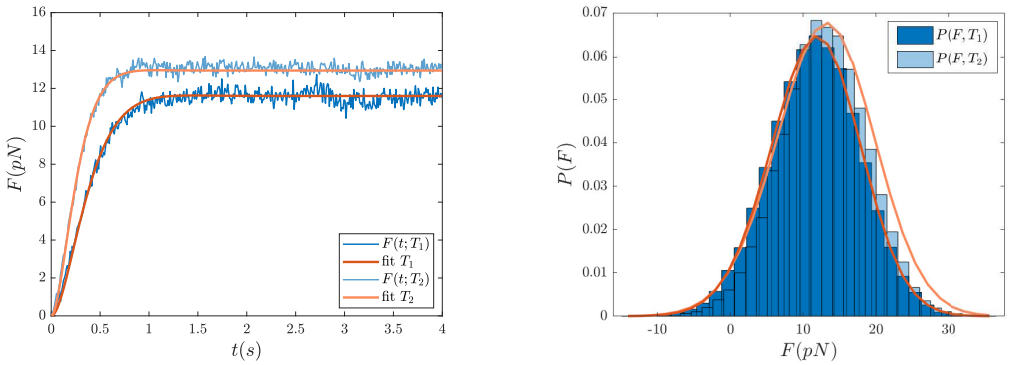

(a) *(b)*

Figure 4.8: ***Result of the fitting procedure on the force development and on the probability distribution of the force obtained from the stochastic simulations of the dynamics.***
The relevant parameters of the simulations are: $N = 20$, $f_0 = 3, T_1 = 10\,^\circ\mathrm{C}$ *(darker colours) and* $T_2 = 14\,^\circ\mathrm{C}$ *(lighter colours), while the values of the* Q_{10} *factors are listed in the text, and the kinetic constants are:* $\boldsymbol{k} = (70, 10, 100, 20, 50)$. **a.** *The trajectory of the force has been obtained averaging over* 800 *independent simulated trajectories.* **b.** *The histogram of the force of the ensemble at the isometric plateau is fitted against the analytical profile, via a self-consistent optimisation procedure which aims at estimating the kinetic parameters and the force of a single motor* f_0.

the solutions of the mean field dynamics are represented by the two hyperbolae, the one above corresponding to the data set with the lower temperature T_1, while the dashed blue line represents the duty ratio as previously estimated without taking into account the contribution of the motors in configuration A_1. The symbols are the results of the analysis of the probability distribution of the force fluctuations around the isometric plateau, exerted by the ensemble of motors.

Table 4.4: ***Estimated parameters via the inverse scheme fed with simulated data.***

	F_0 (pN)	f_0 (pN)	r
True parameters	11.6	3.0	0.70
Estimated parameters	11.6	3.12 ± 0.2	0.66 ± 0.02

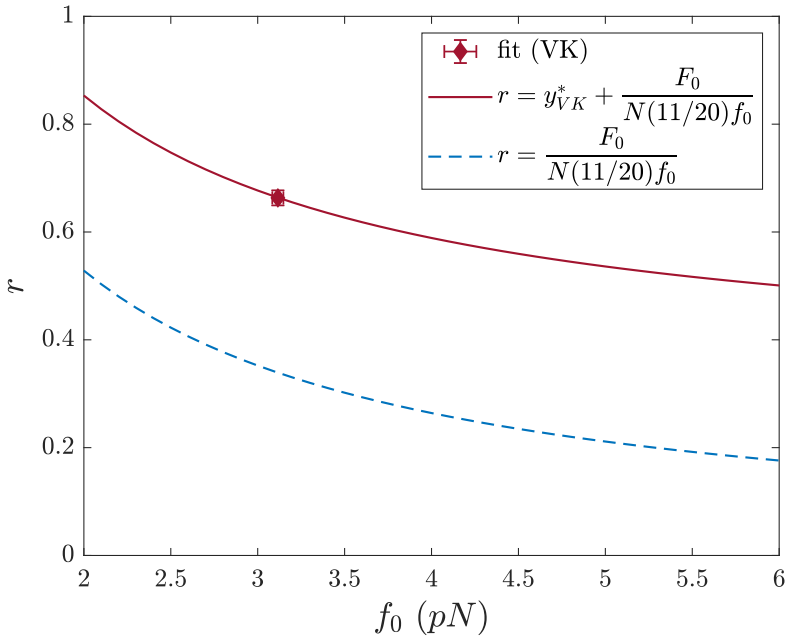

Figure 4.9: ***Estimated parameters*** $(\boldsymbol{f_0}, \boldsymbol{r})$ ***from the synthetic data.*** *The red symbol (mean ± SD) represents the solution of the optimisations procedure for the force of a single motors f_0, and the duty ratio of the ensemble r. The solid red line represents the expression of the duty ratio of the ensemble as it follows from the mean field model, with the mean field solution for y^* expressed as a function of the kinetic parameters of the system. The dashed blue line represents the duty ratio as previously estimated without taking into account the contribution of the motors in configuration A_1.*

Chapter 5

Results and discussion

In this Chapter we present and discuss the results obtained by the combined experimental and theoretical approach described in Chapters 2 and 3, to provide an estimate of the relevant parameters underlying the generation of force of an ensemble of slow and fast skeletal HMMs performing isometric contractions, at room temperature. Under this condition it is possible to employ the theoretical approach developed in Chapter 3 which accounts for only one population of force-generating motors. Future experimental work it is planned to investigate the low-temperature regime, when the force of the ensemble is significantly affected by the change in proportion of motors in different force-generating states.

5.1 Parameters estimation on the experimental output of the nanomachine powered by skeletal HMMs

Before applying the procedure detailed in Section 3.5 of Chapter 3 to the experimental data and present the results we recall the relevant steps that define the envisaged fitting strategy:

1. The first step amounts to analyse the time evolution of the force in its mean field approximation: the asymptotic force F_0 and the time scale a, as defined above, are extracted via a direct - two parameters - fit that exploits expression 3.23.

2. We turn to study the distribution of the fluctuation of the force around the equilibrium value. To this end we make use of $\boldsymbol{P}^{\mathrm{st}}$.

3. From $\boldsymbol{P}^{\mathrm{st}}$ we extract the $N+1$ marginal probabilities ρ_q, namely the probabilities to find $q \leq N$ motors in the force-generating configuration A_2. This is achieved by summing over $n_1 = 0, \ldots, N$ the stationary probability distribution $\boldsymbol{P}^{\mathrm{st}}$.

4. We then make use of the marginal probabilities $(\rho_0, \rho_1, \rho_2, \ldots, \rho_N)$ to weight the probability distributions $\Pi_q(f)$ of the force exerted by a set of q motors. These latter are computed as generalised Irwing-Hall distributions for independent and identically distributed random variables f drawn from the considered interval I_2. The distribution of the force is hence estimated as $P(F) = \sum_{q=0}^{N} \rho_q \Pi_q(f)$.

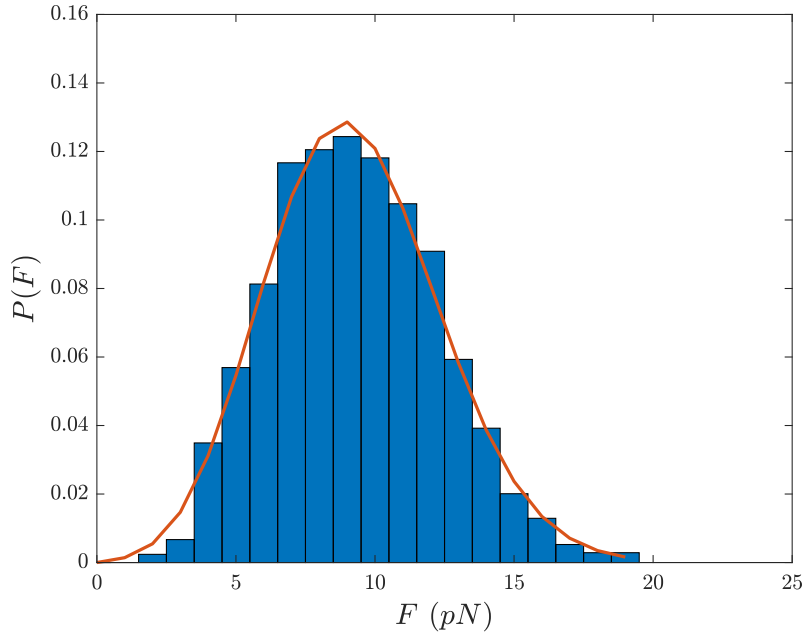

Figure 5.1: ***Result of the fitting procedure on the soleus HMMs ensemble isometric force.*** *The histogram of the soleus HMMs force at the isometric plateau is fitted against the analytical profile, via a self-consistent optimisation procedure which aims at estimating the unknown kinetic parameters.*

5. For fixed size N (previously estimated by the counting of rupture events in ATP-free solution, see also at the end of the ext Section where the possibility to modulate N is accounted for) we adjust the kinetic rate constants $k_1, k_{-1}, k_2, k_{-2}, k_3$, so as to minimise the root mean square distance between the recorded distribution and its analytic estimate. The best fit values are used to compute the parameter b and thus determine the sought estimates for r and f_0, as well as the rate of motors detaching from the actin, i.e. ϕ.

We now proceed by applying the validated procedure to the experimental data collected with the nanomachine powered by slow and fast myosin isoforms. As mentioned, the number of available molecular motors ($N = 16$) estimated from number of ruptures in rigor for both isoforms (Figure 2.3), is assumed as the reference value in the following, unless otherwise specified. We interpolate the distribution of the fluctuations as recorded experimentally, given the analytical solution obtained above. A representative example of the fitting outcome for the soleus HMMs ensemble is reported in the Figure 5.1; the histogram is generated from the experimental data series of the isometric force in the stationary state (i.e. at the isometric plateau). In Figure 5.2 the results of the analysis are plotted in the parameters plane (f_0, r) (symbols and lines refer to different isoforms according to the colour: blue for psoas, red for soleus; different tones identify different experiments). The solid lines highlight the ensemble of distinct - though equivalent - solutions ensuing from the average force profile, which would follow from solely inspecting the average force profile. By accounting for the fluctuations one breaks the degeneracy inherent to the system when analysed in its mean field version, getting just one pair

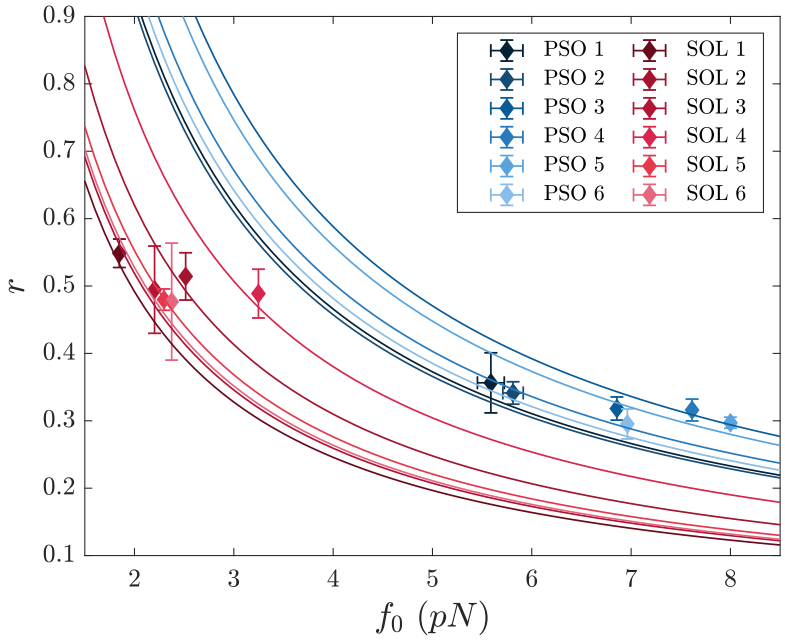

Figure 5.2: ***Estimated motor force f_0 and fraction of attached motors r from the experimental data.*** *Best fit parameters from the experimental data sets of rabbit soleus HMMs (red symbols) and rabbit psoas HMMs (blue symbols). Mean values and standard deviations are obtained by averaging over 20 independent realisations of the stochastic fitting procedure for each data record. Different tones refers to different experiments. Each solid line represents the hyperbola on which each of the pair (f_0, r) is constrained to be, according to the mean field analysis.*

(f_0, r) (identified by the symbol) compatible with each individual experimental curve. The quantitative results of the fitting procedure and the parameters estimation performed on the experimental data sets from both rabbit psoas and rabbit soleus are listed in Table 5.1 and Table 5.2 respectively.

Table 5.1: ***Estimated parameters for psoas data.***

Exp	F_0 (pN)	f_0 (pN)	r	$\phi(\mathrm{s}^{-1})$
PSO 1	16.4	5.6	0.36	6.4
PSO 2	16.1	5.8	0.34	6.1
PSO 3	20.7	7.6	0.32	6.2
PSO 4	17.7	6.9	0.32	5.9
PSO 5	19.7	8.0	0.30	5.8
PSO 6	17.0	7.0	0.30	5.8
$mean \pm SD$	17.9 ± 1.9	6.8 ± 1.0	0.32 ± 0.02	6.0 ± 0.2

In Table 5.3 is shown the quantitative comparison between the estimated mean values and standard deviations for f_0, r and ϕ, for both the psoas and the soleus HMMs.

Table 5.2: ***Estimated parameters for soleus data.***

Exp	F_0 (pN)	f_0 (pN)	r	$\phi(\mathrm{s}^{-1})$
SOL 1	8.7	1.8	0.55	2.25
SOL 2	10.9	2.5	0.51	2.27
SOL 3	9.1	2.2	0.49	2.29
SOL 4	13.4	3.2	0.49	2.26
SOL 5	9.7	2.3	0.48	2.34
SOL 6	9.3	2.4	0.48	2.23
$mean \pm SD$	10.2 ± 1.7	2.4 ± 0.4	0.50 ± 0.03	2.27 ± 0.04

Table 5.3: ***Average values of the three relevant parameters estimated by the stochastic model.***
For each parameter, the force of a motor f_0, the fraction of actin-attached motors r, and the rate of transition through the attachment-detachment cycle ϕ, mean $\pm$ SD are obtained by averaging over 6 *data records, for each isoform.*

Estimated Parameters	fast	slow	ratio
f_0 (pN)	6.8 ± 1.0	2.4 ± 0.4	2.8
r	0.32 ± 0.02	0.50 ± 0.03	0.64
$\phi(\mathrm{s}^{-1})$	6.0 ± 0.2	2.27 ± 0.04	2.6

Let us now relax the constraint $N = 16$ obtained from the rigor experiments and scan the range of N that yields convergence of the optimisation algorithm, for the imposed level of accuracy. The results of the analysis for the soleus isoform for different system size N is reported in Figure 5.3, where the best fit values of f_0 (symbols) are plotted against different choices of N. The histogram computed from the collection of fitted parameters can be conceptualised as an indirect imprint of the degree of experimental variability as associated to f_0 and N. The shaded region identifies the portion of the parameters plane where the solutions are expected to be found. Specifically, it is assumed to lay in between the two curves:

$$f_0 N = \frac{20}{11} \langle F_0 \pm 2\Delta F_0 \rangle \left\langle \frac{a}{b} \right\rangle$$

Here the relative error associated with the average value of the quantity $\langle a/b \rangle$ is assumed negligible, as compared to that stemming from the average stationary force, ΔF_0. The histogram computed from the collection of fitted parameters (each choice of symbols refers to a different experimental series) can be conceptualised as an indirect imprint of the degree of experimental variability as associated to f_0 and N.

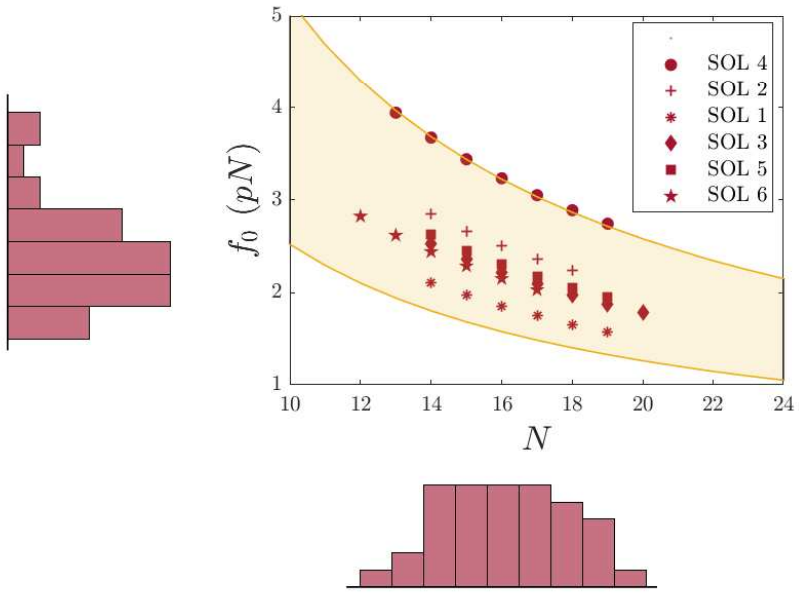

Figure 5.3: ***f_0 vs. N on the force of the soleus HMMs ensemble.*** *The estimated parameter f_0 of the soleus HMMs is plotted as a function of the imposed N; each choice of symbols refers to a different experimental series. The shaded region is drawn from the theoretical curve that resolve the dependence of f_0 on N.*

5.2 Discussion

In the previous Section we used the DLOT apparatus to define the performance, under isometric conditions, of an array of 16 myosin motors purified from either fast (psoas), or slow (soleus), muscle of the rabbit. To eliminate the large trap compliance and recover the condition for the motors to operate as independent force generators, as in the native half-sarcomere, once the interaction is established the system control is switched from position clamp to length clamp. The array of 16 motors in physiological ATP concentration (2 mM) at 24 °C exhibits a steady isometric force that is 17 pN for the fast isoform, and is 10.5 pN for the slow isoform. The finding that the force exerted by the same number of motors is 1.6-fold larger in the fast isoform disagrees with the most common finding in muscles and muscle fibres that the isometric force normalised for the cross sectional area of the fibre T_0, is either similar or at max 1.5-fold larger in the fast isoform [41–44, 46–50]. Notably in skinned fibres from the same rabbit muscles from which the nanomachine motor proteins are purified, T_0 in psoas at 25 °C has been found 317 ± 14 kPa, 1.9-fold larger than T_0 in soleus, 165 ± 12 kPa [74].
Recording the development of the steady isometric force in length clamp eliminates the contamination of the large trap compliance, showing a roughly exponential time course characterised by the parameter t_r that is 238 ms for the slow isoform and 77 ms for the fast isoform. Thus the rise of the force to the maximum steady value takes a 3-fold longer time for the slow isoform than for the fast isoform. How this emergent property of the motor ensemble relates to the corresponding event *in situ*, and how it is affected by the different isoforms, has been tested by comparing the nanomachine output with that of Ca^{2+}-activated skinned fibres, from the same rabbit muscles from which the motor proteins were purified. According to the sarcomere-level mechanics for skinned fibres developed in our laboratory, the compliance of the attachments of the skinned fibre segment to the transducer levers is negligible. A detailed description of the protocol adopted to obtain the rate of force development *in situ* is provided in Appendix C. Turning back to consider the synthetic nanomachine under these conditions, the force redevelopment following a fast shortening able to drop the isometric force to zero is characterised by a rise time $t_r = 265 \pm 15$ ms in soleus fibres and $t_r = 62 \pm 5$ ms in psoas fibres. Thus, the time course of force development, recorded by the nanomachine in length clamp and its modulation by the two isoforms, are in quite satisfactory agreement with those recorded at the cell level. The corresponding rates of force development a are $28.6\,s^{-1}$ for the fast isoform and $9.3\,s^{-1}$ for the slow isoform recorded by the nanomachine. Considering that in length clamp such rate is direct expression of the sum of the effective rate constant of attachment/force-generation and the effective rate constant of detachment of the myosin motors, we conclude that the interaction kinetics in isometric condition is 3-fold higher in the fast isoform than in the slow isoform. The attachment/detachment kinetics is expected to increase if the load on the motor ensemble is reduced, due to the strain-dependent increase in rate constant of detachment, which underpins the maximum velocity of shortening V_0 attained under zero load. V_0 estimated by the time taken by the ensemble to redevelop force following a release able to drop the isometric force to zero (Figure 2.4a, d) is $0.5\,\mu m\,s^{-1}$ and $1.95\,\mu m\,s^{-1}$ in the slow and fast HMM respectively, showing a $V_0 \sim 4$-fold larger in the fast isoform. Thus, the isoform-dependent increase of V_0 is 33% larger than the increase in a and even larger if one considers that V_0 of the fast isoform is underestimated by the proportionally larger fraction of time spent for

Table 5.4: ***Energetic cost of isometric contraction.***
The energetic cost of isometric contraction is reported in terms of the ATP hydrolysis rate per myosin motor ϕ, in slow and fast mammalian skeletal muscle, and its ratio R for fast over slow muscle. Data from the literature (ref, in brackets) except the last row that reports the data from the nanomachine

ϕ (s^{-1})	[ref.]	fast	slow	R
Mouse muscle 21 °C	[41]	12.4	2.47	5.0
Mouse muscle 25 °C	[42]	13.3	2.95	4.5
Rat muscle 27 °C	[44]	12.5	2.3	5.4
Rat skinned fibre 12 °C	[46]	1.28	0.25	5.12
Rabbit skinned fibre 12 °C	[49]	1.79	0.23	7.78
Human skinned fibre 12 °C	[50]	3.22	0.65	4.95
Nanomachine 24 °C		6.0	2.3	2.6

the force to drop to zero following the release (compare the records in Figure 2.4a, d). This suggests that the fast isoform exhibits a specifically larger strain dependence of the detachment rate constant.

The rate of development of the isometric steady force and the force fluctuations superimposed on the steady force in length clamp have been exploited to implement a three-state stochastic model which is able to fit the experimental responses, allowing self-consistent estimates of all the relevant mechanokinetic parameters underlying the isometric performance of the motor ensemble: the force of a single correctly oriented motor f_0, the fraction of attached motors r, and the rate of transition through the attachment/detachment cycle ϕ (see Table 5.3). The force of a single correctly oriented motor f_0 of the fast isoform (6.8 ± 1.0 pN) is 2.8-fold larger than f_0 of the slow isoform (2.4 ± 0.4 pN), while the ensemble force F_0 is only 1.6 times larger (Figure 2.4b, e). This is in a great part explained by the different fraction of attached motors r, which in the fast isoform (0.32 ± 0.02) is 0.64 that of the slow isoform (0.50 ± 0.03). The corresponding number of attached motors (Nr) is ~ 5 and ~ 8 for the fast and the slow isoform respectively. The average force of a single randomly oriented motor ($0.55 f_0$) is 3.7 pN for the fast isoform and 1.3 pN for the slow isoform, from which the predicted ensemble force is ($3.7 \times 5 =$) 18.5 pN and ($1.3 \times 8 =$) 10.4 pN respectively. These values are in quite good agreement with the observed values: 17 ± 3 pN for the fast isoform and 10.5 ± 1.8 pN for the slow isoform.

The model predicts a rate of transition of a motor through the interaction cycle, and thus a frequency of ATP splitting per motor ϕ, which is 2.6 times higher for the fast isoform ($6.0\,s^{-1}$) than for the slow isoform ($2.3\,s^{-1}$), see Table 5.3. The value of ϕ of the slow isoform array is in a remarkably good agreement with that estimated on the slow muscle of mouse and rat (2.3-2.9 s^{-1}), as shown in Table 5.4.

On the other hand, ϕ for the fast isoform array is less than half of the one estimated in the fast muscle of the same animals (12.4-13.3 s^{-1}), Table 5.4. The same discrepancy for the isoform-dependent increase in ϕ is found between the model prediction and the skinned fibre experiments [46–50]. However, it must be noted that: (*i*) the absolute values of ϕ in skinned fibres is 10-fold smaller than the one in the muscle for both slow and fast myosin isoforms [46–49]; (*ii*) the difference can only in minor part be explained by the different

temperature of the experiments (21-27 °C for the muscle and 12 °C for the skinned fibres), taking into account that the temperature factor Q_{10} of ϕ is ≤ 2.5 in either preparation [42, 50, 75]. The rate of ATP splitting ϕ predicted by the model for the output of the fast isoform nanomachine is 2.5-fold larger than that predicted for the slow isoform, but still 2-fold smaller than that indicated by the energy rate measured in the fast muscle. Thus the 5-fold larger ϕ of the fast isoform with respect to the slow isoform found in muscle is only partly explained by higher rate constants of transitions through the conventional attachment/force generation and detachment cycle operating in isometric conditions and recorded by the nanomachine force fluctuations. The actin-activated myosin ATPase activity in solution is 2.5 times larger in fast than in slow muscle [51], which can be accounted for by a higher rate of ADP release (which is followed by a fast ATP binding and detachment [76], step (c)-(d) in Figure 1.4) and/or a higher rate of the hydrolysis step (d)-(e), and/or a higher rate of actin attachment (step (a)-(b)). In isometric contraction at physiological ATP concentration, ADP release is the rate-limiting step for detachment and is 10-fold slower in slow myosin than in fast myosin [76] and this may *per se* explain the finding that during steady isometric force generation the duty ratio of the fast myosin nanomachine is lower than that of the slow myosin nanomachine. However, it must be taken into account that under isometric conditions (or high load) the transitions through the different force-generating states of the motor (step (a)-(b)/(c) in Figure 1.4) slow down due to the strain dependence of the transition rate [24, 77] and thus the subsequent conformation-dependent release of ADP also gets slower [28]. As far as the difference in ϕ between slow and fast myosin ensembles in isometric contraction, the finding that the force of fast myosin is 2.5-fold higher should suggests that the equilibrium distribution between different force-generating states is shifted toward the end of the working stroke in the fast myosin, in this way explaining a larger flux through the detachment step and thus the reduction in the duty ratio and the increase in ϕ with respect to the slow myosin (Table 5.3). However, it must be considered that the stiffness of the myosin motor, determined *in situ* with fast sarcomere-level mechanics applied to skinned fibres from rabbit muscle, is larger in the fast muscle in proportion to the motor force, so that the extent of the force-generating structural change is the same in either fast or slow myosin motor [78].

In conclusion, the 2.5-fold larger isometric ϕ of the fast myosin isoform found with the analysis of force fluctuations is accounted for by an intrinsic faster rate of the relevant kinetic steps of the fast myosin isoform which underpins a 2.5-fold larger ATPase rate in solution [51]. Instead, the 5-fold larger isometric ϕ of the fast isoform reported in the literature (see Table 5.4), exceeds by a factor of 2 the one recorded by the nanomachine force fluctuations at 25 °C and could be explained by a further kinetic adaptation of fast myosin isoform hypothesising that, also in isometric conditions, a futile faster actin-activated ATPase cycle is present. In terms of the kinetic scheme in [79], this cycle implies the working stroke transition to occur in the motor undergoing weak actin-binding interactions and does not imply strong/force-generating attachment unless the load is reduced and the muscle shortens.

A comparison of the parameters estimated in this work with those obtained in previous nanomechanical approaches is possible for the fast isoform purified from rabbit psoas investigated by Yanagida's group [55] through the microneedle manipulation technique. In close-to-isometric conditions, obtained through a stiff microneedle, both the force of the motor (5.9 pN) and the fraction of actin-attached motors (0.36) estimated in that

work are in exceptional good agreement with the values calculated here from the output of the nanomachine. A peculiar difference that makes our nanomachine unique is the possibility to define the performances emerging from the array arrangement of the motors in the half-sarcomere, as the force-velocity relation and the maximum power output.
The novelty of the present nanomachine application in relation to the previous ones [61–63], is the interpretation of the output of the motor ensemble and of the isoform-dependent differences on the basis of the mechanokinetic molecular properties of either isoform is self-consistent way without any assumptions from cell mechanics and solution kinetics.
The achievements of the combined experimental and theoretical approach illustrated in this Thesis set the basis for future studies on the emergent mechanokinetic properties of the nanomachine assembled with any other myosin motor, either engineered or purified from mutant animal models or human biopsies.

Conclusions

This Thesis concerns a combined experimental and theoretical study on the performance of a synthetic nanomachine made by an ensemble of fast and slow isoforms of the protein myosin II, the molecular motor of striated (skeletal and cardiac) muscle.
The first Chapter is an overview of the physiology of striated muscle contraction, focusing on the sarcomere, the structural unit of the striated muscle cell. I detailed the organization and the role of the proteins in the sarcomere, in particular the contractile proteins, myosin and actin, the regulatory proteins on the thin actin-containing filament, troponin and tropomyosin, as well as myosin binding protein-C and the cytoskeleton protein in the thick filament. I also provided a brief description of the chemo-mechanical acto-myosin ATPase cycle, responsible for the transduction of chemical energy into mechanical work, of the characteristics of myosin II as a nonprocessive molecular motor that works efficiently in ensemble, and of the functional differences between fast and slow isoforms of myosin II. At the end of the Chapter I provided a brief summary of the latest experimental techniques developed in recent years to investigate and characterise muscle myosin *in vitro*, highlighting the originality, as well as the limitations, of conventional laser trap techniques for single molecule mechanics and the privilege of our application of the Dual Laser Optical Tweezers to measure and control the performance of an ensemble of myosin motors interacting with an actin filament, in a half-sarcomere-like nanomachine.
The second Chapter is dedicated to the description of the methodology implied to build the nanomachine, including the methods for purifying and assembling the proteins, the protocol for the definition of the number of motors available for the actin interaction, the recording and analysis of transient and steady state force responses in isometric conditions of the nanomachine powered by either the slow or the fast myosin isoform.
In the third Chapter I introduced the theoretical background of the stochastic model that allowed the parameters estimation for an ensemble of myosin motors performing isometric contractions, then I described the fitting strategy for the parameters estimation, as well as the validation of the fitting scheme on synthetically generated data.
In the fourth Chapter I presented a generalisation of the theoretical model to include the contributions of two populations of force-generating motors, which will allow to analyse data collected at different temperatures, when the force of the ensemble is significantly affected by the change in proportion of motors in different force-generating states. A fitting procedure was validated against synthetic data, and I showed that combining data obtained at different temperatures allowed us to provide a more robust estimation of the kinetic rate constants of the model.
In the last Chapter the fitting procedure presented in Chapter 3 was applied on experimental data recorded from the output of the nanomachine powered by an ensemble slow and fast isoforms performing isometric contractions at room temperature, extracting for either

isoform the intrinsic mechanokinetic parameters underlying the ensemble performance: the force per motor, the fraction of motors attached during steady state force response and the rate of the chemo-mechanical cycle. I then discussed the main results of this work and their significance in relation to the data present in the literature.
In conclusion, in the Thesis it is illustrated that by combining the experimental results obtained with a synthetic nanomachine with the stochastic model approach, it is possible to characterise the main mechanokinetic features of the performance of fast and slow myosin isoform, without any assumptions from in-cell and solution experiments. This will allow the definition of the performance of unknown myosin isoforms, mutant myosins and engineered motors.

Appendix A

Dual Laser Optical Tweezers

In 1987 Ashkin and collaborators published the work in which they described the device they invented, which they named Optical tweezers [58]. They found that micro-sized particles with high indexes of refraction (such as cells, bacteria, viruses or beads) can be trapped in an electric field gradient near the laser focus. The typical configuration of an optical trap setup consists of a highly focused laser beam, trapping a dielectric object (typically a polystyrene bead) towards the focus. Near-infrared wavelengths ($800-1100\,\mathrm{nm}$) are commonly used for the trapping laser as they minimize the absorption of the laser light and consequently the biological photodamage, and can be easily incorporated into imaging systems that use visible light. For a displacement from the equilibrium position of about 150 nm, the optical trap acts as a harmonic potential well, pulling the bead toward the centre of the trap. Under this condition the force is proportional to the displacement and can be measured by quantifying the bead displacement from its equilibrium position (in the trap centre). The common trap stiffness for optical tweezers is $\sim 0.1\,\mathrm{pN\,nm^{-1}}$, while the displacement measurements have a typical accuracy of $\sim 10\,\mathrm{nm}$, this results in $\sim 1\,\mathrm{pN}$ force measurement resolution (under the hypothesis of Hookean spring), which can be increased by decreasing the trap stiffness.

The piconewton force range accessible to optical traps makes them particularly useful for the investigation of biological systems, or interactions that occur in the same range of force, like ligand-receptor binding, protein unfolding and nucleic acids structural dynamics. For this reason, since their implementation, optical tweezers have been utilised to study the kinetics and the mechanical properties of single molecules, like the direct measurements of force and displacement resulting from the interaction of a single skeletal muscle myosin with a suspended actin filament [22].

The trapping force results from the interaction between the light impinging on the particle and the trapped object, and the proper physical description of the phenomenon depends on the size of the trapped particle relative to the wavelength of light used to trap it. When the dimensions of the particles are much greater than the wavelength of trapping laser, the trapping phenomenon can be described in terms of momentum conservation in the context of ray optics. A beam of light interacting with the surface of a particle with a refraction index higher than the surrounding medium is refracted or reflected and changes its propagation direction. A change in the direction corresponds to a change in the momentum carried by light photons, and by momentum conservation law, there is no change in the total momentum as the particle experiences a reaction impulse equal

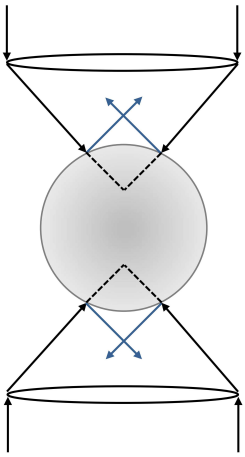

Figure A.1: ***Schematic representation of scattering forces in a dual-beam optical setup.***
In blue, the two light beams reflected when impinging the surface of the particle. Since the scattering forces generated at the two opposite sides of the bead have the same amplitude but are opposite in direction, they cancel out each other out, and the total scattering force acting on the trapped object is null. This setup gives the system a good axial stability.

and opposite to the change in deflected rays momentum, thus pointing towards the laser focus. If the diameter of the particle is much smaller then the wavelength of the trapping laser, a description in terms of electric dipoles in an electric field is needed. In Rayleigh regime the dielectric particles is a Rayleigh scatterer (with a polarizability α) interacting with the electric field E of the light source, that induces a dipole moment in the particle. The particle is subjected to a force proportional to its volume, towards the focus of the trap. The resulting optical force is further decomposed into two components, a gradient force (a trapping force in the direction of the field gradient), and a scattering force proportional to both α and to the optical intensity gradient in the focus. This latter is due to the reflection of the light at the surface of the particle, and tends to push the sphere out of the trap. Therefore, in order to generate a stable trapping, the optical trap must be designed so that the gradient component of the force pulling the particle towards the focus exceeds the scattering component pushing it away from the trap centre; this is usually attained by using high numerical aperture objectives, as water or oil immersion objectives (the latter suffering from spherical aberrations reducing the trapping performance). As a result of the balancing between the gradient force and the scattering force, the axial equilibrium position of a trapped particle is located slightly beyond the focal point.
An alternative optical tweezers design is the Dual Laser Optical Tweezers (DLOT) [80], in which two separate laser beams are focused by two microscope objectives (facing each other) to the same spot. The scattering forces generated by reflection on each side of the bead are equal but have opposite direction, so that in this way the net scattering force acting on the particle is zero and the axial trap stability is greatly enhanced, see Figure A.1. For a given laser power, a higher trapping force can be generated, and lower numerical aperture microscope objectives can be used. A disadvantage with respect to

the single-beam design, in a Dual Laser Optical Tweezers setup the two laser beams need to be carefully aligned (to within less than the bead diameter) and the resulting measurements must be corrected for errors due to the drift in the relative beam alignment. With this setup the trapping laser itself can be used to measure the force acting on the trapped bead. The change in the direction of the light propagation, that corresponds to the change in the momentum of the laser light due to the presence of the particle, may be measured by imaging the bead position with a position sensitive photodiode detector [81]. With this method, force calibration is independent of the particle size, shape and refractive index.

Appendix B

Spatial-dependent model for myosin motors performing isometric contractions

A more general, spatial-dependent model for the attachment-detachment dynamics of the molecular motors ensemble can be formulated following the definition of spatial-dependent configurations for the molecular motors.
We consider a spatial support that corresponds to the relative distance between the motor and the actin monomer available for interaction.
The spatial range for possible myosin-actin interaction is $L = 5\,\text{nm}$, that means that a molecular motor can attach itself to an actin monomer with the binding site that is located at maximum 2.5 nm from it, forward or backward along the actin filament.
We can consider a discrete spatial variable $i = \{1, \ldots, \Omega\}$ where $i = 1$ corresponds to a motor attached in position $d = -2.5\,\text{nm}$ and $i = \Omega$ corresponds to a motor attached in position $d = 2.5\,\text{nm}$.
In addition to that the random orientation of the molecular motors on their support implies that the force that each motor exerts depends on the binding angle $\theta \in [0, \pi]$, with $\theta = 0$ corresponds to the correct orientation.
The possible configurations for each molecular motor are: D for a detached motor, $(A_1)^i)$ for a motor attached in position $d = i$, exerting a force $(f_1)^i$, and $(A_2)^i)$ for a motor attached in position $d = i$, exerting a force $(f_2)^i$. The state of the system at any time t is represented by the 2Ω dimensional vector $\boldsymbol{n}(t)$, which contains the number of molecular motors in the two force-exerting configurations:

$$\boldsymbol{n}(t) = (\boldsymbol{n}_1(t), \boldsymbol{n}_2(t)) \tag{B.1}$$

with $\boldsymbol{n}_1 = \sum_{i=1}^{\Omega} n_1$ and $\boldsymbol{n}_2 = \sum_{i=1}^{\Omega} n_2$ representing the total number of motors attached in configurations A_1 and A_2 respectively, for every value of the position d. The number of detached motors at any time $n_D(t)$ can be obtained from the conservation law:

$$N = n_D + \sum_{i=1}^{\Omega} (n_1^i + n_2^i).$$

Working in this framework implies that in principle the kinetic rate constants associated with the microscopic transitions between microscopic configurations are spatial dependent.

From the analysis of the spatial dependency of the rate constant in [61] we can see as the kinetic rates k_1, k_{-1}, k_{-2}, k_3 are roughly constant as a function of the position d, therefore in the following we will consider that rate constants k_1, k_{-1}, k_{-2}, k_3 so not depend on the position d, while we assume that k_2 is linear in d. A schematic representation of the microscopic dynamics for a single motor is the following:

$$\mathrm{D} \underset{\mathrm{k_{-1}}}{\overset{\mathrm{k_1}/\,\Omega}{\rightleftharpoons}} \mathrm{A_1}^i \underset{\mathrm{k_{-2}}}{\overset{\mathrm{k_2}^i}{\rightleftharpoons}} \mathrm{A_2}^i \xrightarrow{\mathrm{k_3}} \mathrm{D} \tag{B.2}$$

The reaction rate constants k_j represent the probability for unit of time that the reaction j is happening, and they are expressed in unit of s^{-1}.
The master equation associated with the microscopic dynamic described by the chemical equations (B.2) has the same form of the master equation in the non spatial case, i.e. equation (3.2), but the state of the system is now defined by (B.1), and the terms $\mathbb{T}(\boldsymbol{n'}|\boldsymbol{n})$ that represent the transition rates from the state $\boldsymbol{n}$ to a new state $\boldsymbol{n'}$are now defined as:

$$\begin{aligned}
&\textit{ATTACHMENT} && \mathbb{T}(n_1^i + 1|\boldsymbol{n}) = \frac{k_1}{\Omega}\frac{n_D}{N} = \frac{k_1}{\Omega}\Big[1 - \frac{1}{N}\sum_{i=1}^{\Omega}(n_1^i + n_2^i)\Big] \\
&\textit{DETACHMENT} && \mathbb{T}(n_1^i - 1|\boldsymbol{n}) = k_{-1}\frac{n_1^i}{N} \\
&\textit{CONVERSION} && \mathbb{T}(n_1^i - 1, n_2^i + 1|\boldsymbol{n}) = k_2^i\frac{n_1^i}{N} \\
&\textit{CONVERSION} && \mathbb{T}(n_1^i + 1, n_2^i - 1|\boldsymbol{n}) = k_{-2}\frac{n_2^i}{N} \\
&\textit{DETACHMENT} && \mathbb{T}(n_2^i - 1|\boldsymbol{n}) = k_3\frac{n_2^i}{N}
\end{aligned} \tag{B.3}$$

With the explicit expressions for the transition rates for all the possible reactions, the master equation (3.2) reads:

$$\begin{aligned}
\frac{\partial P(\boldsymbol{n},t)}{\partial t} = \sum_{i=1}^{\Omega}\Big[&\mathbb{T}(\boldsymbol{n}|n_1^i - 1)P(n_1^i - 1, t) - \mathbb{T}(n_1^i + 1|\boldsymbol{n})P(\boldsymbol{n},t) + \\
&+ \mathbb{T}(\boldsymbol{n}|n_1^i + 1)P(n_1^i + 1, t) - \mathbb{T}(n_1^i - 1|\boldsymbol{n})P(\boldsymbol{n},t) + \\
&+ \mathbb{T}(\boldsymbol{n}|n_1^i + 1, n_2^i - 1)P(n_1^i + 1, n_2^i - 1, t) + \\
&- \mathbb{T}(n_1^i - 1, n_2^i + 1|\boldsymbol{n})P(\boldsymbol{n},t) + \\
&+ \mathbb{T}(\boldsymbol{n}|n_1^i - 1, n_2^i + 1)P(n_1^i - 1, n_2^i + 1, t) + \\
&- \mathbb{T}(n_1^i + 1, n_2^i - 1|\boldsymbol{n})P(\boldsymbol{n},t) + \\
&+ \mathbb{T}(\boldsymbol{n}|n_2^i + 1)P(n_2^i + 1, t) - \mathbb{T}(n_2^i - 1|\boldsymbol{n})P(\boldsymbol{n},t)\Big]
\end{aligned}$$

The temporal behaviour of the discrete concentration of the three populations of motors in each configuration can be obtained performing the Gillespie algorithm.
The concentration of motors in the configurations n_D, n_1^i, n_2^i, in the case $\Omega = 10$, is shown in Figure (B.1). Employing these temporal series for the dynamics of the concentrations of each population, it is possible to obtain the histogram of the probability

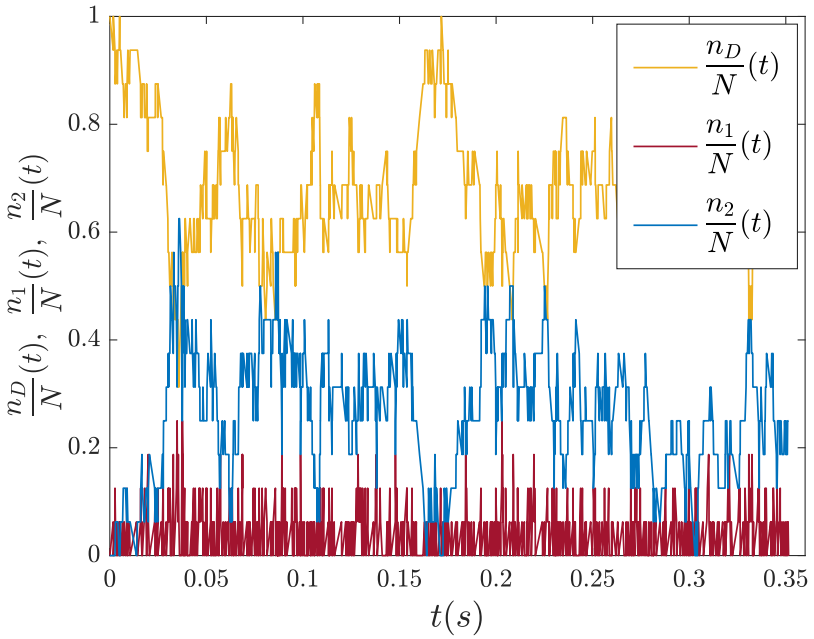

Figure B.1: Temporal behaviour of the fractions of the three motors populations in each configuration: n_D, n_1^i, n_2^i, in the case $i = 1$, as obtained via the Gillespie algorithm.

distribution associated with the subpopulations of motors in the configurations D, A_1^i and A_2^i, in two different cases: $\Omega = 3$ and $\Omega = 10$, as shown in Figure (B.2). We then consider these probability distributions for the cumulative population of motors in the force-generating configurations $n_1 = \sum_{i=1}^{\Omega} n_1^i$ and $n_2 = \sum_{i=1}^{\Omega} n_2^i$, and we can observe that the global populations of each state do not depend on the spatial details of the attached motors configurations. By confronting the two types of histograms in Figure (B.3) we can conclude that this spatial characterisation of the configurations A_1 and A_2 can be neglected, and simplify the characterisation of the system in order to obtain a set of reaction constants not depending on the spatial coordination d. As a result we can formulate the stochastic model without the spatial details.

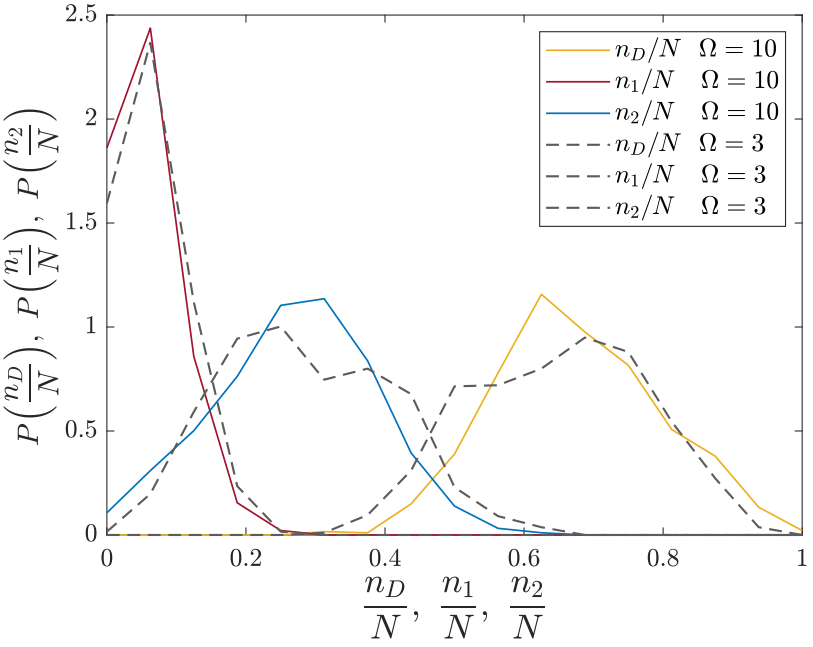

Figure B.2: Comparison between the normalised histograms of the fractions of the three motors populations in each state: $\frac{n_D}{N}$, $\frac{n_1^i}{N}$, $\frac{n_2^i}{N}$, as obtained from the simulated dynamics for a suitable choice of the kinetic parameters and for $\Omega = 3$ (grey dashed lines) and $\Omega = 10$ (solid coloured lines).

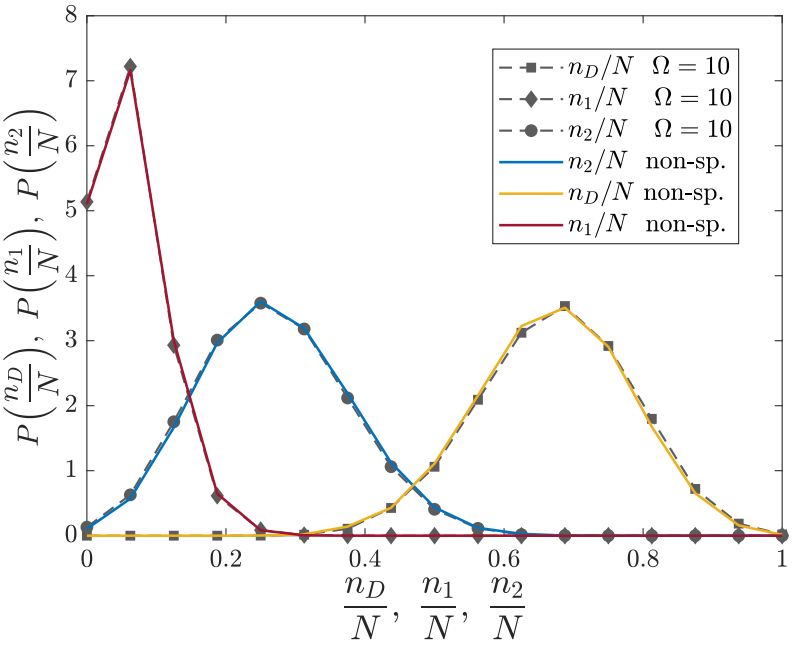

Figure B.3: Comparison between the normalised histograms of the fractions of motors in the case of the spatial model (concentrations of the molecular motors in the state D, A_1 and A_2 as a sum of the subpopulations in states A_1^i, A_2^i, for $i = 1, \ldots, \Omega$), and the non-spatial model.

Appendix C

The rate of force development measured *in situ*

In the following we described of the protocol adopted to obtain the rate of force development *in situ*. The time course of isometric force redevelopment following a release that drops the isometric force to 0 was determined in Ca^{2+}-activated demembranated fibres from the same slow and fast muscles of the rabbit used to extract the myosin isoforms for the nanomachine. As previously described [72, 74, 78], small bundles dissected from the two muscles were stored in skinning solution containing 50% glycerol at −20 °C for 3–4 weeks and single fibres were prepared just before the experiment. A fibre segment 4-6 mm long was clamped at its extremities by T-clips and mounted between the lever arms of a loudspeaker motor and a capacitance force transducer [82]. To prevent sliding of the ends of the fibre segment inside the clips and minimise the shortening of the activated fibre against the damaged sarcomeres at the ends of the segment during force development, the extremities of the fibre were fixed first with a rigor solution containing glutaraldehyde and then glued to the clips with shellac dissolved in ethanol. Fibres were activated by temperature jump using a solution exchange system as previously described [72]. A striation follower [83] allowed nanometre-microsecond resolution recording of length changes in a selected population of sarcomeres.

The composition of the solutions has been reported previously ([74], Supplementary Table 1, 25 °C). The increase of interfilamentary distance following cell membrane permeabilisation was reversed by the addition of the osmotic agent Dextran T-500 (4% weight/volume). The rate of force development was determined on the isometric force redevelopment recorded after superimposing on the isometric contraction of the maximally Ca^{2+}-activated fibre (pCa 4.5) a fast ramp shortening (5-6% of the initial fibre length) able to drop the force to zero (see Figure C.1).

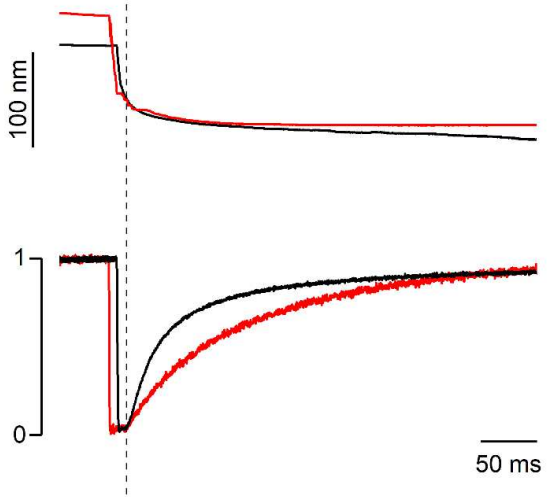

Figure C.1: ***Time course of force redevelopment in fast and slow skinned fibres.*** *Force redevelopment (lower traces) and corresponding half-sarcomere shortening (upper traces) after a period of unloaded shortening in a skinned fibre from rabbit psoas (black traces) and soleus (red traces) muscles. The vertical line indicates the time at which the force development starts. Force is normalised for the isometric value (T_0) before the imposed large shortening ($\sim 5\%$ of the fibre length or $\sim 60\,\mathrm{nm}$ per hs). Further shortening against end compliance during force redevelopment was $29 \pm 6\,\mathrm{nm}$ per hs ($n = 4$) and $19 \pm 3\,\mathrm{nm}$ per hs ($n = 11$) in fast and slow fibres respectively. T_0 was $276 \pm 44\,\mathrm{kPa}$ and $195 \pm 26\,\mathrm{kPa}$ in fibres from psoas and soleus respectively. Temperature, $25.2\,^{\circ}\mathrm{C}$. 4% dextran T-500 was added to reduce the lateral filament spacing of the relaxed fibre to the value before skinning.*

Bibliography

1. Huxley, A. F. & Niedergerke, R. Structural changes in muscle during contraction: interference microscopy of living muscle fibres. *Nature* **173,** 971–973 (1954).
2. Huxley, H. & Hanson, J. Changes in the cross-striations of muscle during contraction and stretch and their structural interpretation. *Nature* **173,** 973–976 (1954).
3. Gordon, A., Huxley, A. F. & Julian, F. The variation in isometric tension with sarcomere length in vertebrate muscle fibres. *The Journal of physiology* **184,** 170–192 (1966).
4. Seiler, S. H., Fischman, D. A. & Leinwand, L. A. Modulation of myosin filament organization by C-protein family members. *Molecular biology of the cell* **7,** 113–127 (1996).
5. Dominguez, R., Freyzon, Y., Trybus, K. M. & Cohen, C. Crystal structure of a vertebrate smooth muscle myosin motor domain and its complex with the essential light chain: Visualization of the pre–power stroke state. *Cell* **94,** 559–571 (1998).
6. Smith, C. A. & Rayment, I. X-ray structure of the magnesium (II) ADP vanadate complex of the Dictyostelium discoideum myosin motor domain to 1.9 Å resolution. *Biochemistry* **35,** 5404–5417 (1996).
7. Geeves, M. A. & Holmes, K. C. Structural mechanism of muscle contraction. *Annual review of biochemistry* **68,** 687–728 (1999).
8. Dominguez, R. & Holmes, K. C. Actin structure and function. *Annual review of biophysics* **40,** 169–186 (2011).
9. Taylor, K. A. *et al.* Tomographic 3D reconstruction of quick-frozen, Ca2+-activated contracting insect flight muscle. *Cell* **99,** 421–431 (1999).
10. Wu, S. *et al.* Electron tomography of cryofixed, isometrically contracting insect flight muscle reveals novel actin-myosin interactions. *Biophysical Journal* **98,** 216a (2010).
11. Steffen, W., Smith, D., Simmons, R. & Sleep, J. Mapping the actin filament with myosin. *Proceedings of the National Academy of Sciences* **98,** 14949–14954 (2001).
12. Greaser, M. L. & Gergely, J. Purification and properties of the components from troponin. *Journal of Biological Chemistry* **248,** 2125–2133 (1973).
13. Herzberg, O. & James, M. N. Structure of the calcium regulatory muscle protein troponin-C at 2.8 Å resolution. *Nature* **313,** 653–659 (1985).
14. Potter, J. D. & Gergely, J. Troponin, tripomyosin, and actin interactions in the Ca2+ ion regulation of muscle contraction. *Biochemistry* **13,** 2697–2703 (1974).

15. Herzberg, O., Moult, J. & James, M. N. in *Methods in Enzymology* 610–632 (Elsevier, 1987).

16. Ingraham, R. H. & Swenson, C. A. Binary interactions of troponin subunits. *Journal of Biological Chemistry* **259,** 9544–9548 (1984).

17. Van Eyk, J. E. *et al.* Distinct regions of troponin I regulate Ca2+-dependent activation and Ca2+ sensitivity of the acto-S1-TM ATPase activity of the thin filament. *Journal of Biological Chemistry* **272,** 10529–10537 (1997).

18. Huxley, A. F. Muscle structure and theories of contraction. *Prog. Biophys. Biophys. Chem* **7,** 255–318 (1957).

19. Huxley, H. E. The Mechanism of Muscular Contraction: Recent structural studies suggest a revealing model for cross-bridge action at variable filament spacing. *Science* **164,** 1356–1366 (1969).

20. Lymn, R. & Taylor, E. W. Mechanism of adenosine triphosphate hydrolysis by actomyosin. *Biochemistry* **10,** 4617–4624 (1971).

21. Geeves, M. A. & Holmes, K. C. The molecular mechanism of muscle contraction. *Advances in protein chemistry* **71,** 161–193 (2005).

22. Finer, J. T., Simmons, R. M. & Spudich, J. A. Single myosin molecule mechanics: piconewton forces and nanometre steps. *Nature* **368,** 113–119 (1994).

23. Rayment, I. *et al.* Three-dimensional structure of myosin subfragment-1: a molecular motor. *Science* **261,** 50–58 (1993).

24. Huxley, A. F. & Simmons, R. M. Proposed mechanism of force generation in striated muscle. *Nature* **233,** 533–538 (1971).

25. Geeves, M. A. The dynamics of actin and myosin association and the crossbridge model of muscle contraction. *Biochemical journal* **274,** 1 (1991).

26. White, H. & Taylor, E. Energetics and mechanism of actomyosin adenosine triphosphatase. *Biochemistry* **15,** 5818–5826 (1976).

27. Caremani, M., Melli, L., Dolfi, M., Lombardi, V. & Linari, M. The working stroke of the myosin II motor in muscle is not tightly coupled to release of orthophosphate from its active site. *The Journal of physiology* **591,** 5187–5205 (2013).

28. Caremani, M., Melli, L., Dolfi, M., Lombardi, V. & Linari, M. Force and number of myosin motors during muscle shortening and the coupling with the release of the ATP hydrolysis products. *The Journal of Physiology* **593,** 3313–3332 (2015).

29. Harris, D. E. & Warshaw, D. Smooth and skeletal muscle myosin both exhibit low duty cycles at zero load in vitro. *Journal of Biological Chemistry* **268,** 14764–14768 (1993).

30. Uyeda, T. Q., Kron, S. J. & Spudich, J. A. Myosin step size: estimation from slow sliding movement of actin over low densities of heavy meromyosin. *Journal of molecular biology* **214,** 699–710 (1990).

31. Månsson, A., Rassier, D., Tsiavaliaris, G., *et al.* Poorly understood aspects of striated muscle contraction. *BioMed research international* **2015** (2015).

32. Hill, A. V. The heat of shortening and the dynamic constants of muscle. *Proceedings of the Royal Society of London. Series B-Biological Sciences* **126,** 136–195 (1938).

33. Fenn, W. O. The relation between the work performed and the energy liberated in muscular contraction. *The Journal of physiology* **58,** 373 (1924).

34. Woledge, R. C., Curtin, N. A. & Homsher, E. Energetic aspects of muscle contraction. *Monographs of the physiological society* **41,** 1–357 (1985).

35. Smith, D. & Geeves, M. Strain-dependent cross-bridge cycle for muscle. *Biophysical Journal* **69,** 524–537 (1995).

36. Smith, D. & Geeves, M. Strain-dependent cross-bridge cycle for muscle. II. Steady-state behavior. *Biophysical journal* **69,** 538–552 (1995).

37. Smith, D., Geeves, M. A., Sleep, J & Mijailovich, S. M. Towards a unified theory of muscle contraction. I: foundations. *Annals of biomedical engineering* **36,** 1624–1640 (2008).

38. Linari, M. *et al.* Straightening out the elasticity of myosin cross-bridges. *Biophysical Journal* **118,** 994–1002 (2020).

39. Schiaffino, S. & Reggiani, C. Myosin isoforms in mammalian skeletal muscle. *Journal of applied physiology* **77,** 493–501 (1994).

40. Schiaffino, S. & Reggiani, C. Fiber types in mammalian skeletal muscles. *Physiological reviews* **91,** 1447–1531 (2011).

41. Barclay, C., Constable, J. & Gibbs, C. Energetics of fast-and slow-twitch muscles of the mouse. *The Journal of physiology* **472,** 61–80 (1993).

42. Barclay, C., Woledge, R. & Curtin, N. Is the efficiency of mammalian (mouse) skeletal muscle temperature dependent? *The Journal of physiology* **588,** 3819–3831 (2010).

43. Wendt, I. & Gibbs, C. Energy production of rat extensor digitorum longus muscle. *American Journal of Physiology-Legacy Content* **224,** 1081–1086 (1973).

44. Wendt, I. & Gibbs, C. Energy production of mammalian fast-and slow-twitch muscles during development. *American Journal of Physiology-Legacy Content* **226,** 642–647 (1974).

45. Barclay, C. J., Woledge, R. C. & Curtin, N. A. Inferring crossbridge properties from skeletal muscle energetics. *Progress in Biophysics and Molecular Biology* **102,** 53–71 (2010).

46. Bottinelli, R, Betto, R, Schiaffino, S & Reggiani, C. Unloaded shortening velocity and myosin heavy chain and alkali light chain isoform composition in rat skeletal muscle fibres. *The Journal of physiology* **478,** 341–349 (1994).

47. Reggiani, C *et al.* Chemo-mechanical energy transduction in relation to myosin isoform composition in skeletal muscle fibres of the rat. *The Journal of physiology* **502,** 449 (1997).

48. Potma, E., Van Graas, I. & Stienen, G. Effects of pH on myofibrillar ATPase activity in fast and slow skeletal muscle fibers of the rabbit. *Biophysical journal* **67,** 2404–2410 (1994).

49. Reggiani, C., Bottinelli, R. & Stienen, G. J. Sarcomeric myosin isoforms: fine tuning of a molecular motor. *Physiology* **15,** 26–33 (2000).

50. He, Z.-H., Bottinelli, R., Pellegrino, M. A., Ferenczi, M. A. & Reggiani, C. ATP consumption and efficiency of human single muscle fibers with different myosin isoform composition. *Biophysical journal* **79,** 945–961 (2000).

51. Barany, M, Barany, K, Reckard, T. t. & Volpe, A. Myosin of fast and slow muscles of the rabbit. *Archives of Biochemistry and Biophysics* **109,** 185–191 (1965).

52. Goldman, Y. E. Kinetics of the actomyosin ATPase in muscle fibers. *Annual review of physiology* **49,** 637–654 (1987).

53. Yanagida, T., Nakase, M., Nishiyama, K. & Oosawa, F. Direct observation of motion of single F-actin filaments in the presence of myosin. *Nature* **307,** 58–60 (1984).

54. Sheetz, M. P. & Spudich, J. A. Movement of myosin-coated fluorescent beads on actin cables in vitro. *Nature* **303,** 31–35 (1983).

55. Ishijima, A. *et al.* Multiple-and single-molecule analysis of the actomyosin motor by nanometer-piconewton manipulation with a microneedle: unitary steps and forces. *Biophysical journal* **70,** 383–400 (1996).

56. Ishijima, A. *et al.* Simultaneous observation of individual ATPase and mechanical events by a single myosin molecule during interaction with actin. *Cell* **92,** 161–171 (1998).

57. Svoboda, K., Schmidt, C. F., Schnapp, B. J. & Block, S. M. Direct observation of kinesin stepping by optical trapping interferometry. *Nature* **365,** 721–727 (1993).

58. Ashkin, A. & Dziedzic, J. M. Optical trapping and manipulation of viruses and bacteria. *Science* **235,** 1517–1520 (1987).

59. Tyska, M. *et al.* Two heads of myosin are better than one for generating force and motion. *Proceedings of the National Academy of Sciences* **96,** 4402–4407 (1999).

60. Tyska, M. J. & Warshaw, D. M. The myosin power stroke. *Cell motility and the cytoskeleton* **51,** 1–15 (2002).

61. Pertici, I. *et al.* A myosin II nanomachine mimicking the striated muscle. *Nature communications* **9,** 1–10 (2018).

62. Pertici, I., Bianchi, G., Bongini, L., Lombardi, V. & Bianco, P. A myosin II-based nanomachine devised for the study of Ca2+-dependent mechanisms of muscle regulation. *International journal of molecular sciences* **21,** 7372 (2020).

63. Pertici, I. *et al.* Muscle myosin performance measured with a synthetic nanomachine reveals a class-specific Ca2+-sensitivity of the frog myosin II isoform. *The Journal of Physiology* **599,** 1815–1831 (2021).

64. Pardee, J. D. & Spudich, J. A. Mechanism of K+-induced actin assembly. *The Journal of cell biology* **93,** 648–654 (1982).

65. Kron, S. J., Toyoshima, Y. Y., Uyeda, T. Q. & Spudich, J. A. in *Methods in enzymology* 399–416 (Elsevier, 1991).

66. Suzuki, N., Miyata, H., Ishiwata, S. & Kinosita Jr, K. Preparation of bead-tailed actin filaments: estimation of the torque produced by the sliding force in an in vitro motility assay. *Biophysical journal* **70,** 401–408 (1996).

67. Gillespie, D. T. A general method for numerically simulating the stochastic time evolution of coupled chemical reactions. *Journal of computational physics* **22,** 403–434 (1976).

68. Gillespie, D. T. Exact stochastic simulation of coupled chemical reactions. *The journal of physical chemistry* **81,** 2340–2361 (1977).

69. Sadooghi-Alvandi, S., Nematollahi, A., Habibi, R, *et al.* On the distribution of the sum of independent uniform random variables. *Statistical papers* **50,** 171–175 (2009).

70. Hall, P. The distribution of means for samples of size n drawn from a population in which the variate takes values between 0 and 1, all such values being equally probable. *Biometrika,* 240–245 (1927).

71. Decostre, V, Bianco, P., Lombardi, V. & Piazzesi, G. Effect of temperature on the working stroke of muscle myosin. *Proceedings of the National Academy of Sciences* **102,** 13927–13932 (2005).

72. Linari, M., Caremani, M., Piperio, C., Brandt, P. & Lombardi, V. Stiffness and fraction of myosin motors responsible for active force in permeabilized muscle fibers from rabbit psoas. *Biophysical journal* **92,** 2476–2490 (2007).

73. Van Kampen, N. G. The expansion of the master equation. *Advances in chemical physics* **34,** 245–309 (1976).

74. Caremani, M. *et al.* The force of the myosin motor sets cooperativity in thin filament activation of skeletal muscles. *Communications Biology* **5,** 1266 (2022).

75. Stienen, G., Kiers, J., Bottinelli, R & Reggiani, C. Myofibrillar ATPase activity in skinned human skeletal muscle fibres: fibre type and temperature dependence. *The Journal of physiology* **493,** 299–307 (1996).

76. Iorga, B., Adamek, N. & Geeves, M. A. The slow skeletal muscle isoform of myosin shows kinetic features common to smooth and non-muscle myosins. *Journal of Biological Chemistry* **282,** 3559–3570 (2007).

77. Piazzesi, G. & Lombardi, V. A cross-bridge model that is able to explain mechanical and energetic properties of shortening muscle. *Biophysical journal* **68,** 1966–1979 (1995).

78. Percario, V. *et al.* Mechanical parameters of the molecular motor myosin II determined in permeabilised fibres from slow and fast skeletal muscles of the rabbit. *The Journal of Physiology* **596,** 1243–1257 (2018).

79. Zeng, W. *et al.* Dynamics of actomyosin interactions in relation to the cross-bridge cycle. *Philosophical Transactions of the Royal Society B: Biological Sciences* **359,** 1843 (2004).

80. Ashkin, A. Acceleration and trapping of particles by radiation pressure. *Physical review letters* **24,** 156 (1970).

81. Smith, S. B., Cui, Y. & Bustamante, C. in *Methods in enzymology* 134–162 (Elsevier, 2003).

82. Lombardi, V. & Piazzesi, G. The contractile response during steady lengthening of stimulated frog muscle fibres. *The Journal of physiology* **431,** 141–171 (1990).

83. Huxley, H. *et al.* Millisecond time-resolved changes in x-ray reflections from contracting muscle during rapid mechanical transients, recorded using synchrotron radiation. *Proceedings of the National Academy of Sciences* **78,** 2297–2301 (1981).